Applications of Integrated Polymer Waveguides in Microsystems

Wang, Zhenyu; Wolff, Anders; Kutter, Jörg Peter

Publication date:
2006

Document Version
Publisher's PDF, also known as Version of record

Citation (APA):
Wang, Z., Wolff, A., & Kutter, J. P. (2006). Applications of Integrated Polymer Waveguides in Microsystems.

Applications of Integrated Polymer Waveguides in Microsystems

Ph.D. Thesis, January 2006

Zhenyu Wang

Supervisors: Dr. Anders Wolff
Dr. Jörg P. Kutter
Dr. Dang D. Bang

MIC – Department of Micro and Nanotechnology
Technical University of Denmark

Preface

This thesis has been completed as one of the requirements for pursuing the Ph.D. degree from the Technical University of Denmark (DTU). The Ph.D. work has been carried out in the Cell/ Particle Handling Group at the Department of Micro and Nanotechnology (MIC), Technical University of Denmark from 1st April 2003 to 31st January 2006.

This Ph.D project has been supervised by the following people:
Project leader, Assoc. Prof. Dr. Anders Wolff, main supervisor
Prof. Dr. Jörg P. Kutter, co-supervisor
Senior Scientist, Dr. Dang Duong Bang, co-supervisor

The project has been financed by a grant (Grant no. 26-02-0307) from the Danish Technical Research Council (STVF).

Many people have been involved and contributed to this three year Ph.D. project. I would like to take this opportunity to thank my main supervisor, Dr. Anders Wolff, for his patience and hard work for this project. A special thank to my co-supervisor, Dr. Jörg P. Kutter, for his experience and especially his great help in writing English text. A great thank you also to Dr. Dang D. Bang for his insightful suggestions, efficient organization and encouragement.

During the three years, many people at MIC and DANCHIP have provided their help for this project. I wish to thank Ole Hansen for his creating ideas and suggestions in physical theory of dielectrophoresis, Klaus B. Mogensen, Martin Dufva, Michael Stangegaard, Detlef Snakenborg, Daniel Häfliger, Henning Klank, Anders M. Jorgensen, Maria I. Dimaki, and Maria Nordström and others for their fruitful discussions and ideas. Many thanks to Jamil El-Ali, Ivan R. Perch-Nielsen, Claus R. Poulsen, and Salim Bouaidat, the former Ph.D students of the Cell/ Particle Handling Group at MIC, since a lot of research described in this thesis is based on their previous Ph.D. works.

Finally, I would like to thank my family and my wife for their perpetual support.

Kgs Lyngby, January 31st, 2006

Zhenyu Wang
MIC- Department of Micro and Nanotechnology
Technical University of Denmark, Bldg 345 East
DK-2800, Kgs. Lyngby, Denmark
31st January 2006

Abstract

The research in this thesis focused on different applications of integrated polymer waveguides for real-time optical detection in µTAS (micro total analysis systems). Based on previous research efforts of our group on SU-8 waveguides, dielectrophoresis (DEP) and microchip PCR, the SU-8 waveguides were integrated into a microchip flow cytometer, a microchip DEP-flow cytometer, and a real-time microchip PCR. Those microdevices were applied for detection of cells, investigation of cell sorting processes, and monitoring of PCR products, respectively. Finally, the surface modification of SU-8 was also investigated in this thesis.

With integrated polymer waveguides, a novel microchip flow cytometer was developed for the detection of cell/particle in microfluidic channels. Several different optical elements (waveguides, lens and fiber-to-waveguide couplers) were monolithically defined in same SU-8 (negative epoxy photoresist) layer with microfluidic channels using standard photolithography. Using a band-pass filter set, this microchip flow cytometer could detect three signals (forward scattering, large angle scattering and extinction) of polystyrene beads with different sizes as well as the fluorescence from two different types of labeled blood cells.

Different realizations of cell-sorting microstructures combined with sample pretreatment have been developed, but most of them still use bulk optical system for monitoring purpose. Based on previously developed microchip flow cytometer, two micro flow cytometers were integrated up and downstream of a positive DEP structure for real-time monitoring of the DEP sorting process. The chips were used to quantitatively determine the influence of different factors (flow rate, applied voltage, conductivity of the sample, and frequency of the electric field) on the sorting efficiency for yeast cells. A theoretical model for the capture efficiency was developed and showed a reasonable agreement with the experimental results. Viable and non-viable yeast cells showed different frequency dependence and were sorted with high efficiency at 2 MHz and 20 Vpp, where more than 90 % of the viable cells and less than 10 % of the non-viable cells were captured on the DEP filter.

Finally, a novel real-time PCR microchip platform was developed with integrated thermal system and polymer waveguides for real-time PCR monitoring. The integrated polymer optical system was created in the SU-8 layer of the reaction chamber, without requiring any additional mask process. To realize real-time PCR, two suitable DNA binding dyes, SYTOX Orange and TO-PRO-3, were selected and added to the PCR mixture. The real-time PCR microchip was applied to detect *cad*F, a virulence gene of *Campylobacter jejuni.*

Since the μTAS devices described in this thesis are all mainly constructed with SU-8. A chemical treatment method for SU-8 surface was investigated to render the biocompatibility. The biocompatibility of the treated SU-8 surface was examined by different methods (including contact angle measurements, cell culture, cell morphology, cell growth kinetics, and the whole genome expression profiles microarray analysis). The whole genome expression profile microarray analysis can provide more detailed biocompatibility information of different polymer surfaces than other methods. The results also indicated that there might be no correlation between surface hydrophobicity and biocompatibility.

Contents

Appendix

Chapter 1: Introduction

1.1 Concept of μTAS

During the last decade, microfabricated devices for biological analysis has been generated based on the integrated circuit (IC) fabrication technologies. [1] The main goal is to miniaturize and to integrate a whole laboratory onto a microchip the so-called Micro Total Analysis System or μTAS in short. An ideal μTAS will integrate all the steps from sample preparation to final data representation of the analysis onto a single micro-device. The interest in μTAS devices has increased rapidly due to its low-cost, portability, and low reagents consumption. To date, various μTAS devices have been developed by different micro fabrication technologies, materials to apply in biochemical, chemical, and pharmaceutical research. [2-4]

Isolation and identification of cells (e.g. cancer cells) is extremely important in clinical diagnosis, molecular biological and pharmaceutical research. For realizing a real cell μTAS, several functional microstructures have been fabricated and tested in this thesis. A basic cell μTAS concept is shown in Fig. 1.1. It consists of cell sorting pretreatment system, cell incubation chamber, cell lysis and bio-molecular identification system.

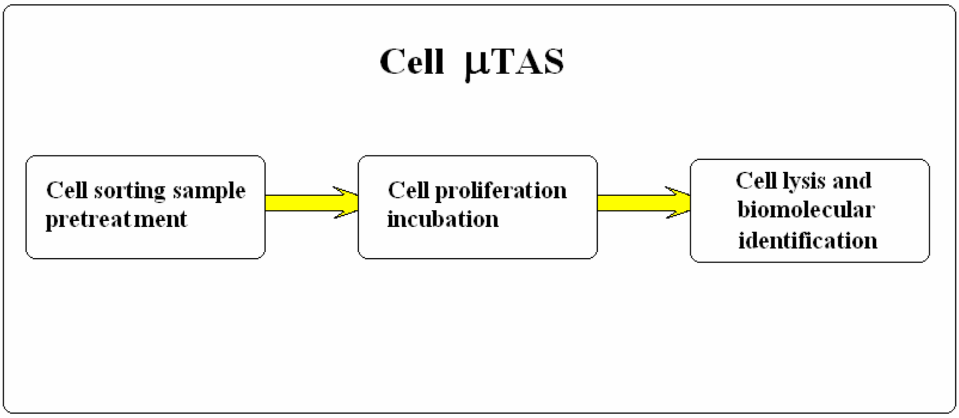

Figure 1.1 *Schematic of cell μTAS device concept. The whole device constitutes three major integrated systems: cell sorting, cell incubation, and cell lysis and biomolecular identification. An integrated microfluidic network connects these systems.*

In the first sample pretreatment step, the target cells will be sorted. The collected cells will be then transported into the micro cell incubation chamber for cell proliferation and enrichment. Finally, the enriched cells are lysed, the released biomolecules (e.g. DNA, proteins) are detected for the cell identification.

1.2 Integrated polymer optical system

To realize multiplex functionalities in a real μTAS device, integration of different sensors is critical for monitoring various parameters within the system. Optical detection is the most common method for detection in μTAS. Recent development of the optical detection in μTAS is reviewed by E. Verpoorte. [5] However, currently the most developed μTAS devices still use bulk optics for the optical measurements. The use of bulk optics has several drawbacks in terms of alignment, shock stability, and space occupation. Although very accurately aligned adapter can be fabricated for mounting the bulk optical system on a μTAS device, it is difficult to reform. In addition, the bulk optical systems are difficult to package together for real-time monitoring each microstructure in a combination μTAS device, because of the space limitation of the μTAS device and the miniaturization difficulties for free-space optical elements.

Several groups have inserted optical fibers directly in etched grooves [6, 7] or encapsulated fibers in polymer chips [8]. Recently, J.C. Roulet *et al.* (2002) reported an array of melted photoresist microlenses and chromium apertures deposited on the chip surfaces to form a micro optical system for enhanced signal treatment. [9] However, this micro optical system still needs to combine with bulk optics. Microlenses have also been integrated at the end of the fiber insertion groove for control of the beam shape. [10] Another approach is to use a light emitting diode (LED) as the light source for the microsystem. In 2002, J. Seo *et al.* has reported a packaging mode where light was coupled into the chip from the side using an external LED and integrated lenses for focusing. [11] Recently, a novel thin lay flat organic light emitting diode (OLED) has been packaged beneath a microfluidic channel for fluorescence excitation. [12] However, in all these approaches, the alignment and packaging was difficult and not very repeatable. Additionally, these approaches only allow a single detection point per fiber/LED. Although several fibers can be placed along a measuring channel it would be exceedingly tedious to realize a device as previously presented by Mogensen *et al.* [13], with more than one hundred measuring points. Therefore, the direct integrated fiber or LED approaches are limited to apply in complex devices.

In recent years, integrated optical system with planar optical waveguides (silicon nitride or doped silicon dioxide waveguides), has been monolithically integrated with microfluidic channels. [13-19] Comparison with bulk optical system, the integrated optical system provides more design flexibility and higher capacity. Furthermore, the alignment problem can be also solved at mask level, where the error can be down to a few hundred nanometers.

The principle of waveguides is quite simple. Usually, a waveguides consists a higher refraction index core layer and the surrounding lower refraction index buffer or cladding layers. Since all the integrated waveguides mentioned in this thesis are multimode waveguides, the light traveling in the waveguides can be explaned by ray-optic approach.

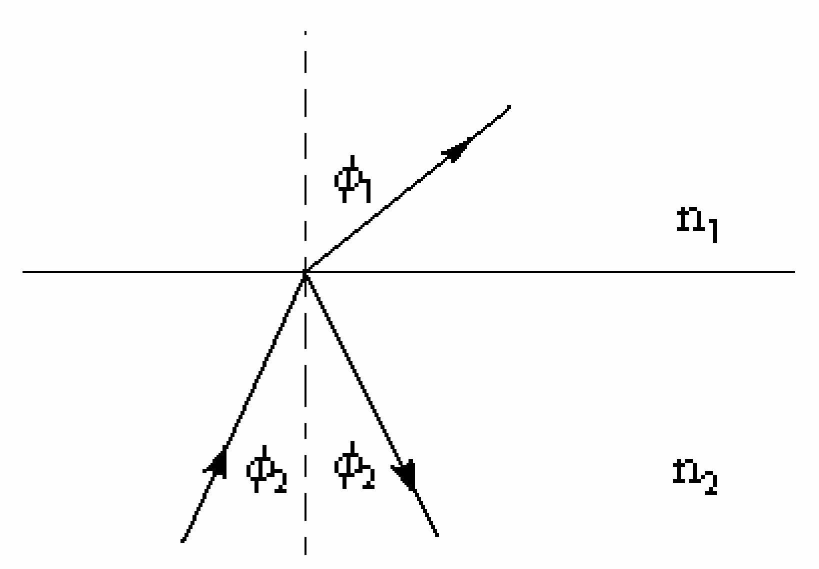

Figure 1.2 *Optical ray pattern of a standard radiation on the interface plane.*

Regarding to the Snell's law (Fig. 1.2), the relationship between incidence and refraction angle on the interface plane can be given by the flowing function (1.1).

$$\sin\phi_1 / \sin\phi_2 = n_2 / n_1 \qquad (1.1)$$

Since the n_l is smaller than n_2, the ϕ_l is always larger than ϕ_2. At a certain incidence angle, ϕ_l can become 90 °. Which means that no light refrect through the interface. This is also called total reflection. This special incidence angle is called the critical angle ϕ_c, given by the function (1.2).

$$\phi_c = 90° - \phi 2 = 90° - \sin^{-1}(n_1 / n_2) \qquad (1.2)$$

Therefore, once the angle of incidence in the waveguides is lower than ϕ_c, the light will be guided through the direction of core layer without leaking. The more complex theoretical calculations and many application samples (e.g. RF spectrum analyzer, integrated laser, and telecommunication systems) of the integrated planar waveguides can be found in the book of R.G. Hunsperger. [20]

However, silicon-based waveguides often need complex silicon micro-fabrication techniques. Those fabrication processes (e.g. thin-film deposition, anisotropic etching) normally request two to four photolithographic mask steps. Some fabrication process takes at least a couple of weeks or even a month, as in case of wet oxidization to convert the silicon waveguides into silicon dioxide waveguides. [21]

Conference name	The abstracts concerned about SU-8
MEMS 2004	13
μTAS 2004	41
MEMS 2005	11
μTAS 2005	26

Table 1.1 *The number of abstracts concerned about SU-8, which were presented on the recently important conferences.*

For low cost μTAS requisition, various optical quality polymeric materials have been invested to integrate polymer optics on the microchips by simple manufacturing procedures. [22-25] As an epoxy-based negative constructional photoresist, SU-8 is widely used for fabricating microstructures in various μTAS devices because of its excellent chemical stability [26, 27], optical properties [24, 28] and fast fabrication process [29]. Recently, many presented μTAS devices were constructed in SU-8 (as shown in Table 1.1).

In our lab, polymer waveguides made by SU-8 have been integrated with micro channels in a very simple fabrication procedure. The fluidic channels and optical elements (e.g. waveguides, lenses and fiber-to-waveguide couplers) were defined in the same layer of the negative photoresist SU-8. [24] This technology was applied to realize the real-time multiplex detection in several different microchips presented in this thesis.

1.3 Flow cytometry

Cytometry is one of the fundamental operations in the cell research. In traditional cytometry, different parameters (e.g. cell morphology) can be measured by taking microscope images of the cell smearing on a glass slide. Flow cytometry is now more often applied for studying physical and/or chemical characteristics of the cells or particles in clinical diagnostics, biochemistry and biology. [30] The picture of a typical flow cytometer and the operating principle of flow cytometer are shown in Fig. 1.3.

Principally, when the cells or particles pass in single file through the measuring apparatus in a fluid stream of flow cytometry, several parameters (e.g. scattering or fluorescent signals) that give different information of the cells or particles can be measured. The characters of different parameters that can be measured through flow cytometer will be mentioned in Chapter 2. Such delicate system is not only expensive (about 200,000 euro depended on types), but also requires especially trained person to operate. Therefore, miniaturization of flow cytometer is necessary and expected.

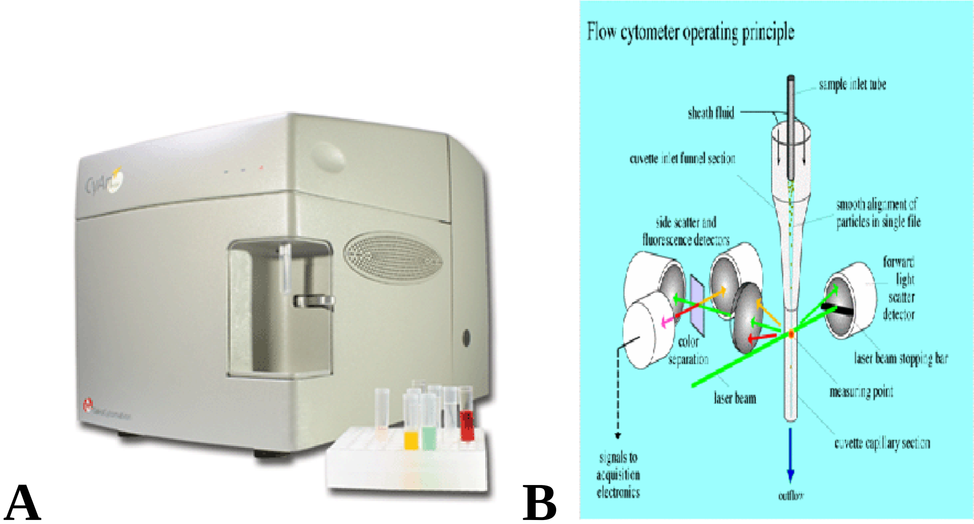

Figure 1.3. A: *A typical flow cytometer station (CyAn™ ADP, Dako, DK), including state-of-the-art optics (which includes 3 lasers (405 nm, 488nm, and 635nm), can provide 300 µl/min high throughput, 50,000 events/second fast analysis speed, and 4096 channels/parameter signal resolution), is about 30 cm wide x 45 cm deep x 40 cm high.* ***B:*** *The optical system setup for the different parameters measurements in a standard flow cytometer.*

In a cell µTAS, the microfluidic channel by itself serves a nature apparatus for a micro flow cytometer. Various micro flow cytometers have recently been developed by introducing incident light into the channel and optical systems for measuring the scattering or fluorescent signals. [31-37] The impendence of the passing cells can be also measured in the micro flow cytometers. [38] In the micro flow cytometers, the cells are aligned in the microfluidic channel centre to achieve the precise detection position, using the hydrodynamic [39], electrokinetic [40] or negative dielectrophoresis (DEP) [41] focusing. By doing so, these micro flow cytometers provide competent performances (similar coefficients of variation (CV)) as the conventional flow cytometers. However, most of the approaches mentioned above were still monitored by various bulk optical systems. In this thesis, an innovative micro flow cytometer with integrated optical system for real-time monitoring is presented in Chapter 2.

1.4 Cell sorting

Separation different types cell is a crucial step in sample pretreatment process in many clinical diagnostic and biological researches. Conventionally, different cells can be separated by e.g. gradient centrifugation, or by filtration. Combination of the cell fluorescent labeling with flow cytometer, the fluorescent activated cell sorting (FACS) technique provide impressively efficient sorting and high throughput (typically several ten thousand events per second). [42, 43] However, conventional FACS is expensive, difficult to sterilize, mechanically complex, and requires relatively large sample volumes as well as trained personnel for operation and maintenance. Several groups have developed micro FACS (μFACS) devices to realize the cell sorting process on a microchip. [44-53] The main drawback of these μFACS is the low sorting throughputs, which are highly limited by the fluorescence activated switch response in comparison to conventional FACS. Other groups have developed high throughput micro-devices where cells are sorted in continuous flow depending on size. [54, 55] A severe limitation of such systems is that the sorting is based purely on the cell sizes, which may not be the most relevant parameter for different sorting approaches. Another approach is magnetic sorting. [56-59] In this approach, magnet i.e. particles will be trapped by magnetic forces during the sorting process. This approach is therefore suitable for antibody immunization research by collection the magnetic beads with the antibody grafted on the surface. Electrokinetic techniques such as isoelectric focusing (IEF) [60] or dielectrophoresis (DEP) [61-63] are also a major approach for the micro sorting devices. In isoelectric focusing (IEF) the subcellular organelles and/or proteins are sorted by the isoelectric point, where the proteins or organelles achieve a neutral position under a pH gradient in an electric field. In dielectrophoresis (DEP), cells are sorted according to the cells permittivity, as described below.

To apply DEP, an alternating electric field will be formed to polarize particles or cells. As a good approximation, the polarized particle/cell can be represented by a dipole. Such dipole, in a non-uniform alternating electric field, is moved by a DEP force. [64] The direction of the DEP force is depended on the polarizability (permittivity) of the particle comparison with the suspending medium. If the permittivity of the particle or cell is higher than the medium, the force is toward the regions of high electric field gradient (positive DEP). Reversely, it will be a negative DEP. If the medium has the permittivity gradient, the non-uniform electric field can perform a DEP gradient. The DEP theory will be described in more detail in Chapter 4.

Depending on the conductivity of the fluid, positive DEP [65], negative DEP [66, 67], and DEP gradient [68, 69] has been applied to sort various cells or particles in microsystems. DEP has been also combined with field flow fractionation (FFF) [70] and traveling wave dielectrophoresis (TWD) [71] for separating malaria infected cells [72] or cancer cells [73-75] from normal cells. We have used DEP in a microsystem for PCR sample preparation. In this micro-device, positive DEP was used as a selective filter for capturing and holding cells in a sample while PCR inhibitors were flushed out. [76]

For the cell characterization, the DEP related technology of electrorotation (ROT) is widely applied. [77-82] In ROT, the particle or cell is rotated under a four phase alternating electric field. However ROT can only measure a single or a few cells each time. In contrast, flow cytometry can measure thousands of cells per second. In the Chapter 4, we present a novel microchip flow cytometer with an integrated DEP system. Using the microchip flow cytometer, the performance of the DEP filter (positive DEP) can be quantitatively real-time monitored by two micro flow cytometers integrated upstream and downstream of the DEP filter. It is an efficient way to study the effect of DEP on a large number of cells.

1.5 PCR on microchips

The cells selected by the sorting process need to be identified to summary the cell μTAS detection results, such as DNA analysis. Polymerase Chain Reaction (PCR) is an enzyme-catalyzed nucleotide amplification technique, routinely used in many different fields for genetic identification. To date, many different types PCR microchip have been developed. The PCR microchips can be classified into three main categories: a chamber, [83-96] a continuous flow, [97-100] and a droplet oscillation PCR chip design [101]. The chamber type PCR microchip is the first generation of PCR microchip. It contains large volume and has thermal cycles easily to control. [83, 84] The main drawbacks of the chamber type are the air-bubble generation and the packaging. In the continuous flow PCR, a meander microfluidic channel is designed to pass through three different heating zones. [97] However, this continuous flow PCR has also other drawbacks. Since the channel length is fixed, the thermal cycles cannot be changed. Recently, Wang, W. *et al.* (2004) invented a droplet oscillation PCR microsystem. [101] In this system, the droplet acts as a tiny reactor. The PCR mix-droplets were controlled to oscillate inside the microfluidic channel passing through the three different heating zones under required times. The system that controls the microfluidic in this PCR microchip is, however, rather complex.

Although PCR is a robust and predictable method, PCR itself cannot provide any information about the initial DNA template and the final product. In most cases, an end point PCR analysis (e.g. DNA gel electrophoresis) is required. A PCR integrated with gel electrophoresis microchip has already been developed. [102, 103] But due to the extremely complex control systems, the current trend is to fabricate into two separate microsystems then couple together. [104]

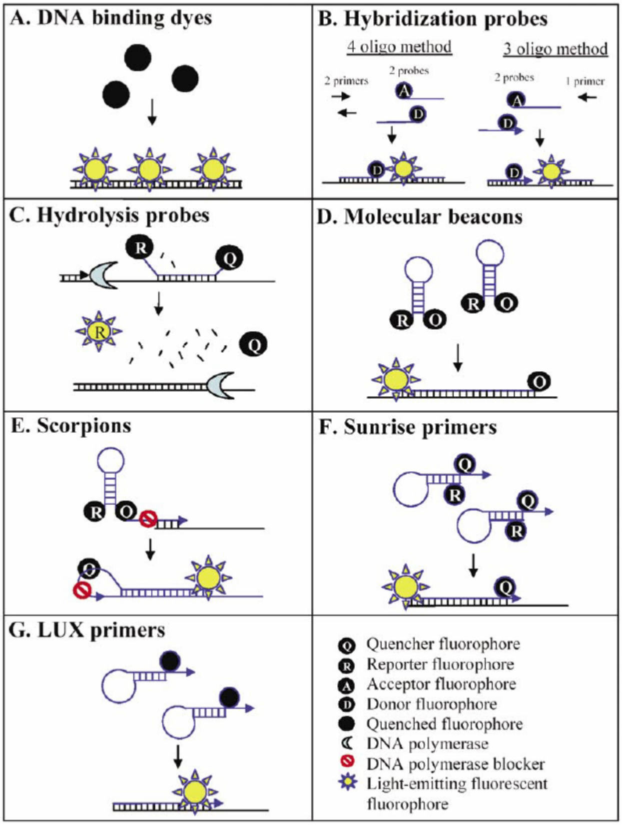

***Figure 1.4** The reaction mechanisms of DNA binding dyes and different DNA probes. [105]*

PCR quantification is difficult because the concentration of amplified PCR product can have large variations caused by minor disturbances, e.g. reaction components, thermal cycling fluctuation, or primer misalignment. [106] A solution to this problem is to use real-time PCR. In real-time PCR, the product formation is measured during the PCR reaction by using different fluorescence DNA binding dyes (e.g. SYBR green I [107, 108]) or by the real-time PCR probes (such as Hybridization probes [109], Hydrolysis probes [110, 111], and Hairpin probes [112-116]). DNA binding dyes will be fluorescent, only when they bind to double strand DNA. However, such binding is nonspecific. Real-time PCR probes can specifically bind to the DNA targets for the fluorescent reporting. But the prices of those probes are expensive due to the complex synthesizing. The chemistries of different real-time PCR fluorescence technologies are shown in Fig. 1.4. By using either dyes or probes, in a real-time PCR, the PCR amplification process can be visualized. The cycle threshold (C_T) value, the cycle number when the fluorescence intensity is higher than the detection baseline level, can provide more accurate and real-time quantitative information for the PCR amplification process. [105, 106] In 2002, Liu, J. et al. reported a nanoliter rotary

PCR microchip for the real-time PCR. [117] Recently, Gulliksen, A. *et al.* realized the real-time nucleic acid sequence-based amplification of RNA on nanoliter PCR microchips using a custom-made external optical system. [118, 119] However, there is no report on the integrated optics application in the real-time PCR microchip.

In pervious studies at the Cell and Particle Handling group at MIC, DTU, a PCR microchip with integrated thermal system for fast thermocycling has been developed. [120, 121] Based on this PCR microchip, in this thesis, a novel real-time PCR microchip with integrated polymer waveguides is developed and examined (Chapter 5). This new PCR microchip provides more accurately quantitative information about the DNA template, the PCR reaction dynamic inside the micro reaction chamber. The integrated polymer optics in this approach does not increase any extra cost and fabrication process.

1.6 Biocompatibility investigation of cell incubation in microsystems

In some case, the target cells obtained from a sorting process are limited. Therefore, incubation of the collected cells for cell proliferation will be a necessary step. The incubation systems for *in vitro* cell proliferation have been developed in many cell µTAS. [122-124] Most of them are fabricated based on polymer materials. [125-127] However, polymer materials often have both cytotoxic and positive effects in term of bio-functionality *i.e.* promotion or obstruction of biological processes of the cell in comparison to the reference surface. [128, 129] Thus the biocompatibility of the material surface for cell incubation needs to be rendered and investigated before application. There are a number of methods for biocompatible surfaces treatment that includes coating the surfaces with fibronectin [130-132], hydrophilic polymer materials [133], or O_2 plasma treatment [134]. However, those coatings may be laborious, expensive, and unstable over time. Biocompatibility investigation of a material surface can be examined by different methods, such as surface water contact angle [135], cell adhesion [136-138], cell spreading on the surface [139], cell proliferation rate [138], cell metabolic activity [138]. However, in some of the research it has been shown that decreasing water contact angle may not represent increasing biocompatibility. [140, 141]

Since most of structures of the cell µTAS presented in this thesis will be fabricated based on the negative photoresist SU-8. In Chapter 6, a simple, moderate and robust method for SU-8 surface chemical treatment for biocompatible is presented. The biocompatibility of the modified SU-8 surfaces is tested by different methods such as contact angle measurements, mammalian cell culture, cell morphology, cell-growth kinetics and whole genome expression profiling.

1.7 Outline of the thesis

The main theme of this Ph.D. project is to apply integrated polymer optical waveguides for the real-time optical monitoring the functionalities of the different cell μTAS and four applications have been investigated.

For detecting the cells in microfluidic channel, a micro flow cytometer with integrated polymer waveguides is developed. The micro flow cytometer is made based on negative photoresist SU-8 and is fabricated by a simple and fast process (Chapter 2). In addition, an application of the micro flow cytometer for detecting of fluorescence labeled cell using standard filter sets is investigated and presented in Chapter 3. A real application of a cell μTAS with two micro flow cytometers integrated upstream and downstream of a positive DEP filter for real-time monitoring yeast cell sorting is described in Chapter 4. Application of integrated polymer waveguides in a PCR microchip for detection of the variation of fluorescent signals in a real-time PCR is presented in Chapter 5. Since most of the main structures of the cell μTAS described in this thesis are fabricated in SU-8, different methods for measurement of the SU-8 surface biocompatibility are applied and evaluated in Chapter 6. Finally, a semi-standard bio-MEMS packaging mode for the fast bio-MEMS prototype packaging application is demonstrated in Chapter 7.

In this thesis, a number of successful applications of integrated polymer waveguides for real-time monitoring in various cell μTAS are demonstrated. The results presented here promote a promising possibility for the development of real practical μTAS in a near future.

Chapter 2: Measurements of scattered light on a microchip flow cytometer with integrated polymer based optical elements[†]

Z. Wang, J. El-Ali, M. Engelund, T. Gotsæd, I. R. Perch-Nielsen, K. B. Mogensen, D. Snakenborg, J. P. Kutter and A. Wolff*
MIC-Dept. of Micro and Nanotechnology, Technical University of Denmark (DTU), Building 345e, DK-2800 Kgs, Lyngby, Denmark. E-mail: aw@mic.dtu.dk; Fax: +45 4588 7762; Tel: +45 4525 6305

Received 15th January 2004, Accepted 17th March 2004, First published as an Advance Article on the web 20th April 2004

Flow cytometry is widely used for analyzing microparticles, such as cells and bacteria. In this paper, we report an innovative microsystem, in which several different optical elements (waveguides, lens and fiber-to-waveguide couplers) are integrated with microfluidic channels to form a complete microchip flow cytometer. All the optical elements, the microfluidic system, and the fiber-to-waveguide couplers were defined in one layer of polymer (SU-8, negative photoresist) by standard photolithography. With only a single mask procedure required, all the fabrication and packaging processes can be finished in one day. Polystyrene beads were measured in the microchip flow cytometer, and three signals (forward scattering, large angle scattering and extinction) were measured simultaneously for each bead. To our knowledge this is the first time forward scattered light and incident light extinction were measured in a microsystem using integrated optics. The microsystem can be applied for analyzing different kinds of particles and cells, and can easily be integrated with other microfluidic components.

2.1. Introduction

Flow cytometry is a powerful technology for analyzing chemicals, particles and cells in clinical diagnostics, biochemistry and biology. In flow cytometry cells or particles flow through an incident light beam in a sensing region and parameters such as scattered light and fluorescence are measured to provide information about the cells or particles of interest (Fig. 2.1). [30] Forward scattering (FS), also called small angle scattering, provides information on the size and viability of

---

[†] Reprint with permission from The Royal Society of Chemistry; Z. Wang, J. El-Ali, I.R.P. Nielsen, K.B. Mogensen, D. Snakenborg, J.P. Kutter, A. Wolff, "Measurements of scattered light on a microchip flow cytometer with integrated polymer based optical elements", *Lab on a Chip*, vol. 4, pp. 372-377, 2004.

cells or particles. FS is measured in a very narrow scattering angle range (0.5 – 5.0° to the incident light). Large angle scattering (LS) gives information of surface roughness and internal structures of cells or particles, such as cell internal granularity. LS can be detected in a broad scattering angle range (15 – 150° to the incident light). When a cell or particle passes through the light beam, the amount of direct light decreases due to a combination of absorbance and light scattering: This decrease is called extinction (EX). EX provides information on size, viability, and, *e.g.*, hemoglobin and protein contents. Since forward scattering has to be measured in a narrow scattering angle range, more precise alignment is required than for large angle scattering, extinction or fluorescence measurements. Consequently, FS is more difficult to measure than the other parameters. [30, 142] When flow cytometry is combined with cell sorting so-called fluorescent activated cell sorters (FACS) [43] are realized.

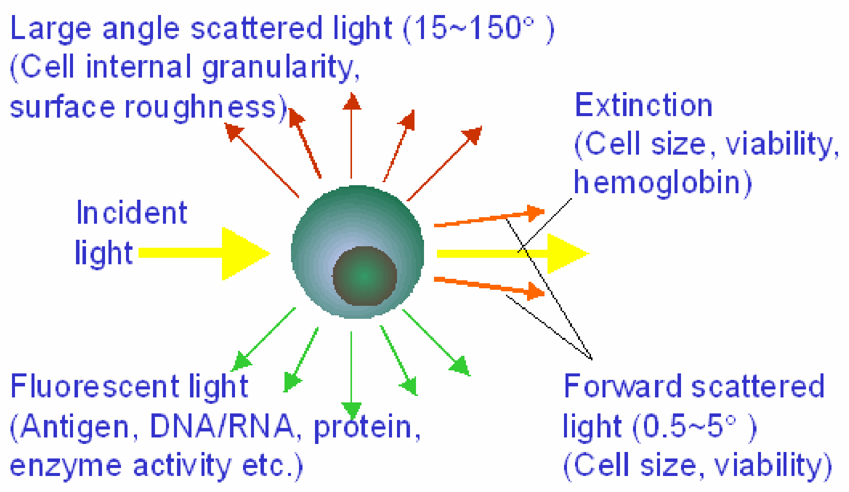

Figure. 2.1 *Measurement principle of flow cytometry. Cells or particles flow through an incident light beam in a sensing region and parameters such as extinction, scattered light, and fluorescence are measured. The different parameters provide various information about the cells or particles as indicated in the figure.*

In the past two decades, the microfabrication technologies developed for the microelectronics industry have been applied in chemistry, biotechnology, and pharmaceutics for miniaturization of different analytical instruments. [2-4, 143-149] Those technologies have also been utilized for miniaturizing flow cytometers [31-38, 40] and fluorescent activated cell sorters (µFACS). [44-48, 150] However, the vast majority of those microsystems used bulk optics for the optical measurements. This has drawbacks in terms of packaging because of alignment problems and shock stability. Furthermore, free-space optical elements are often difficult to miniaturize. E. Verpoorte has recently written a review on optics for microsystems. [5] An attempt to miniaturize free space optic systems was reported by Roulet *et al.* [9] who deposited an array of melted photoresist microlenses and chromium apertures on the chip surfaces to form a micro optical system for enhanced signal treatment. However, this micro optical system still had to be combined with bulk optics. Other groups have inserted optical fibers in etched grooves [6, 7] or encapsulated fibers in polymer chips. [8]

Microlenses have also recently been incorporated at the end of the fiber insertion groove for control of the beam shape. [10] Another approach has been presented where light was coupled into the chip from the side using an external LED and integrated lenses for focusing. [11] However, in all these approaches the insertion and precise alignment of either the optical fiber with the microfluidic channel or the LED with the microchip may be difficult. Furthermore, these approaches only allow a single detection point per fiber/LED. Even though several fibers can be placed along a measuring channel it would be exceedingly tedious to realize a device as the one previously presented by Mogensen *et al.*, [13] which had more than one hundred measuring points. The fiber approach is therefore of limited use for complex devices.

Planar optical waveguides monolithically integrated with microfluidic channels can provide good solutions to these problems. Microfluidic devices with integrated silicon nitride or doped silicon dioxide waveguides have been presented in recent years. [13-18] They were fabricated using silicon micromachining techniques such as thin-film deposition and anisotropic etching with the use of two to four photolithographic mask steps. The fabrication procedures were relatively complicated and took at least a couple of weeks.

Optical waveguides of polymeric materials can be made by simple manufacturing procedures. [22-25] In our lab, polymer waveguides have been integrated with micro channels using a very simple fabrication procedure where fluidic channels and optical elements are defined in a layer of the negative photoresist SU-8. [24] In this paper, we present a novel microchip flow cytometer with polymer optical elements (waveguides, lenses and fiber-to-waveguide couplers) integrated with microfluidic channels, which is suitable for high performance measurements of scattered light. Both fabrication and packaging are simple and fast, resulting in devices that can be made and tested in one day.

2.2. Experimental section

2.2.1. Design and fabrication of flow cytometer microchip

In the new microchip flow cytometer, the main innovative part is the integrated optical elements for measurement of scattered light. The design of these optical elements in the central part of the chip is shown schematically in Fig. 2.2.

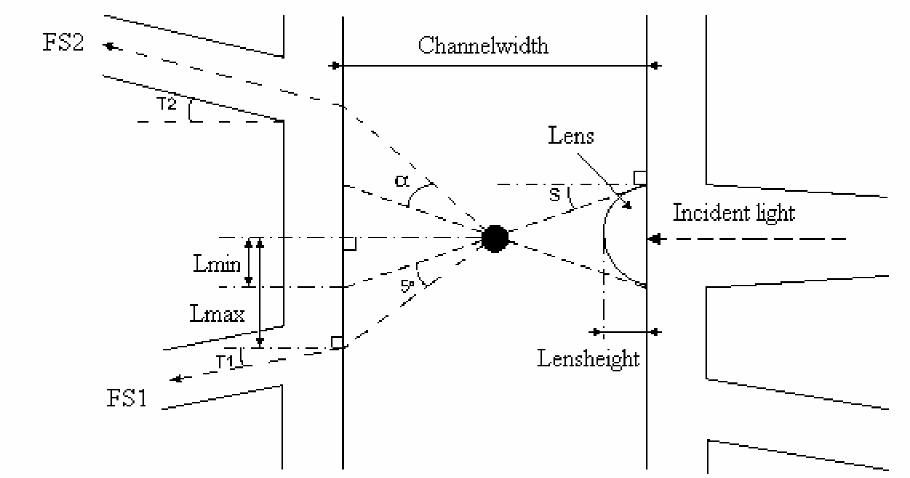

***Figure 2.2** Schematic of the geometry of the optical system in the central part of the chip (not to scale). The incident light comes from the tapered waveguide (to the right in the figure) and is focused by a lens to the center of the channel. When the focused incident light hits the particle light is scattered. Forward scattered light can only be measured in a window between the light path of the incident light and light scattered with an angle of 5°, i.e., between L_{min} and L_{max}.*

Incident light for the measurement is guided through a waveguide. The last part of this incident light waveguide expands in a tapered structure because recent experiments indicate that such structures ensure a higher degree of collimated light. [25] The waveguide ends in an elliptical lens (232 μm macroaxis and 130 μm brachyaxis) to focus the light at the center of the channel. Forward scattered light (FS) is measured in a narrow angle range (0.5 – 5°) and at the same time collection of too much direct incident light should be avoided because this will increase the noise level. Thus, the detection window of the FS waveguides should be located between the line of direct incident light and light scattered at an angle of 5° (Fig. 2.2). From simple geometry the angle (S) and the boundary (L_{min}) of the direct incident light beam on the channel wall can be calculated to be S = 11.5° and L_{min} = 56.9 μm from the centerline of the incident light waveguide. Due to refraction of the direct incident light beam on the water-SU-8 interface the minimum angle ($T1_{min}$) is $T1_{min}$ = 9.6°. Similarly, the boundary of the light scattered at 5° from the particle can be calculated to correspond to L_{max} = 68.4 μm and $T1_{max}$ = 13.7°. In the design, the distance L = 60 μm and the angle T1 = 10.1° was selected. Even though the center of the waveguide is located between the two boundaries, the detection waveguide also receives part of the direct incident light because the width of the waveguide is 30 μm, and the distance between the two boundaries is only 11.5 μm. The height of the waveguides (90 μm) is determined by the size of the external optical fiber, which has to fit in the fiber-to-waveguides couplers, while 30 µm was chosen as a practical minimum width to ensure mechanical stability of the waveguides. Although this direct incident light will increase the noise level it also enables the measurement of light extinction.

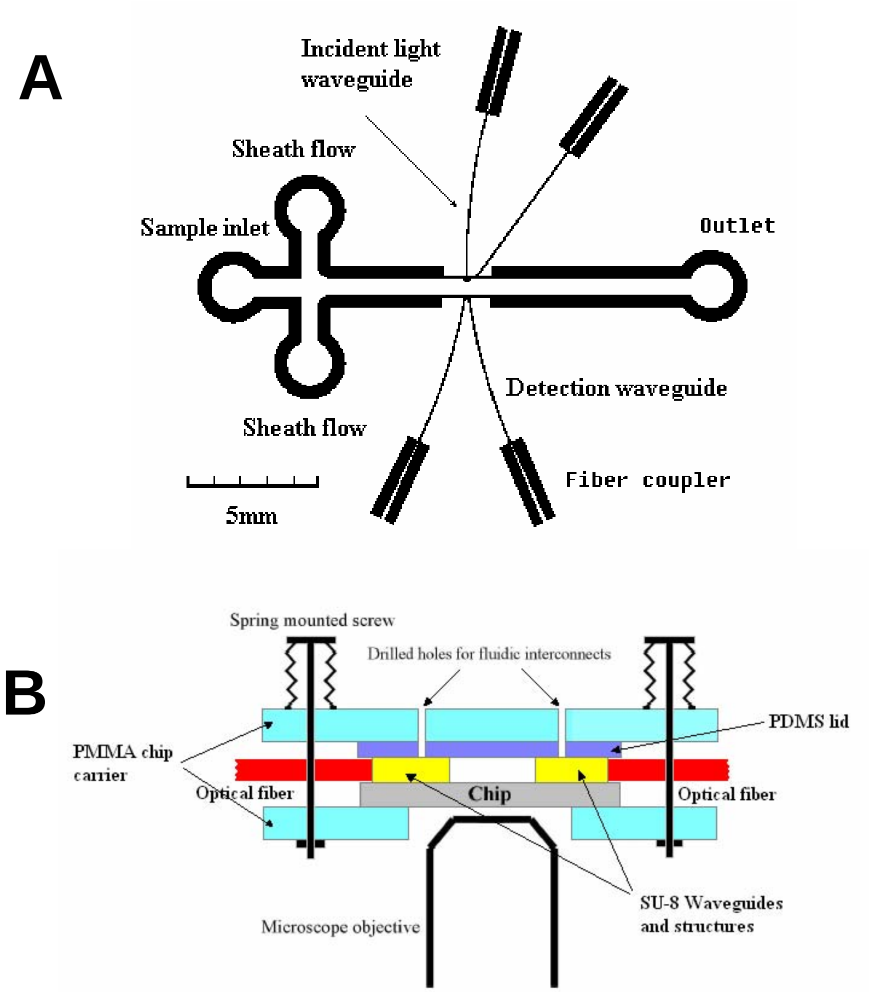

Figure 2.3 *Schematic of the microchip flow cytometer's structure and packaging.* ***A:*** *Design of the microchip flow cytometer. All the optical elements, the microfluidic system, and the fiber-to-waveguide couplers were defined in one layer of polymer.* ***B:*** *Schematic of the chip's packaging. The chip is placed in a holder and a PDMS lid (n = 1.4) was utilized to seal the flow channels and to serve as top cladding layer. The thickness of the SU-8 layer was adjusted to readily accommodate 70 µm outer diameter optical fibers in the fiber couplers.*

The design of the microchip flow cytometer is illustrated in Fig. 2.3A. The fabrication has been described previously. [24] Briefly, all the channels and optical elements were defined by standard lithography in a single layer of SU-8 negative photoresist (XP2075 Microchem, refractive index n = 1.59 at 633 nm). The microstructures were fabricated on a 4 inch 500 μm thick Borofloat glass substrate wafer (n = 1.46) (Schott corporation, Mainz, Germany). The glass wafers were cleaned in a “Piranha” solution (H2O2: H2SO4 = 1:3) for 10 min and subsequently dehydrated in a 250 °C oven for at least 3 h (to improve the adhesion of SU-8). Immediately after the wafer had cooled, a 90 μm SU-8 layer was spun onto the wafer (rotation speed 1800 rpm) and soft-baked on a hotplate (25 min at 95 °C, temperature ramp 7 °C min^{-1}). The wafer was cooled on the hotplate to room temperature and the structures were defined by UV lithography (900 mJ cm^{-2} at 365 nm), followed by a crosslink bake (25 min at 95 °C, temperature ramp 7 °C min^{-1}, cooled on hotplate). The SU-8 thin layer was developed in a propyleneglycolmonomethylether-acetate (PGMEA) solution (MicroChem, Massachusetts, US) for approximately 10 min to finish the fabrication of the chip.

The glass substrate (n = 1.46) served as waveguide buffer layer, while air (n = 1) acted as cladding on each side of the 30 μm wide waveguides. Finally, the flow channels were sealed by a PDMS lid (n = 1.4), which also served as top cladding layer. The PDMS lid was pressed down on the chip by spring-mounted screws (Fig. 2.3B). This gave a watertight and reversible sealing of the flow system. The thickness of the SU-8 layer (90 μm) was adjusted to readily accommodate 70 μm outer diameter optical fibers in the fiber couplers. The tapered groove of the coupler structure ensured self-alignment and thus very efficient coupling of light between fiber and planar waveguide. [24] The width of the microfluidic channel is 600 μm and the total dimensions of the chip are 16 mm × 14 mm.

2.2.2. Chemicals

Four different sizes of polystyrene beads (Polysciences, Inc. Warrington, PA, USA) were used in the experiment: 9.1 (±0.6) μm, 5.8 (±0.3) μm, 4.6 (±0.2) μm, and 2.8 (±0.1) μm, respectively. The beads were diluted in MilliQ water to the concentration shown in Table 2.1. A fluorochrome, Bodipy 650/665-X, (excitation at 646 nm, emission at 665 nm, Bio-Rad Laboratories, Inc. USA) was applied to visualize light paths in the optical system.

2.2.3. Equipment

Large angle scattered light was measured using an inverted microscope (Zeiss Axiovert 100, Carl Zeiss Co., Germany) with a 40× objective and a photo multiplier tube (PMT) (H6780–01, Hamamatsu Photonics K.K., Japan). Another PMT (H6780–02, Hamamatsu Photonics K.K., Japan) was used to monitor forward scattered light. A HeNe Laser (632.8 nm, max 5.8 mW, Melles Griot, USA) was used to provide incident light for the measurements and 70 μm outer diameter optical fibers (Polymicro Technologies, AZ, USA) served as external optical fibers. Three syringe pumps (Harvard Apparatus 22 Inc, Holliston, MA, USA) were used for pumping the sample and the sheathing flows.

***Table 2.1** Concentrations of different beads samples and the applied flow rates. Higher flow rates of bead-streams were used for larger beads to prevent settling of the beads in the channel.*

Size of beads (μm)	Concentration (bead/ml)	Flow rate of beads stream (ml/h)	Flow rate of sheath flow (ml/h)
9.1	2.68×10^6	1.0	2.0
5.8	2.54×10^6	0.5	2.0
4.6	5.09×10^6	0.1	2.0
2.8	8.63×10^7	0.03	2.0

2.3. Results and discussions

The microchip flow cytometer has one sample inlet and two sheathing flow inlets, one on each side of the sample inlet (Fig. 2.3A). The sample flow is hydrodynamically focused in the center of the main channel by the two sheath flows. In the measuring region in the center part of the chip, several optical elements are integrated with the microfluidic channel. These optical elements (lens, tapers and waveguides) are shown in Fig. 2.4A. The incident light waveguide seen perpendicular to the channel wall in the top part of the image is equipped with a lens for focusing of the light. At the opposite channel wall, there are two waveguides placed at certain angles for measuring scattered light. The waveguide to the right was used for measuring FS. The other waveguides seen in the picture were not used in the work described in this paper. The incident beam's light path was visualized by filling the channel with a fluorochrome (Bodipy 650/665-X, excitation at 646 nm, emission at 665 nm) (Fig. 2.4B). The focal plane of the lens is clearly seen near the center of the fluidic channel (the lens defined in SU-8 is a cylindrical lens and therefore has a focal plane rather than a focal point). From this image, the light intensities across the incident light path can be determined.

The light intensities of several important sections (labeled I, II, and III, in Fig. 2.4B) are shown in Fig. 2.5. The focal plane (265 ± 39 μm from the top channel wall) is not exactly at the center of the channel (320 μm from the top channel wall). However, the maximum value at the center of the channel is still 87% of the light intensity at the focal plane. The shift of the location of the focal plane is probably caused by a slight change in the refractive index of SU-8 or in the lens profile during the different baking processes. The lens is defined inside the channel and is as such an obstacle that, in principle, will perturb the flow path and cause a non-straight movement of particles in the region close to the lens. However, the lens height (40 μm) is less than 7% of the total channel width (600 μm) and the perturbation of the flow will therefore be limited. More importantly, the chip is designed for measuring particles that are hydrodynamically focused at the center of the channel where the effect of the perturbation will be negligible.

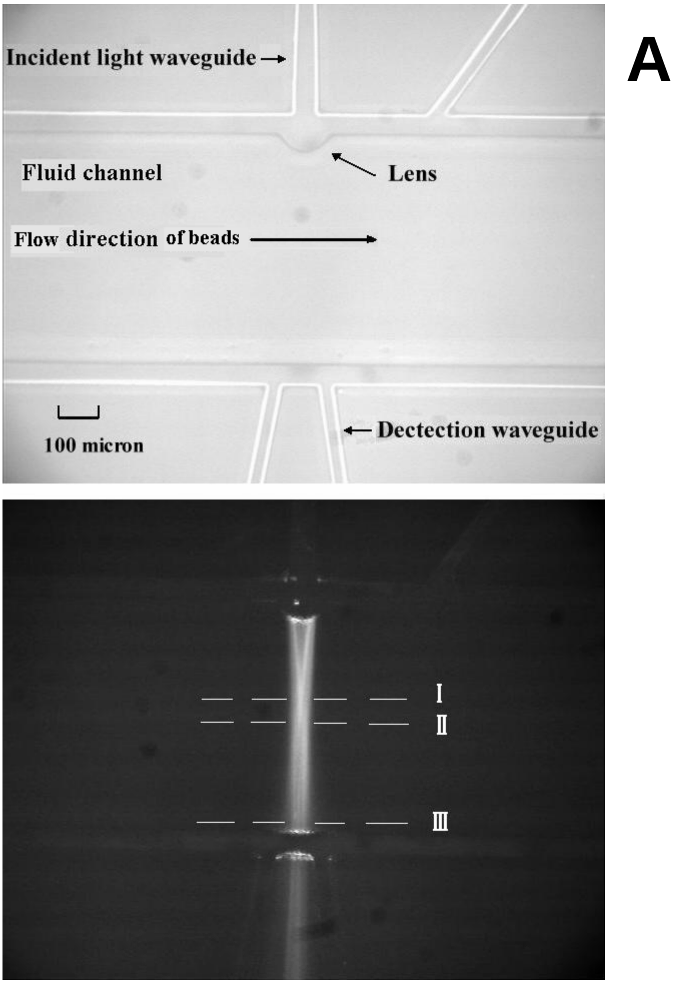

Figure 2.4 *Microscope images of the polymer optical system at the center of the microchip.* ***A:*** *Bright field image. The incident light waveguide that can be seen perpendicular to the channel wall in the top of the picture is equipped with a lens for focusing the light. At the opposite channel wall, there are two waveguides placed at certain angles for measuring FS.* ***B:*** *Fluorescence light image (same field of view as in Fig. 2.4A). The incident light path is visualized by filling the channel with a fluorochrome. In Fig. 2.5 cross sections of the light intensity are shown. These cross sections are labeled here for reference: focal plane (I), center of channel (II), and edge of the bottom channel wall (III).*

The right of the two waveguides at the channel wall seen at the bottom of Fig. 2.4A was used for measuring FS. In Fig. 2.5 the detection window of this FS waveguide is indicated together with the light intensity along the bottom channel wall. From this figure it is estimated that less than 13% of direct incident light will arrive at the FS detection window. This part of incident light constitutes the background level of the forward scattered light measurements, but, at the same time, allows the FS waveguide to be used for measuring extinction signals. However, if too much direct light were received by the FS waveguide it would have increased the noise to an unacceptable level.

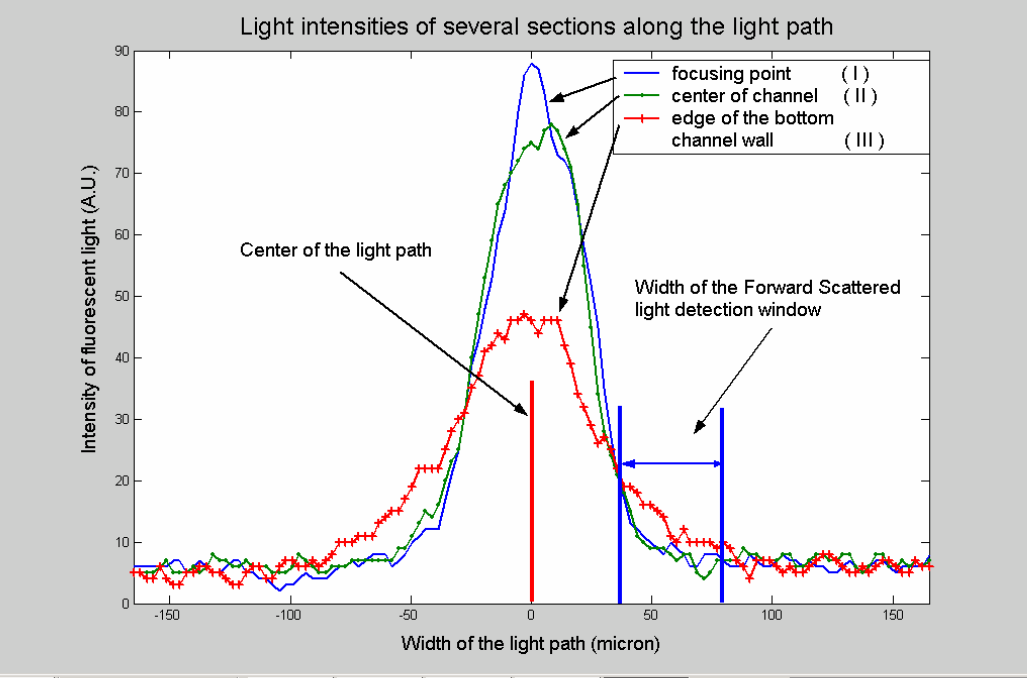

Figure 2.5 *Light intensities of several sections at different locations along the incident light path (labeled in Fig. 2.4). The width and location of the detection window of the forward scattered waveguide is indicated in the figure. It is estimated that this waveguide received 13% of the incident light.*

For measuring bead samples, incident light from a HeNe laser (632.8 nm) was introduced through an external optical fiber coupled to the incident light waveguide, then focused by the integrated SU-8 lens (Fig. 2.4B). Forward scattered light was measured through the right detection waveguide. However, as described above, this waveguide also received a small amount of direct incident light. Consequently, as a bead passed through the light beam a positive forward scattered light (FS) peak is observed first, followed by a negative extinction (EX) peak as a result of the bead blocking part of the incident light (Fig. 2.6). Simultaneously, large angle scattered light (LS (90°)) was measured vertically through the inverted microscope objective. Thus, for each bead three signals (FS, LS, EX) were recorded simultaneously. In this study we have chosen to measure

LS using a known technique, *i.e.*, to measure LS through the objective of the inverted microscope (Fig. 2.3B). We could thus compare the information obtained by our new method (FS and EX measured through the detection waveguide (Fig. 2.4A)) with the results obtained by the established method. There is an agreement in time between the LS and FS signal, whereas the EX signal follows a few milliseconds later (Fig. 2.6). The established method thus confirmed the information obtained by our new method. In future studies, we will measure all signals using integrated waveguides hereby avoiding the requirement for external free space bulk optics.

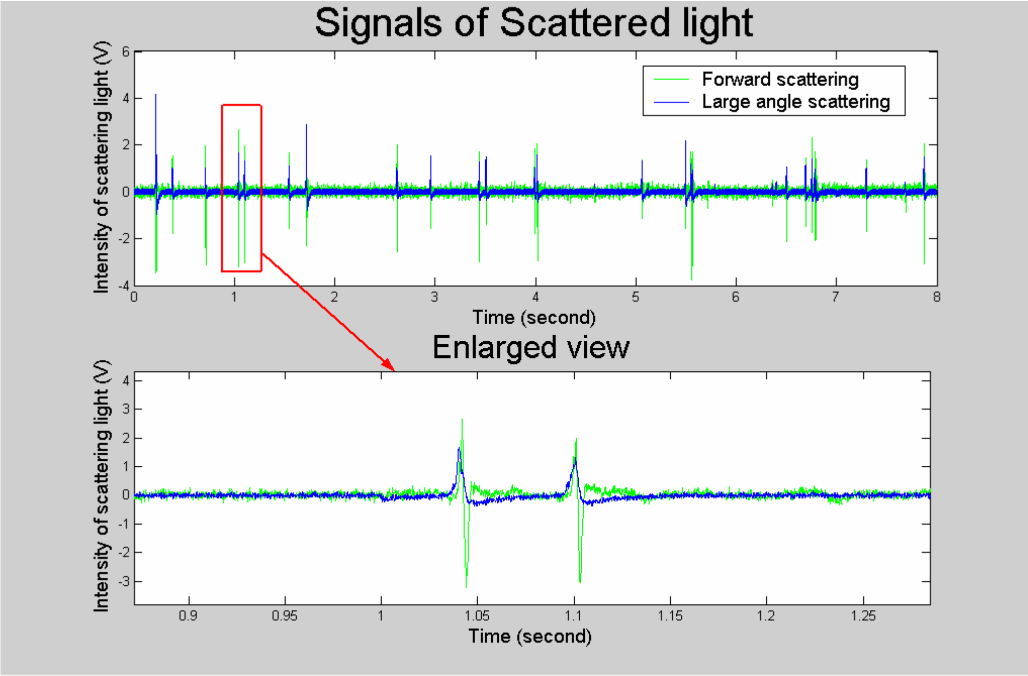

Figure 2.6 *Typical scattered light signals. When a bead passes through the light beam a positive forward scattered light (FS) peak is detected by the FS waveguide first, followed by a negative extinction (EX) peak as a result of the bead blocking part of the incident light. Simultaneously, large angle scattered light (LS (90°)) was detected vertically through the microscope objective.*

The main disadvantages of using bulk optics for microfluidic systems are the size, susceptibility to shock, and alignment problems. The integrated optics presented here are much reduced in size in comparison to bulk optics. In addition, the monolithic integration of the optics with the microfluidic system ensures excellent shock stability. Furthermore, the alignment is done once and for all on the mask design level where the accuracy is as good as a few hundred nanometers. Moreover, mask-to-mask alignment is avoided since a single mask is used for defining both the optical and fluidic system. The microchip flow cytometer can therefore be reproduced with the full fidelity of the photolithographic process.

In order to test the performance of this microchip flow cytometer, samples of polystyrene beads of different sizes (2.8, 4.6, 5.8, and 9.1 μm diameter) were percolated through the chip at a flow rate of 0.1–1.0 ml h^{-1}. The concentrations of beads and the applied sample flow rates are summarized in Table 2.1. The beads were sheathed and hydrodynamically focused in the center of the main fluid channel by a flow of 1 ml h^{-1} MilliQ water through each of the two sheath flow channels (Fig. 2.3). Three syringe pumps were used, one for the sample flow, and two for the sheath flows.

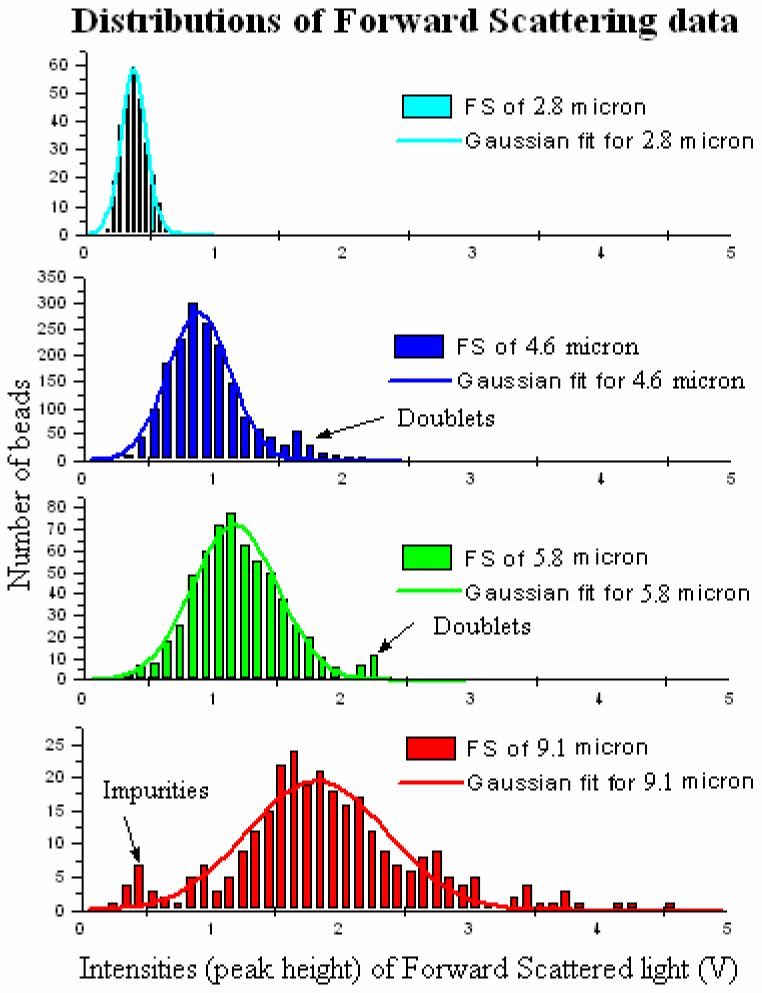

__Figure 2.7__ Distribution of forward scattered light intensities (peak height) for four different bead sizes. The different bead sizes can be distinguished from the

distribution of the intensities of the scattering signals. In the histograms for 4.6 and 5.8 µm beads an additional small peak is seen at twice the average intensity caused by two beads (doublets) passing through the detection area simultaneously. In the histogram for 9 µm beads an extra peak is seen in the low intensity area. This is due to an impurity of smaller particles in the beads sample.

During the measurements the throughput of beads was 4–25 beads s^{-1} (4–25 Hz). The widths of the signal peaks from the beads were around 10 ms. The minimum distance between beads should be at least twice the signal peak width. This would limit the maximum theoretical throughput to 50–65 Hz. However, increasing the flow rates will increase the linear velocity of the beads and thereby decrease the peak width and increase the theoretical throughput. Another possibility to increase the throughput is to decrease the width of the detection window or to narrow the incident light path.

The scattering signals from the measured beads were plotted in histograms of the signal intensities (peak heights). The histograms of forward scattered light intensities are shown in Fig. 2.7 for the four different bead sizes. From those histograms, the coefficients of variation (CV), defined as the standard deviation divided by the mean of the signal intensity, can be determined. The CV is 26.6%, 27.4%, 28.2% and 29.7% for 2.8, 4.6, 5.8 and 9.1 µm beads, respectively. These results are comparable to results obtained with other microchip flow cytometers. [34, 35, 40] However, the CV in the microchip flow cytometer is still high in comparison to conventional flow cytometers. [30] This might be caused by several reasons: Firstly, the ratio of sheath flow to sample flow is much lower than in a conventional flow cytometer. Secondly, in the chip flow cytometer we used syringe pumps, which produced a slightly pulsing flow especially at low flow rates. In contrast, in conventional flow cytometers, the sheath flow is driven by air pressure to create very stable, pulse-free flows. Thirdly, in the chip flow cytometer the sample flow was only sheathed on the two lateral sides but not from the top and the bottom. This may give a greater variation in comparison to conventional flow cytometry, where the sample is sheathed and hydrodynamically focused from all four sides. [48] In our lab, we have developed a microfabricated coaxial flow structure for hydrodynamic sample focusing in flow cytometers and cell sorters. [48, 151] In future works this structure will be included in the microchip flow cytometer and the operation of the chip will be modified to bring the CV down to the level of conventional flow cytometers. In the histograms for 4.6 and 5.8 µm beads an additional small peak is seen at twice the average intensity (Fig. 2.7). When two beads (doublets) pass through the detection area simultaneously this will give rise to the extra peak. In the histogram for 9 µm beads an extra peak is seen in the low intensity area. This is due to an impurity of smaller particles in the beads sample.

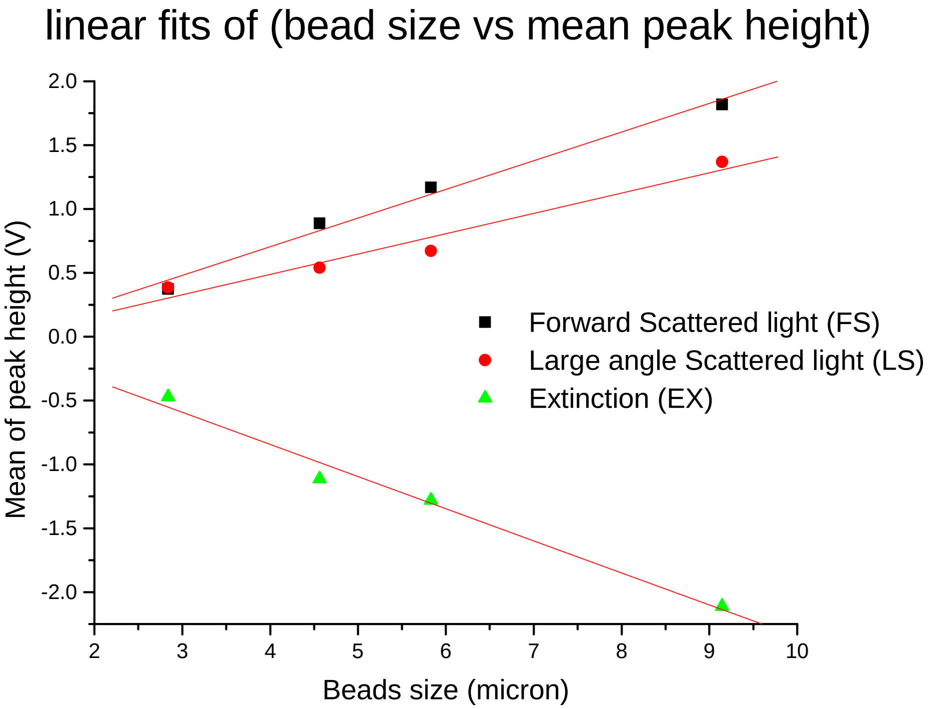

Figure 2.8 *Mean peak heights for FS, LS, and EX plotted as a function of bead size and fitted by linear regression. Linear Regression for FS:* $Y = -0.19356 + 0.22449 \times X$, *(R = 0.99403, SD = 0.08046); Linear Regression for LS:* $Y = -0.14844 + 0.15912 \times X$, *(R = 0.97882, SD = 0.10871); Linear Regression for EX:* $Y = 0.1608 - 0.25121 \times X$, *(R = - 0.99118, SD = 0.10972).*

Based on the distributions of the measured signal peak heights, the means of the FS, LS, and EX values were extracted after fitting to a Gaussian (only the fits for FS are shown in Fig. 2.7). Mean peak heights were plotted as a function of bead size and fitted by linear regression (Fig. 2.8). The relationship between the signal intensities and the size of the beads shows that FS and EX have more dependence on the particle size than LS as seen from the slopes, which are: FS: 0.22, EX: -0.25, LS: 0.16. This is in agreement with findings in the literature, which state that FS and EX provide information on particle size, whereas LS can display information about the internal structures or surface roughness of the particles. [30, 31] Here, LS only yielded information about the beads' surface roughness since all the polystyrene beads are solid. In future experiments, the microchip flow cytometer described here will be used to measure fluorescence (FL) labeled cells.

Then four parameters (FS, LS, EX, FL) can be measured simultaneously for each cell in the microchip flow cytometer.

2.4. Conclusions

To our knowledge, this is the first time forward scattered light and incident light extinction was measured in a microsystem using integrated optical elements. Polymer optical elements including waveguides, lenses and fiber-to-waveguide couplers were integrated with microfluidic channels to form a microchip flow cytometer. The microfluidic system and all the optical elements were defined in one polymer layer (SU-8) by standard photolithography in a single mask procedure. This approach allows the fabrication and packaging of an entire device to be completed in a single day. Four different size polystyrene beads were tested in this micro device, and three different signals (forward scattering, large angle scattering and extinction) were measured simultaneously for each bead. The different bead sizes could be distinguished based on their signal intensities' histograms. The relationships between the means of the signal peak heights and the size of the beads also confirmed the viewpoints expressed in the literature, [30, 31] namely that forward scattered light and extinction provide information on bead size, and large angle scattered light reveals information on the surface roughness of the beads. This microsystem can be applied for analyzing different kinds of cells or particles, and can easily be integrated with other microfluidic components.

Acknowledgements

We thank undergraduate students Monika Omonkowska and Bartlomiej Jan Blus for their adjustments of the test setup. We also thank Dr Dang Duong Bang (Danish Institute for Food and Veterinary Research, Aarhus, Denmark) and MSc Per Wolff (Chempilots, Farum, Denmark) for their critical review of the manuscript. The research was supported by the Danish Technical Research Council (STVF) (Grant nos. 26-02-0307 and 26-00-0220).

Chapter 3: Fluorescence analysis in microchip flow cytometer

As described in Chapter 2, flow cytometry is a versatile technology for measuring particles and cells. Major application of flow cytometery technology is analysis of fluorescence labeled cells. In this chapter, the microchip flow cytometer with integrated polymer optical elements (waveguides, lenses and fiber-to-waveguide couplers) was applied for measurements of fluorescence labeled beads and cells. All the optical elements and the microfluidic system were monolithically defined in one SU-8 polymer layer by standard UV photolithography, similarly to the design described in Chapter 2. [152] Different signals (forward scattering, large angle scattering and fluorescence) were measured simultaneously for each bead or cell type. The fluorescence signals of the fluorescence labeled beads and cells were obtained through the integrated waveguides (with a band pass filter in front of the PMT) or an inverted fluorescence microscope, respectively.

3.1. Chip structure

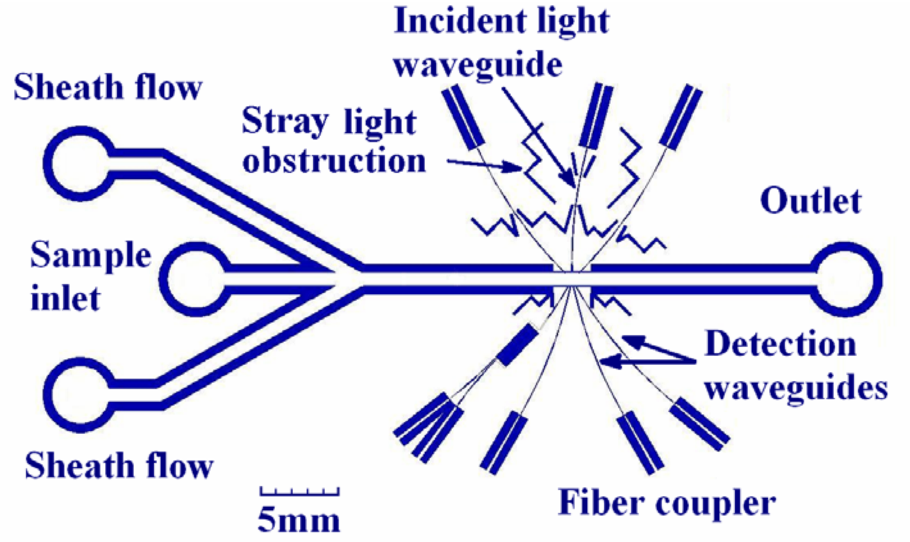

Figure 3.1. *Overview of the chip structure, the flow channel width is 466μm. Some straight light obstruction elements are included to reflect unwanted direct light.*

In the design of this microchip flow cytometer, some stray light obstructions were placed around the waveguides to reflect the unwanted straight light. By using the similar fabrication process as mentioned in Chapter 2, the fluidic and optical systems (as shown in Fig. 3.1) were defined by standard lithography on a single

SU-8 layer on top of Pyrex substrate. Since only one mask step process, therefore the chip fabrication is rather simple and quick. Again all the fabrication and packaging can be finished in one day.

In the microchip flow cytometer, particles or cells were hydrodynamically focused in the channel center by two sheath flows. An incident light from an Ar ion laser (488nm, as the excitation light) was focused to the center of the channel by an integrated SU-8 cylinder lens (Fig. 3.2) for excitation the fluorescence dyes. Fig. 3.2A shows a clear focused light path, when the channel was filled with FITC (fluorescein 5-isothiocyanate, excitation 494 nm/emission 518nm) fluorescence dye solution.

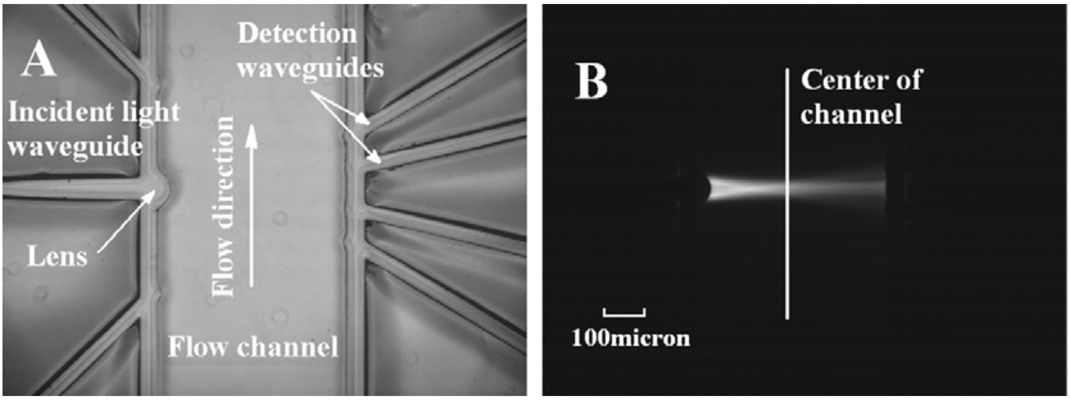

Figure 3.2. A and B: *Image of the integrated polymer optical system (A) and visualization of the light path (B). In the detection area, several waveguides were designed for collecting light scattered from the particles at different angles (Fig. 3.1 and Fig. 3.2A). The incident beam light path was visualized by filling the channel with a green fluorescence dye (B).*

3.2. Experimental section

6 µm and 10 µm Fluresbrite^{TM} plain YG (excitation 494 nm/emission 518nm) fluorescence beads (Polyscience, Inc., USA) were selected for the initial tesing of the micro flow cytometer. Two red blood cells, the rainbow trout red blood cells (RTRBC) and chicken red blood cells (CRBC), were used as the real biological sample to test the performing of the microchip flow cytometer. The cells were obtained from the Finsen Lab, University Hospital, Copenhagen, Denmark. The cell nuclei were stained with propidium iodide (Sigma, USA) (PI, excitation 538 nm/emission 617 nm). The staining protocol is listed in the Appendix F.

Fluoresence signal was measured using an inverted microscope (Zeiss Axiovert 100, Carl Zeiss Co., Germany) with a 40× objective and a photo multiplier tube (PMT) (H6780–01, Hamamatsu Photonics K.K., Japan). Two different band pass filters (BP 520/10 and BP 620/10, DELTA Light & Optics, Denmark) were set in front of the PMT to filter the received incident light. Another PMT (H6780–02, Hamamatsu Photonics K.K., Japan) was used to monitor large angle scattering light from the integratd waveguides. An Ar ion Laser (488 nm, max 400 mW, Lg-laser technologies, German) was used to provide incident light for the measurements and 70 µm outer diameter optical fibers (Polymicro Technologies, AZ, USA) served as external optical fibers. Three syringe pumps (Harvard Apparatus 22 Inc, Holliston, MA, USA) were used for pumping the sample and the sheathing flows.

3.3. Results and discussions

The chip was initially tested using Fluresbrite^{TM} plain YG (excitation 494 nm/emission 518nm) beads (Polyscience, Inc., USA). The fluorescence light emitted from the beads was measured by one of the waveguides and a PMT with a band pass filter (525 nm/22 nm). The distribution of the fluorescence signal intensities (peak heights) for two different sizes of fluorescence beads (5.7 and 10.8 µm diameter) is shown in Fig. 3.3A.

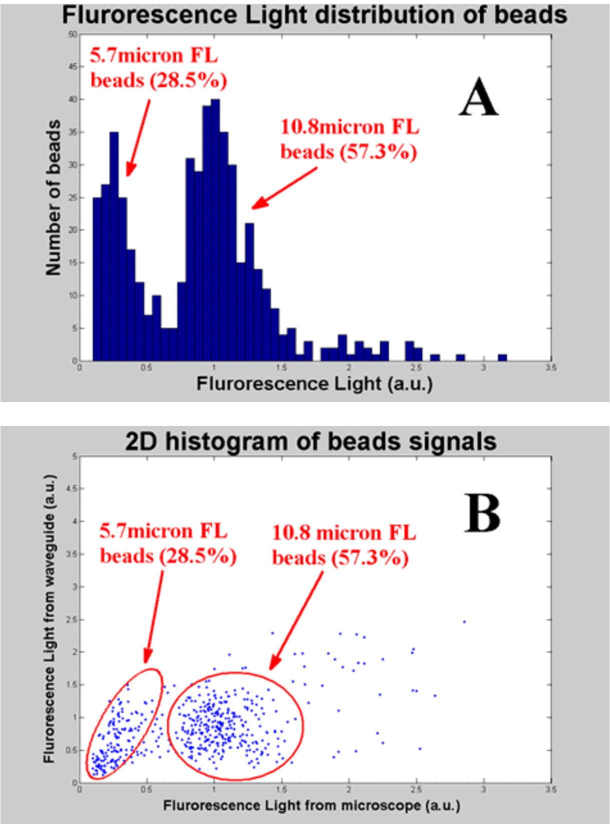

Figure 3.3. A: *Fluorescence signal distribution of two different sizes of fluorescence beads.* ***B:*** *2D histogram of fluorescence signals from the two*

different sizes of fluorescence beads measured using a waveguide and an inverted fluorescence microscope.

The beads with two different sizes can clearly be distinguished through the inverted fluorescence microscope and the ratio of the fluorescence signal intensities is about 1:3, which is close to the ratio of surface areas of the beads. However, due to the high fluorescent background [153] and high propagation loss [24] of SU-8 material at the low wavelength area, the fluorescence signals measured through the SU-8 waveguides are not distinguishable.

In the following real cell analysis, two different red blood cells, Rainbow trout red blood cells (RTRBC) and chicken red blood cells (CRBC), were selected for testing the performance of the microchip flow cytometer. Propidium iodide (PI, excitation 538 nm/emission 617 nm) was selected for labeling the cell nuclei. PI can provide relatively higher wavelength emission light than FITC. Even so, the fluorescence signal measured through the integrated SU-8 waveguides was much lower than the signal direct from the reverse microscope. This is mainly caused by the high propagation loss of SU-8 in the low wavelength range. One alternative is using higher wavelength fluorescence dye, such as deep red dyes.

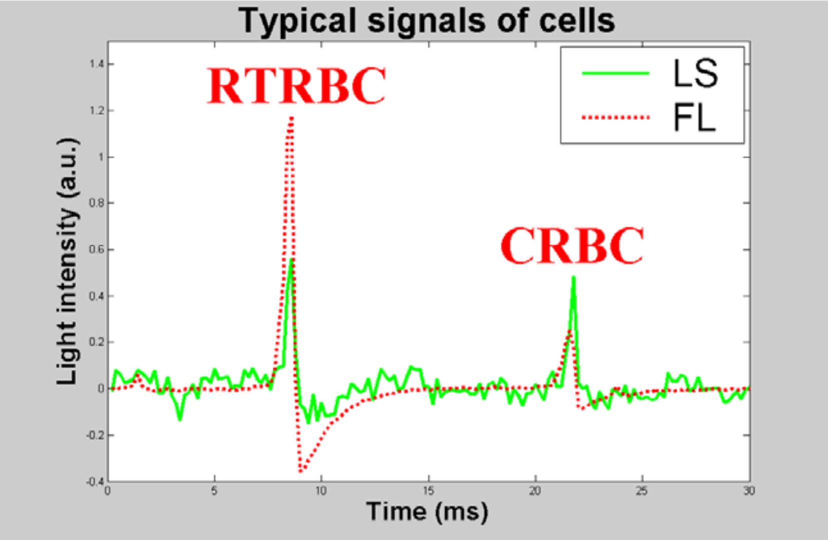

Figure 3.4. *The graphs of typical large angle scattering (LS) and fluorescence (FL) signals of two different types of red blood cells measured by the microchip flow cytometer. The LS is measured through the integrated waveguides. The FL is measured through reverse microscope.*

The two red blood cells have same sizes but different in DNA contents. Once the cell nuclei were stained with PI [154], the fluorescence signals of two different cells would be completely different. A graph of typical fluorescence and large angle scattering signals are shown in Fig. 3.4. There was little difference in the scattering signals since the sizes of both types of cells were close to 3 μm. In contrast, the fluorescence signal was quite different for the different DNA contents. The fluorescence signals intensities of PI dyed RTRBC were 3 fold stronger than PI dyed CRBC. This is in agreement with the literature [155]. Furthermore, from the 1D and 2D distributions of the fluorescence light, the two kinds of cells can also be clearly distinguished (Fig 3.5).

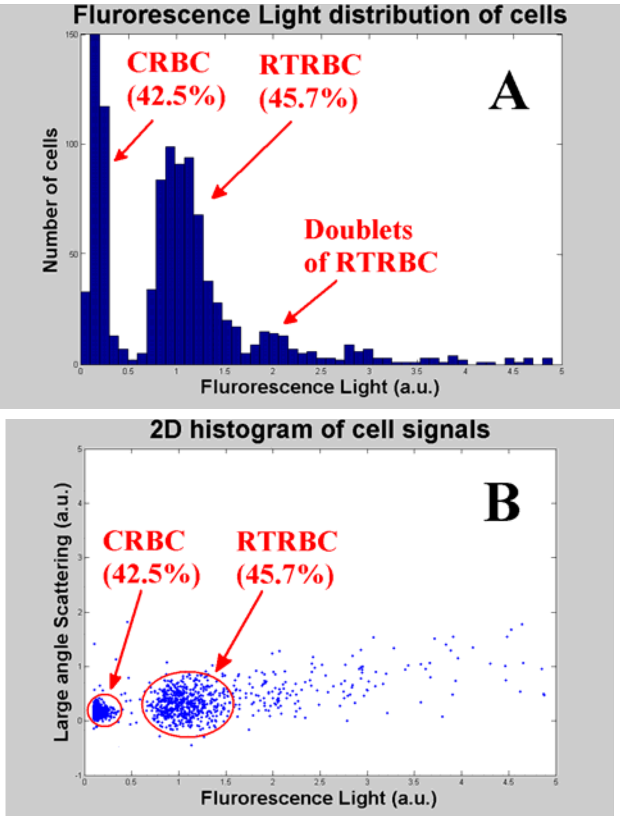

Figure 3.5. A: *Fluorescence signal distribution of two different types of red blood cells (CRBC and RTRBC).* ***B:*** *2D distribution of large angle scattering and fluorescence signals for the two different types of red blood cells.*

3.4. Conclusions

In this chapter, the applications of the microchip flow cytometer for measuring the fluorescence and scattering light of both fluorescence labeled particles and cells are presented. However, due to the high propagation loss of SU-8 in the low wavelenth, the performance of the SU-8 waveguides for the blue light excited fluorescence measurements is not so good. Either changing the fluorescent dye, or changing the waveguides materials might solve this problem. At MIC, a new doping PMMA waveguides fabrication method has been developed [156], but it requires a micro milling machine and is therefore difficult for mass production realization. In the current stage, the SU-8 waveguides is still the most realizable and simplest way to achieve the mass production of integrated polymer optical elements.

Acknowledgments
Many thanks to Dr. J.K. Larsen and Dr. J. Christiansen for kindly providing us cells and staining methods.

Chapter 4: Dielectrophoresis microsystem with integrated flow cytometers for on-line monitoring of sorting efficiency †

Z. Wang[1], O. Hansen[1], P.K. Petersen[1], A. Rogeberg[1], J.P. Kutter[1], D.D. Bang[2] and A. Wolff[1,*]

[1]MIC – Department of Micro and Nanotechnology, Technical University of Denmark, DTU Bldg. 345∅, DK2800, Kgs. Lyngby, Denmark. E-mail: aw@mic.dtu.dk; Fax: +45 4588 7762; Tel: +45 4525 6305
[2]Department of Poultry, Fish and Fur Animals, Danish Institute for Food and Veterinary Research, DK-8200, Århus, Denmark.

Dielectrophoresis (DEP) and Flow cytometry are powerful technologies and widely applied in microfluidic systems for handling and measuring cells and particles. Here, we present a novel microchip with a DEP selective filter integrated with two micro flow cytometers (FC) for on-line monitoring of cell sorting processes. On the microchip, the DEP filter is integrated in a microfluidic channel network to sort yeast cells by positive DEP. The two micro flow cytometer (FC) detection windows are set upstream and downstream of the DEP filter. When a cell pass through the detection windows, the light scattered by the cell is measured by integrated polymer optical elements (waveguide, lens, and fiber coupler). By comparing the cell counting rates measured by the two FC's, the collection efficiency of the DEP filter can be determined. The chips were used for quantitative determination of the effect of flow rate, applied voltage, conductivity of the sample, and frequency of the electric field on the sorting efficiency. A theoretical model for the capture efficiency was developed and a reasonable agreement with the experimental results observed. Viable and non-viable yeast cells showed different frequency dependence and were sorted with high efficiency. At 2 MHz, more than 90 % of the viable and less than 10 % of the non-viable cells were captured on the DEP filter. The presented approach provides quantitative real-time data for sorting a large number of cells and will allow optimization of the conditions for, e.g., collecting cancer cells on a DEP filter while normal cells pass through the system. Furthermore, the microstructure is simple to fabricate and can easily be integrated with other microstructures for lab-on-a-chip applications.

---

† Submitted to Electrophoresis in Jul. 2006

4.1 Introduction

Conventional fluorescent-activated cell sorters (FACS) are widely used in clinical medicine, basic biological and material sciences. FACS provides impressively efficient sorting. [42, 43] However, conventional FACS is expensive, difficult to sterilize, mechanically complex, and requires relatively large sample volumes as well as trained personnel for operation and maintenance. Several groups have developed micro FACS (μFACS) devices to realize the cell sorting process on a microchip. [45-49] However, for most of these μFACS the sorting throughputs were very limited in comparison to conventional FACS. Other groups have developed high throughput microdevices where cells are sorted in continuous flow depending on size. [54, 55] A severe limitation of such systems is that the sorting is based purely on cell size, which may not be the most relevant parameter for many sorting problems. Dielectrophoretic sorting has been developed as a major sorting process in microsystems. [61-63] In dielectrophoretic sorting cells are sorted by the cell permittivity and such sorting processes can, e.g., be used for sorting living cells from dead cells or cancer cells from normal cells.

Dielectrophoresis (DEP) is an electrokinetic technique, where polarizable particles move due to an applied alternating electric field. Dielectrophoresis is widely used to manipulate, sort, and measure cells in various microsystems. [61-63] In an alternating electric field a particle or cell will polarize. The polarized particle can to a good approximation be represented by a dipole, which, in a non-uniform electric field, experiences a net time averaged force that will move the particle. [64] The DEP force is proportional to the volume of the particle, the gradient of the time averaged electric field energy density, and the real value of the effective polarizability of the particle. The effective polarizability of the particle is a function of the complex permittivity of the particle and the surrounding medium. It follows that the polarizability is frequency dependent when the medium and/or the particle has a finite conductivity. The frequency dependence is described by the real value of the Clausius-Mossotti factor, [64] $K(\omega)$, where ω is the angular frequency. Since the dielectrophoretic force is proportional to the gradient of the electric field energy density, which in turn is proportional to the electric field strength squared, a reduction of the electrode spacing will dramatically increase the DEP force. This advantageous scaling of the DEP force with electrode spacing makes DEP very suitable for manipulating cells in microsystems.

The direction of the DEP force is depending on the effective polarizability of the particle in the suspending medium. If the complex permittivity of the particle is lower than that of the medium, the force is toward the regions of low electric field gradient (negative DEP), $0 > \mathrm{Re}[K(\omega)] \geq 0.5$. If it is higher, the force is toward the regions of high field gradient (positive DEP), $1 \geq \mathrm{Re}[K(\omega)] > 0$.

The effective polarizability of cells is determined by intrinsic parameters such as the type of cell, morphology, internal structure, membrane integrity, and physiological state, [61, 77] and DEP can therefore be used for separating and characterizing cells. The effective polarizability of cells is often modeled using a multi-shell model where each shell is assigned a thickness and a complex permittivity, which reflects the rather intricate internal structure of the cells. [64, 157-159]

DEP and the related technique of electrorotation (ROT) [80] have, e.g., been used for characterizing different blood cells, [82] cell viability [77-79, 81] and the influence of biocide on cells. [80] DEP has also been combined with field flow fractionation (FFF) [70] and traveling wave dielectrophoresis (TWD) [71] for separating malaria infected cells [72] or cancer cells [73-75] from normal cells. We have used DEP in a microsystem for PCR sample preparation. Positive DEP was used as a selective filter for capturing and holding cells in a sample while PCR inhibitors were removed. [76] Other groups have also used positive DEP. [160, 161] However, all of these experiments were either only qualitatively characterized or used external methods for quantifying the sorting results, e.g. counting chamber or conventional flow cytometry.

Flow cytometry is a powerful method for analyzing particles and cells in clinical diagnostics, biochemistry and biology. [30] In flow cytometry, cells or particles flow through an incident light beam in a sensing region, and parameters such as scattered light and fluorescence are measured to provide information about the cells or particles. In contrast to DEP and ROT cell characterizing methods, where only a single or a few cells are measured, with flow cytometry thousands of cells can be measured per second. Several groups have made microfabricated flow cytometers. [40, 45, 48, 152] The vast majority of those microsystems used bulk optics for the optical measurements, which has drawbacks in terms of packaging because of alignment problems and shock stability. Furthermore, free-space optical elements are often difficult to miniaturize. We have recently presented a SU-8 based microchip flow cytometer with integrated polymeric optical elements (waveguides, lenses, and fiber couplers). [152] In this microchip the microfluidic and optical systems were fabricated by standard photolithographic steps in a single SU-8 layer. We hereby not only solved the problems of alignment and shock stability of bulk optics measurements, but also facilitated the integration with other microsystem elements. In the present study, we present a novel microchip, which demonstrates the ability to integrate several functionalities and several flow cyrometers in a simple two mask level fabrication process. The microsystem we have chosen for demonstrating this is a combination of a DEP filter and two micro flow cytometers (FC's). The performance of the DEP filter (positive DEP) can be quantitatively monitored in real-time using the flow cytometers integrated up- and downstream of the DEP filter. Since the DEP properties of live/dead yeast is well documented, [77] yeast was chosen as a model system to test our novel chip.

4.2 Experimental Section

4.2.1 Chip Design, Fabrication and Packaging

The layout of the DEP microchip flow cytometer is shown in Fig. 4.1A. The design comprises a fluid channel network, DEP filter electrodes, a four-electrode conductivity measurement cell, and optical circuitry for two flow cytometers up- and downstream of the DEP filter in an 18 × 21 mm^2 chip. The fluidic channel network allows sheathing of the sample flow between two buffer flow streams. At the inlets and outlets the fluidic network is provided with wells for liquid access to the chip. In the 400 µm wide flow channel a 5 mm long DEP filter with castellated electrodes is integrated. Castellated electrodes have already been shown to be efficient for capturing cell by positive DEP. [74, 76] The minimum DEP electrode distance is 10 µm and the center-to-center electrode distance is 40 µm. The optical waveguide network for the flow cytometers includes waveguides (30 µm wide, 90 µm tall), fiber-to-waveguide couplers and a 3dB (50/50) beam splitter, which provides the incident light for the two micro flow cytometers from a single light source. A cylindrical lens with radius 41.5 µm is integrated at the end of the incident light waveguides to improve the transmission of light at the center of the flow channel. The detection waveguides is set at 5° to the incident light direction in order to receive forward scattering light, which provides the size information of the passing cell. The design and fabrication details about the micro flow cytometer using SU-8 waveguides are described in our recent publication. [152] The flow channels and all the optical elements were fabricated in SU-8 using a single mask step. A microscope image of a part of the chip at the downstream end of the DEP filter including the downstream flow cytometer is shown in Fig. 4.1.B.

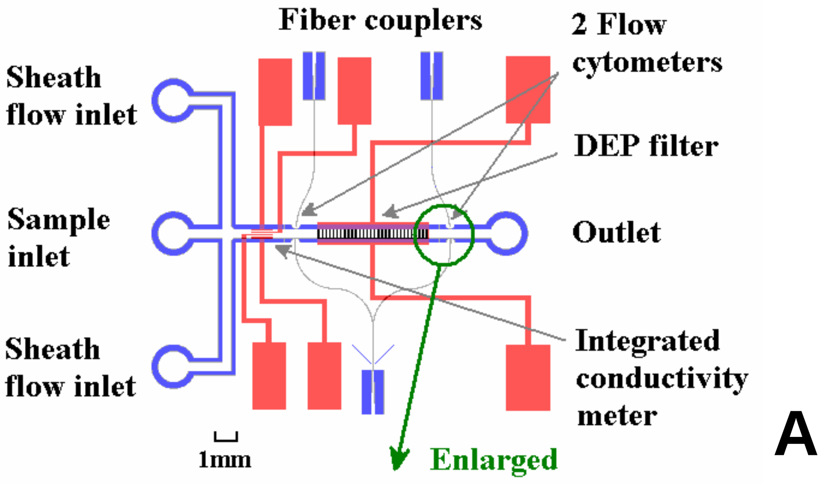

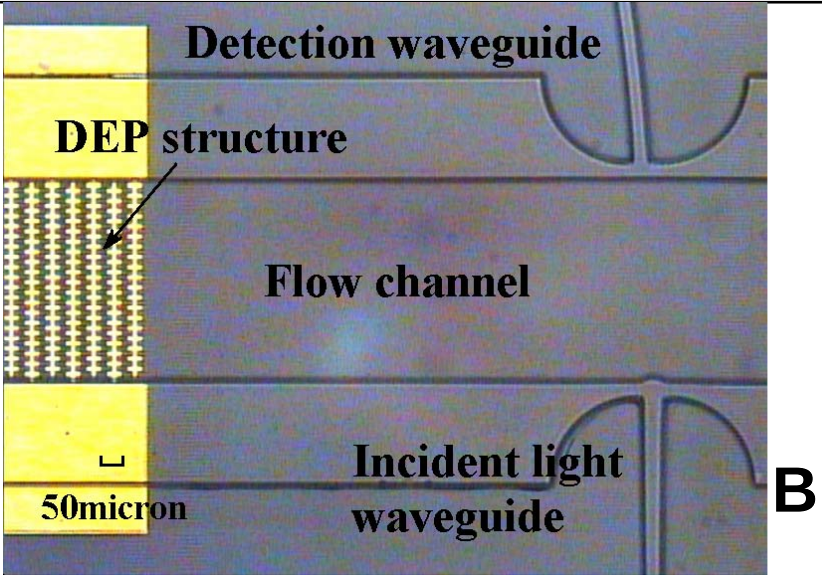

Figure 4.1 A) *Schematic of the lay-out of the chip structure.* ***B)*** *Microscope image showing part of the DEP filter and the downstream flow cytometer (2nd FC). Cells flowing through the FC were excited by light from the incident light waveguide and the forward scattered light was measured using the detection waveguide. The DEP filter has 62.5 pairs of DEP electrodes, the distance between the electrodes is 10μm, and the entire DEP structure is 5mm long.*

The DEP-microchip flow cytometer fabrication process needs only two photolithographic masking steps for defining electrodes and SU-8 structures respectively. In the first masking step electrodes of 200 nm Au on 10 nm Ti, deposited by e-beam evaporation, were defined using a standard lift-off process on 500 μm thick 100 mm diameter borosilicate glass substrates (Borofloat, Schott Corporation, Germany). Then, all the fluidic and optical systems were created by standard lithography in a 90 μm thick SU-8 layer (XP 2075, MicroChem, USA), with a refractive index n = 1.59 at 632.8 nm, as described previously. [152]

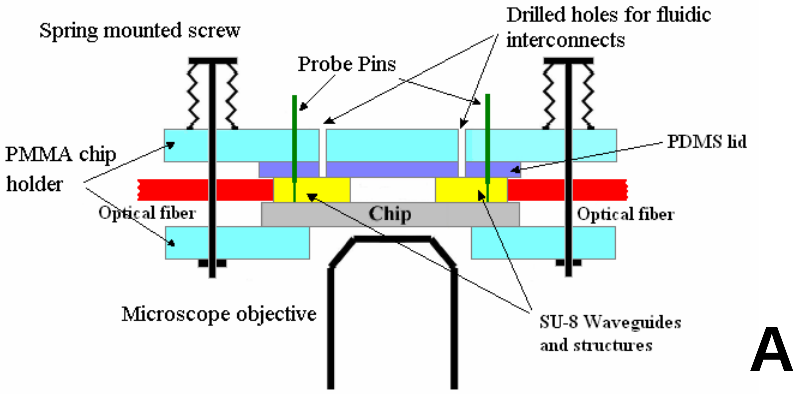

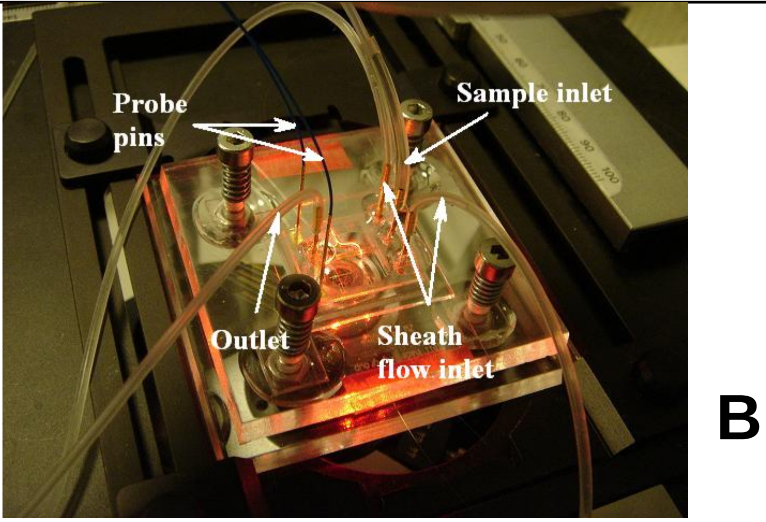

Figure 4.2 A) *Schematic outline of the microchip and the dedicate test jeg providing fluidic, optical, and electrical interconnects to the microchip.* ***B)*** *The picture shows the chip mounted in the test jeg. Probe pins are used to connect the DEP electrodes to an AC generator and optical fibers are used for coupling light in and out of the chip.*

The flow channels were sealed by a PDMS lid, with a refractive index n = 1.4, which also provides top cladding to the waveguides as shown in Fig. 4.2A. The borosilicate glass substrate, with a refractive index n = 1.46, provides the lower cladding of the waveguides, whereas air provides cladding to the vertical waveguide surfaces. The thickness of the SU-8 layer was adjusted to readily accommodate 70 μm outer diameter optical fibers (FVP050055065, Polymicro Technologies, AZ, USA) in the fiber couplers. Copper probe pins with 0.75 mm outer diameter (100426-004-922, Interconnect Device Inc., KS, USA) were used for electrical connections to the electrodes on the chips. A photograph of the DEP microchip flow cytometer mounted in a dedicated test jig providing fluidic and electrical interconnects to the chip is shown in Fig. 4.2B.

4.2.2 Cell Preparation

Yeast cells (*Saccharomyces cerevisiae*) were selected as model cells to test the performance of the DEP microchip flow cytometer. The yeast cells were grown overnight at room temperature on Yeast extract Peptone Dextro (YPD) medium: 10 g yeast extract (Mast group Ltd, UK), 20 g bacto peptone (International Diagnostics Group plc, UK), 20 g glucose (Merck, Germany), and 1000 mL water. The cells were collected by centrifugation at 1000 rpm (112 × g) for 5 min, at room temperature. The yeast cells were washed once with MilliQ water and suspended in MilliQ water to a final concentration of 10^6 cells/mL. FITC labeled yeast cells were obtained by suspending 10^8 cells in 1 mL FITC solution prepared from 1 mg/mL fluorescein 5-isothiocyanate (FITC) (Sigma chemical Co., USA) in 0.05 M sodium carbonate/bicarbonate buffer, pH 9.6 (C-3041, Sigma chemical Co., USA). The FITC and yeast cell mixture was incubated at room temperature for 30-60 min. After the staining, the FITC molecules were conjugated with the cell membrane proteins. [162] The FITC labeled cells were washed 3 times by centrifugation at 1000 rpm (112 × g) for 5 min and resuspension of the cell pellet in MilliQ water. Non-viable yeast cells were prepared by heating a cell suspension (30 mL) in a microwave oven at 1500 W for 30 seconds.

4.2.3 Instrumentation

A HeNe Laser (632.8 nm, max 5.0 mW, Melles Griot, USA) was used to provide incident light for the forward scattering measurements. 70 μm outer diameter optical fibers (FVP050055065, Polymicro Technologies, AZ, USA) were used for coupling the laser light into the incident light waveguides on the DEP-flow cytometer chip. Two photo multiplier tubes (PMT) (H6780-01, Hamamatsu Photonics K.K., Japan) were used to monitor the forward scattering signals of the cells from the two flow cytometers. The chip was placed on a Zeiss Axiovert 100 inverted microscope (Carl Zeiss Co., Germany) which was used for fluorescence measurements. Epi-fluorescence excitation light for the fluorescence measurements was provided by a 100 W mercury lamp (XBO75W/2, Carl Zeiss Co., Germany) through a band pass filter (489/22 nm) with 20× or 40× objectives on the microscope. The fluorescent emission light was collected through the same objective and another band pass filter (535/44 nm), and measured by another PMT (H6780-02, Hamamatsu Photonics K.K., Japan) fitted on the microscope. Two syringe pumps (Harvard Apparatus 22 Inc., MA, USA) were used for pumping the sample and sheathing flows. The AC voltage to drive the DEP filter was provided by a multichannel AC generator (Wavetek model 195, CA, USA).

4.3. DEP Capture Theory

In this section we derive an expression for the capture efficiency, which will allow comparison of the experimentally obtained results with theoretical expectations. In the derivation we shall ignore thermal effects, since we are primarily interested in modeling the capture efficiency in low conductivity media, where the thermal effects are small. The inclusion of thermal effects would complicate the analysis considerably and is beyond the scope of this paper. As a result the validity of the theoretical results is restricted to low conductivity media, where the thermal gradients due to Joule heating are so small that the resulting thermal gradient driven fluid flow can be ignored. The derivation is based on the expression for the time-averaged DEP force, [64] $<F_{DEP}>$, on a particle with volume ν in a non-uniform alternating electric field with peak amplitude E

$$< F_{DEP} >= \frac{1}{4} \nu \operatorname{Re}\left[\tilde{\alpha} \right] \nabla E^2 , \tag{1}$$

where $\tilde{\alpha}$ is the (complex) effective polarizability of the particle. For a uniform spherical particle immersed in a fluid with the permittivity ε_f the effective polarizability is $\tilde{\alpha} = 3\varepsilon_f K(\omega)$. [64] The frequency dependent Clausius-Mossotti factor, $K(\omega)$, is dependent on the complex permittivities of the fluid, $\tilde{\varepsilon}_f = \varepsilon_f - i\sigma_f / \omega$, and of the cell or particle, $\tilde{\varepsilon}_c = \varepsilon_c - i\sigma_c / \omega$, where $\tilde{\varepsilon}_f$ and $\tilde{\varepsilon}_c$ are the conductivities of the respective media [64]

$$K(\omega) = \frac{\tilde{\varepsilon}_c - \tilde{\varepsilon}_f}{\tilde{\varepsilon}_c + 2\tilde{\varepsilon}_f}. \tag{2}$$

It follows that the time averaged DEP force on a uniform spherical particle of radius R is

$$< F_{DEP} >= \pi R^3 \varepsilon_f \operatorname{Re}[K(\omega)] \nabla E^2. \tag{3}$$

Obviously, the real value of the Clausius-Mossotti factor, which can assume values in the range $-0.5 \leq \operatorname{Re}[K(\omega)] \leq 1$, plays an important role in determining the direction of the force.

Consider a DEP filter of length L in a flow channel of width W and height h, with W >> h. We shall use Cartesian coordinates with the x-axis along the length and the z-axis along the height of the channel. The filter has a two-phase periodic electrode structure where the electrodes are driven by the AC voltages $V(t) = \pm V_0 \sin(\omega t)$. The fluid flow in the channel is assumed to be a Poiseuille flow with the flow velocity [163] $v_f \cong [(1 - z/h) z/h] 6Q/(Wh)$, where Q is the flow rate, and z the elevation in the channel.

The collection efficiency, ξ, of the DEP filter is defined as the ratio of the number of cells captured per unit time on the filter to the number of cells entering the filter per unit time. If it is assumed that all cells entering the filter at an elevation less than or equal to $z_0 < h$ are caught in the filter, then the efficiency is

$$\xi(z_0) \equiv \frac{\int_0^{z_0} C v_x dz}{\int_0^{h} C v_x dz} \cong \left(\frac{z_0}{h}\right)^2 \left(3 - 2\frac{z_0}{h}\right) = u_0^2 (3 - 2u_0), \tag{4}$$

where C, which is assumed constant, is the concentration of cells in the solution, v_x is the longitudinal cell velocity, which is assumed equal to the liquid flow speed v_f, and $u = z/h$ is the normalized elevation.

In order to find the elevation $z_0 = hu_0$, below which all cells are assumed caught, the equation of motion for the cells must be solved. Since the momentum relaxation time for the cells ($\tau = (2\rho R^2)/(9\eta) \approx 5\mu s$) is very short compared to the time-scale of the experiments, inertial forces can be ignored. Therefore, only the viscous drag force F_{drag}, the DEP force F_{DEP} and the gravitational force F_g need to be considered. The balance between these forces determines the cell velocity, v_c. Assuming spherical cells, the viscous drag force is obtained from Stokes' equation [163]

$$F_{drag} = 6\pi\eta R(v_f - v_c)\,. \tag{5}$$

Since inertial forces are ignored, the component of the drag force in the *x*-direction is assumed to be zero, which gives the result used above, $v_x = v_f$. The force of gravity is only important at low applied voltages to the DEP filter. For a spherical cell with the mass density difference Δρ compared to the fluid, the force of gravity is [163]

$$F_g = \frac{4}{3}\pi R^3 \Delta\rho g\,, \tag{6}$$

where g is the gravitational acceleration.

The DEP force depends strongly on the geometry of the DEP filter, and is a complicated function of the position of the cell. However, for simple periodic electrode structures Morgan et al.[164] have calculated a simple approximation to the force valid at elevations larger than ~ 0.7d, where d is one quarter of the wavelength of the periodic electrode structure. The time averaged force in the *z*-direction for a spherical cell is approximately [164]

$$< F_{DEP} >= -64 R^3 V_0^2 \varepsilon_f \,\mathrm{Re}\big[K(\omega)\big] \frac{\cos^2(\frac{\pi d_1}{4d})}{d d_2^2} \exp(-\pi \frac{z}{d})\,, \tag{7}$$

where V_0 is the peak applied voltage to the electrodes, d_1 is the width of the electrodes and d_2 is the spacing between the electrodes; thus d = (d1 + d2) / 2. FEM simulations have confirmed that Morgan's expression is very accurate. It follows from the vertical force balance, $<F_{DEP}> + F_g + F_{drag} = 0$, that the velocity of the cell in the *z*-direction becomes $v_z = (<F_{DEP}> + F_g) / (6\pi\eta R) \cong <F_{DEP}> / (6\pi\eta R)$. The last expression is valid if the effect of gravity is ignored, which we will do for the remainder of this discussion. This is justified because the average transit time through the DEP filter is approximately 0.4 s, while the average sedimentation time in the flow channel is more than 8 s.

The elevation of a cell that is just captured in the DEP filter of length L is the solution to the equation

$$L = \int_{z_0}^{0} \frac{v_x}{v_z} dz = h \int_{u_0}^{0} \frac{v_x}{v_z} du\,, \tag{8}$$

since the integral yields the distance traveled in the x-direction when the cell reaches the bottom of the channel. The integral can be evaluated analytically if gravity is ignored, since both velocities, v_x and v_z, are functions of the elevation. The trajectory of a cell can be calculated from Eq. (8) if the left-hand side is taken as the position x and the upper integration limit as the position z. The result of such a calculation is in agreement with the trajectories Holmes et al. calculated by numerical simulation. [67]

Inserting the expressions for the velocities in Eq. (8) and rearranging, we get a relation between the normalized elevation u_0 and the parameters of the experiment

$$G(u_0) \equiv \int_0^{u_0} u(1-u)\exp(-\pi \frac{h}{d} u)du, \qquad (9)$$

$$G(u_0) = \frac{16}{9}\frac{LWR^2V_0^2}{\pi\eta Q}\varepsilon_f \operatorname{Re}[K(\omega)]\frac{\cos^2(\frac{\pi d_1}{4d})}{dd_2^2}. \qquad (10)$$

The function $G(u_0)$ is easily evaluated, but cannot be inverted analytically. However, we can formally write the capture efficiency ξ as a function of the experimental parameters

$$\xi(u_0) = \xi\left[G^{-1}\left(\frac{16}{9}\frac{LWR^2V_0^2}{\pi\eta Q}\varepsilon_f \operatorname{Re}[K(\omega)]\frac{\cos^2(\frac{\pi d_1}{4d})}{dd_2^2}\right)\right]. \qquad (11)$$

This expression is easily evaluated numerically, and yields the capture efficiency if all cells reaching the bottom of the channel are in fact caught. This might not be the case, since cells at the bottom of the channel are affected by a viscous drag force (and a viscous torque), which could overcome the retaining DEP force, as well as forces due to sticking. The viscous drag force, F_{drag0}, on a spherical cell at the bottom of the channel is to a good approximation given by [165]

$$F_{drag0} = 10.2\pi\eta R v_f(R) = 10.2\pi\eta \frac{R^2}{h}\frac{6Q}{Wh}. \qquad (12)$$

The retaining DEP force can be obtained from a FEM simulation of the DEP structure as $\left|F_{DEP,x}\right| = \beta(R,d_1,d_2,h)\cdot \pi R^3 V_0^2 \varepsilon_f \operatorname{Re}[K(\omega)]$, where the function β equals the maximum value of $(\Delta E^2)_x / V_0^2$ measured at the elevation R. Thus a lower voltage limit for efficient capture can be expected

$$V_{0,\min} \cong \sqrt{\frac{10.2\eta}{\beta(R,d_1,d_2,h)\cdot\varepsilon_f \operatorname{Re}[K(\omega)]}\frac{1}{Rh}\frac{6Q}{Wh}}. \qquad (13)$$

Theoretically expected capture efficiencies at low solution conductivity can now easily be calculated using Eq. (11) combined with the functions defined in Eqs.

(4) and (9); the expected efficiencies can be corrected for viscous drag losses using Eq. (13).

In the experiments reported here the conductivity of the solution is varied from below $\sigma_f < 0.5$ mS/m up to $\sigma_f = 25$ mS/m. The corresponding power dissipated in the liquid varies from below $P < 4$ mW up to $P \approx 200$ mW, respectively, which in turn leads to an estimated temperature increase of the effluent of the DEP filter of $\Delta T < 0.2$ K and $\Delta T \approx 10$ K, respectively. The estimated temperature differences between the bottom and the top of the channel are $\Delta T < 0.1$ K and $\Delta T \approx 5$ K, respectively. It follows that the low conductivity experiments are only slightly affected by Joule heating and the above simplification is justified. For the high conductivity experiments, however, very significant thermal gradient driven flow effects can be expected and the calculated capture efficiencies become inaccurate and too high.

4.4. Results and Discussions

The novel microdevice presented here is a combination of a DEP microchip and two micro flow cytometers (FC's) that can measure quantitatively a large number of cells sorted by DEP. The two FC's are integrated upstream and downstream of the DEP filter for simultaneously counting the number of cell passing through by detection of the forward scattered signals. Quantitative data on the collection efficiencies of the DEP filter can be obtained in real-time by comparing the cell counting rate measured on the two FC's. A standard fluorescent microscope with a slit aperture can be used for detection of fluorescence labelled cells, however, it requires the cell to be labelled with fluorescence and cannot provide forward or large angle scattered signals from the cells. In this study, yeast cells were selected as model cells for testing the DEP operations since they have strong cell walls and show a large difference in permittivity between viable and nonviable cells. In all experiments, the yeast cells were hydrodynamically focused in the channel by two sheath flows from both sides. To enable comparison of the effects of different flow rates, the ratio of sample flow to sheath flow rate was set constant at 1:4.

4.4.1 Capturing Yeast Cells

Preliminary experiments showed that the yeast cell count would decrease gradually during the first 20-30 minutes after which the cell count would stabilize at 15-30% of the original level and would remain stable for 2.5 hour or more. This phenomenon is probably due to a combination of sedimentation and adsorption of yeast cells in the pipeline. To get a stable flow of yeast cells during the experiments it was decided to let the system run for at least 30 minutes before starting any experiment. In future studies, sedimentation effects may be reduced without affecting the osmotic balance and medium permittivity by adding a neutral high density solution, e.g., Ficoll400. [67]

In initial experiments, FITC labeled yeast cells were suspended in MilliQ water to a final concentration of 10^6 cells/mL. The conductivity of the cell solution was less than 0.5 mS/cm and the total flow rate was 1 mL/h, corresponding to a cell solution flow rate of 0.2 mL/h. Before activation of the DEP filter, the cell counting rates at the two micro flow cytometer monitor sites (1^{st} FC and 2^{nd} FC) were virtually identical as seen in Fig. 4.3. The counting rates are significantly lower than expected from the concentration of the cell solution and the flow rate, probably due to sedimentation and adsorption effects as discussed above. To obtain stable cell counting rates in the experiment, the flows were set-up and the system left to stabilize for half an hour before the actual measurements. During this time period the counting rates gradually decreased from the expected rates to the stable rates shown in Fig. 4.3. Then, the DEP filter was switched on for 10 minutes by applying an excitation voltage of 20 V peak-to-peak at 1 MHz. In this period, there was a dramatic reduction in the cell counting rate at the FC downstream of the DEP filter (2^{nd} FC), since most cells were collected on the electrode array by positive DEP. When the DEP filter was switched off again, the cell counting rate at the 2^{nd} FC increased above the level measured at the 1^{st} FC, because cells were released from the DEP filter. Two minutes after switching off the DEP, the cell counting rate at the 2^{nd} FC returned to the value measured at the 1^{st} FC.

The yeast cells were labeled with FITC and the fluorescence light intensity of the yeast cells collected on the DEP filter was measured simultaneously through the microscope (20× objective) as a reference measurement. The results of the fluorescence (FL) measurements were in agreement with the results from the integrated flow cytometers. A baseline fluorescence level was measured before switching on the DEP filter. When starting the DEP filter, the fluorescence level increased linearly with time as cells were captured and accumulated on the filter. After the DEP was switched off, the fluorescence level rapidly decreased and returned to the base level as captured cells were released.

Comparing the cell counting rate monitored on the two FCs reveals that about 90% of the yeast cells were captured on the DEP filter during the DEP operation, see Fig. 4.3. Both the FC and the fluorescence measurement show that about 70% of the captured cells are released almost instantaneously (within 2 min) after switching off the DEP. In comparison with other sorting methods, the DEP filter presented here has the advantage that the sorted cells, captured on the DEP filter, can be released in a very short time to create a highly concentrated sample plug.

A smaller part of the captured cells (~20%) were not released or released only slowly because the adhesive surface forces were larger than the drag force at the edge of the parabolic flow profile. This problem can be solved by coating the DEP filter with a non-fouling coating to prevent cell adhesion. [166] The fluorescence measurements only give indirect, relative information on the collected number of cells. Furthermore, when lots of cells are captured on the DEP array, the captured cells will block excitation and emission light from each other and thus give misleading measurements. In contrast, cells accumulated on the filter do not affect the integrated micro flow cytometers. They yield direct quantitative information on the number of collected and non-collected cells in real-time. This method is therefore suited for measuring the effect of various parameters on the sorting efficiency.

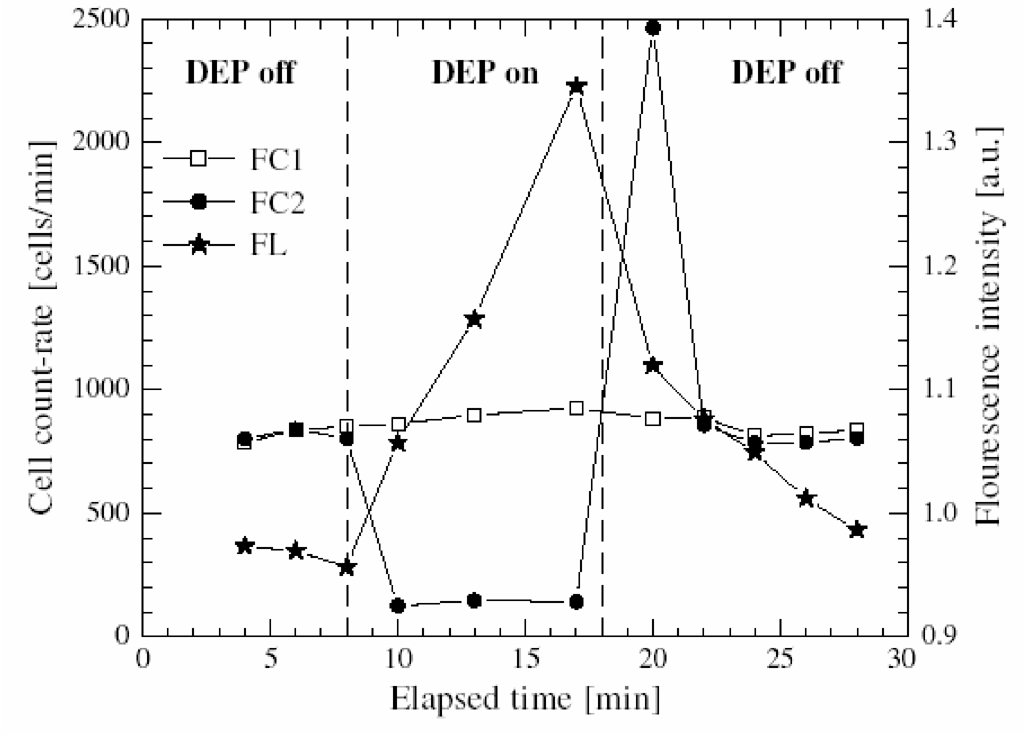

Figure 4.3 *The process of yeast cell capture on the DEP filter monitored by micro flow cytometer counting and fluorescence intensity measurements. The upstream micro flow cytometer (FC1 □) counts all cells entering whereas the downstream micro flow cytometer (FC2 ●) counts all cells leaving the filter. The fluorescent light intensity (FL ★) of the FITC labeled yeast cells collected on the DEP filter was measured through the microscope. The total flow rate was 1 mL/h, the conductivity of the solution was less than 0.5 mS/m, and the concentration of cells in the solution was 10^6 cell/mL (flow rate 0.2 mL/h). The applied voltage to the DEP filter was 20 V peak-to-peak at 1 MHz. The measured cell counting rate on the 1st FC remained almost constant, whereas the cell counting rate on the 2nd FC decreased dramatically when the DEP filter was switched on (at time t = 8 min) because most of the cells were collected at the filter. When the DEP filter*

was switched off again (at time t = 18 min) the cell counting rate on the 2nd FC increased above that of the 1st FC because cells were released from the filter. The capture process monitored by the FL measurements support the flow cytometer measurements. The lines between the experimental data points are for guidance only.

4.4.2 DEP Filter Characterization

To characterize the collection efficiency of the DEP filter, four sets of experiments with varying experimental conditions were performed. The results of these experiments are summarized in Fig. 4.4.

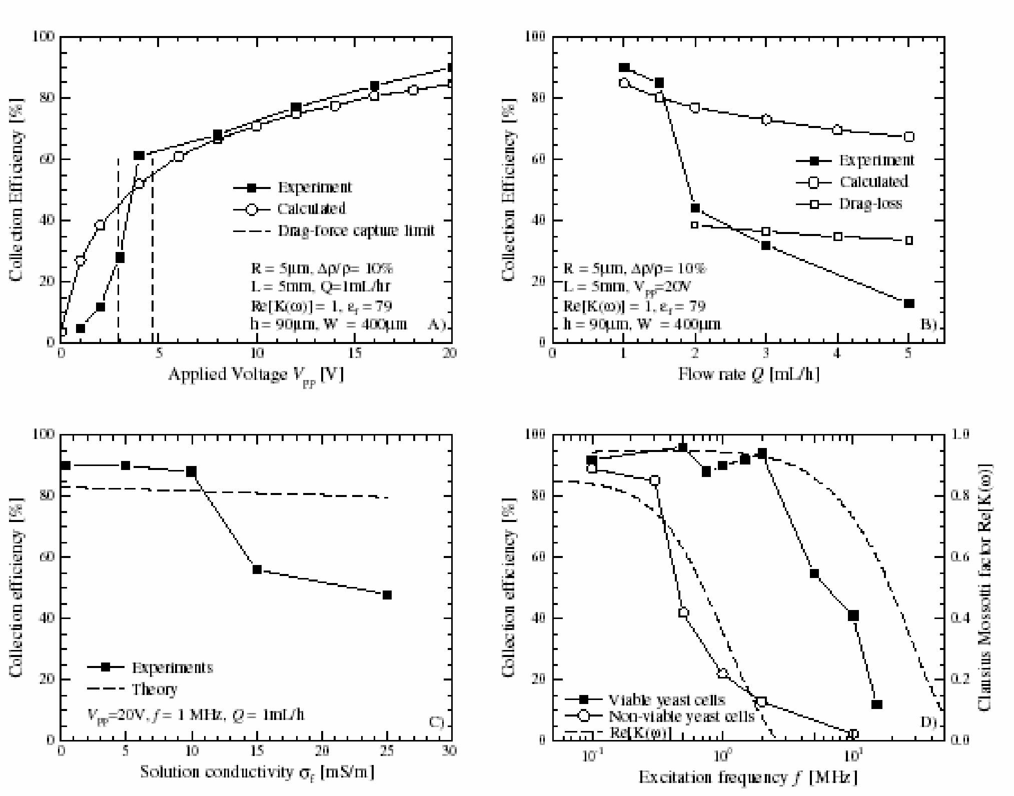

Figure 4.4. The effect of different experimental conditions on the collection efficiency of the DEP filter. The concentration of the yeast cell sample was kept at 10^6 cells/mL, and the other baseline experimental conditions were: total flow rate Q = 1 mL/h, excitation frequency f = 1 MHz, applied peak-to-peak voltage Vpp = 20 V, and solution conductivity σ_f < 0.5 mS/m. ***A)*** *Effect of the peak-to-peak applied voltage Vpp. The experimental results (filled squares) are compared to a simple theoretical model (open circles). Also, the estimated low voltage limits on the collection efficiency due to drag force are shown (dashed lines, see text for more information).* ***B)*** *Effect of the total flow-rate Q. The experimental results (filled squares) are compared to a simple theoretical model (open circles, and*

open squares). ***C)*** *Effect of the solution conductivity σ_f.* ***D)*** *Effect of the excitation frequency f for both viable (filled squares) and non-viable (open circles) yeast cells. The dashed lines are the values of the Clausius-Mossotti factor calculated from a two-shell model of both the viable and the non-viable yeast cells using parameters from Talary. [158] The lines between the experimental data points are for guidance only.*

Fig. 4.4A shows the collection efficiency as a function of the applied peak-to-peak voltage, Vpp, at an excitation frequency of 1 MHz. In the experiment, the conductivity of the liquid solution was $\sigma_f < 0.5$ mS/m, the yeast cell concentration was 10^6 cells/mL, and the total flow rate was 1 mL/h. The experimental data (filled squares) show two distinct regions: above and below Vpp ~ 5 V. Above Vpp ~ 5 V, the collection efficiency increases gradually with increasing applied voltage from ~ 60% to ~ 90% at an applied peak-to-peak voltage of 20 V. In this region, the experimental collection efficiency is in good agreement with the efficiency expected from Eq. (11) (calculated efficiencies: open circles). In the calculation a non-equal electrode width and spacing ($d_1 = 30$ µm, $d_2 = 10$ µm, d = 20 µm) was assumed, but the details of the electrode geometry are not very important as long as the quarter wavelength dimension d = 20 µm is maintained. Furthermore, a cell radius of R = 5 µm, a liquid relative permittivity of $\varepsilon_f = 79$, and the real value of the Clausius-Mossotti factor of Re $[K(\omega)] = 1$ was assumed. To improve accuracy in the low voltage regime, the effect of gravity was included in the calculation, assuming a relative mass density difference to the liquid of $\Delta\rho/\rho = 10\%$.

Below Vpp ~ 5 V, the experimental collection efficiency increases steeply with the applied voltage, but the efficiencies are significantly below the expected efficiency from Eq. (11). The low experimental collection efficiency in this region is believed to be caused by loss of captured cells due to viscous drag forces. The dashed lines show two calculated minimum capture voltages according to Eq. (13), where the retaining force was evaluated from simplified two-dimensional FEM models of the electrode structure. The real experimental structure has castellated electrodes, but two simplified non-castellated models of the electrodes were used in the FEM modeling: one with equal electrode width and spacing (d1 = d2 = d = 20 µm) roughly corresponding to the average of the castellated electrodes, and one with non-equal electrode width and spacing (d1 = 30 µm, d2 = 10 µm, d = 20 µm) corresponding to the real minimum separation of the castellated electrodes. The two different electrode separations in the FEM calculations naturally results in different minimum retaining voltages, $V_{pp\ min} \cong 2.9$ V and $V_{pp\ min} \cong 4.7$ V, respectively. On the castellated electrodes, the minimum retaining voltage is expected to vary with position on the electrode, probably more than covering the full range between the calculated voltage limits, thus explaining a gradual but steep increase of the collection efficiency with applied voltage rather than a full cut off at low voltages.

Yeast cells have been reported to be lysed in less than 100 μs at 20 V pulsed DC bias voltage (10^6 V/m field strength) [167]. However, in our experiments the applied frequencies are much higher, more than 500 kHz. Even at a field strength of 10^6 V/m no sign of cell lysing found during our experiments. Animal cells are known to survive DEP trapping for several days at low applied voltage (2.5 V) and higher frequency (10 MHz) corresponding to a field strength of 50 kV/m. [168] Since the conductivity of the yeast cell suspension is always less than 0.5 mS/m, the lysing caused by the thermal effect can also be neglected.

Fig. 4.4B shows the collection efficiency as a function of the flow-rate Q, at an applied peak-to-peak voltage of Vpp = 20 V and an excitation frequency of 1 MHz. In the experiment the conductivity of the liquid solution was $\sigma_f < 0.5$ mS/m, and the yeast cell concentration was 10^6 cells/mL. Again, the experimental results (filled squares) fall into two distinct regions: below and above Q = 2 mL/h. Below 2 mL/h the high collection efficiency (~90%) decreases gradually with increasing flow rate in agreement with the calculated efficiency from Eq. (11), represented by open circles. Above and at 2 mL/h the collection efficiency is much lower (less than 50%) and a quite dramatic decrease is seen between 1.5 and 2 mL/h. A possible explanation is loss of captured cells due to the viscous drag force. To exemplify this point, the open squares represent the calculated collection efficiency from Eq. (11) if only half of the electrode area is effective. This is a possible scenario, since the electrodes are castellated, and therefore the retaining force varies dramatically with position on the electrode. The experimental collection efficiency decreases at a higher rate with increasing flow rate, which is in qualitative agreement with Eq. (13). In Eq. (13) the minimum retaining voltage increases with the flow-rate due to the increasing viscous drag force, thus rendering less and less of the electrode area effective for cell capture. At high flow rates, only the outer corners of the castellated electrodes may be effective.

Fig. 4.4C shows the collection efficiency as a function of the conductivity σ_f of the solution. The conductivity of the solution was adjusted by adding 0.01M KCl to the solution in both sheat and sample flows. Below $\sigma_f = 10$ mS/m the collection efficiency decreases very slowly with increasing conductivity, whereas the decrease above $\sigma_f = 10$ mS/m is quite dramatic. The decreasing collection efficiency with increasing conductivity is in theory caused by the effect of conductivity on the Clausius-Mossotti factor, which at 1 MHz, to a fair approximation, depends only on the conductivities of the cell interior and the solution, $\mathrm{Re}\,[K(\omega)] \sim (\sigma_c - \sigma_f)/(\sigma_c + 2\sigma_f)$. If the conductivity of the cell interior is assumed independent of the solution conductivity the effect of conductivity on the

collection efficiency should be small, approximately as seen below σ_f = 10 mS/m, since the conductivity of the cell interior is expected to be much larger than the solution conductivity (0.1 S/m < σ_c < 1.2 S/m). [157-159] The discrepancy at higher conductivities is most likely due to thermal effects, since the power dissipated in the DEP filter increases linearly with the conductivity, to a first approximation. The power is mostly dissipated near the electrodes giving rise to substantial thermal gradients, which in turn will cause severe flow disturbances that will interfere with the DEP filter and reduce the collection efficiency. At the highest conductivity used in the experiments, σ_f = 25 mS/m, on the order of 200 mW is dissipated in the DEP filter, whereas the base-line experimental conditions dissipate only ~ 4 mW. Experiments with conductivities above 25 mS/m were destructive since the Ti adhesion layer for the electrodes was
electro-chemically etched within a few minutes. The electro-chemical reaction also generates hydrogen, thus filling the channel with bubbles. This problem might be relieved by replacing the Ti/Au electrodes by metal-silicide electrodes. [169] Low conductivity media have been used in the vast majority of dielectrophoretic cell sorting experiments reported in the literature. [72-76] Many cells (e.g., human or animal cells) require media with physiological osmotic pressure to avoid cell lysis. To fulfill this requirement a sugar solution with physiological osmotic pressure and low conductivity (e.g., 9% w/w) can be applied for sorting such cells. This approach has, e.g., been used for dielectrophoretic-based sorting of malaria infected cells [72] or cancer cells [73-75] from normal cells and the equations and model presented here may be used to optimize such processes. However, our results also indicate that this simplified model breaks down when the conductivity is increased to levels where thermal effects become significant and care should therefore be taken when applying the model.

Fig. 4.4D shows the collection efficiency as a function of the excitation frequency for viable (filled squares) and non-viable (open circles) yeast cells. As expected, the collection efficiency is high and approximately constant at low frequencies and decreases rapidly with frequency above a certain corner frequency, which depends on the viability of the cells. As a result, the DEP filter can selectively capture the viable cells while the non-viable cells pass the filter relatively unaffected if a sufficiently high excitation frequency (*f* ~ 1 - 2 MHz) is chosen. This is due to the significant decrease in cell conductivity for non viable cells due to perforated cell membranes. [158] In Fig. 4.4D we show calculated values of the Clausius-Mossotti factor for both viable and non-viable yeast cells evaluated from a two shell model of the cells using the parameters given by Talary. [158] The corner frequencies in the collection experiments are expected to be significantly higher than the corner frequencies of the Clausius-Mossotti factor due to the nonlinearity of the capture process; obviously, the experimental data are not in agreement with this expectation. This is probably again due to loss of captured cells caused by viscous drag forces. Since the retaining force is directly proportional to the Clausius-Mossotti factor the decrease in this factor at high frequencies can lead to a quite dramatic loss of captured cells. This is a nice demonstration of how useful the integrated micro flow cytometers are for monitoring the DEP filter operation, and that experimental validation of DEP models is always necessary. The biological variability of the dielectric parameters of cells also imposes a need to monitor and experimentally validate the DEP operation.

Experiments at excitation frequencies below 100 kHz proved destructive to the electrodes due to electro-chemical etching of the Ti adhesion layer. Again metal-silicide electrodes might relieve the problem. [169]

4.4.3 DEP Filter Capture Capacity

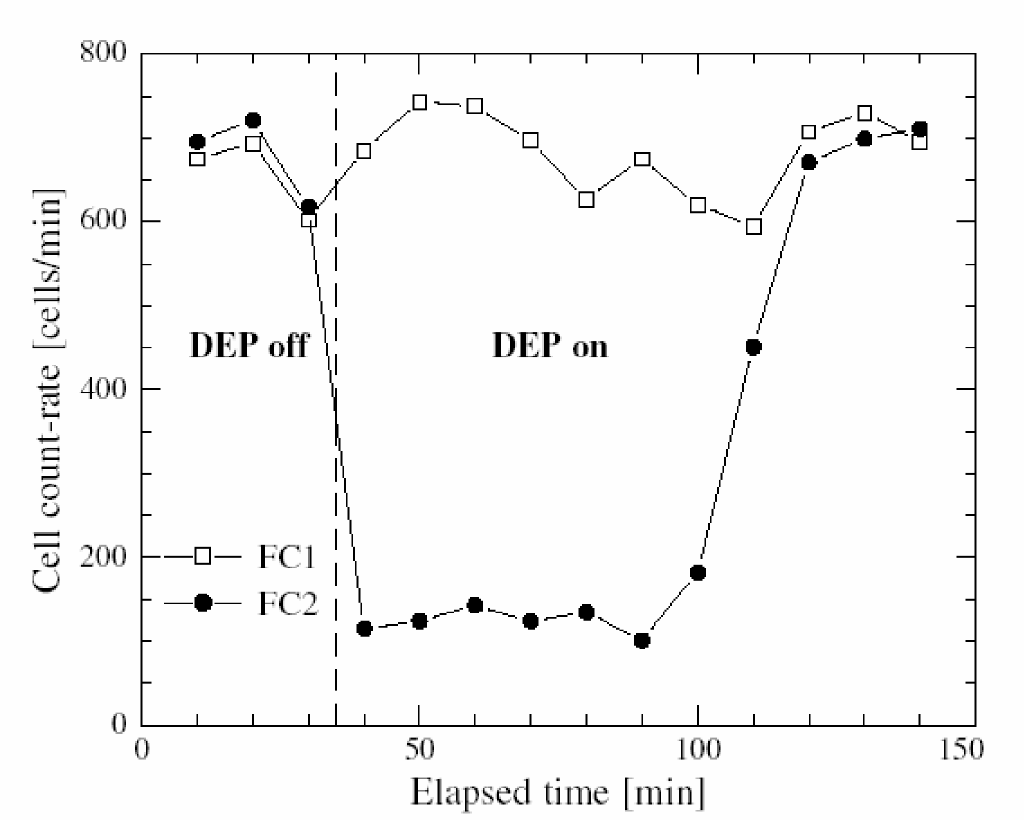

Figure 4.5 Monitoring yeast cell capture on the DEP filter at 1 MHz with 20 V applied peak-to-peak voltage by micro flow cytometer counting. The total flow rate was 1.5 mL/h and the sample concentration was 10^6 cells/mL (flow rate 0.3 mL/h). The upstream micro flow cytometer (FC1□) counts all cells entering

whereas the downstream micro flow cytometer (FC2 ●) counts all cells leaving the filter. The DEP filter was turned on at time t = 35 min. At time t ≅ 125 min the capacity limit (estimated 100000 cells/mm2) of the filter is reached and break-through is observed. The lines between the experimental data points are for guidance only.

Using the two micro flow cytometers integrated up- and down-stream of the DEP filter it is straightforward to estimate the capacity of the DEP filter from a break-through measurements as shown in Fig. 4.5. In this experiment, the total flow rate was 1.5 mL/h, where 0.3 mL/h of this flow stream was a cell solution with a nominal cell concentration of 10^6 cells/mL. The flow was left to stabilize and at time t = 35 min the DEP filter was turned on by applying 20 V peak-to-peak voltage at 1 MHz to the DEP electrodes. At time t ~ 125 min the capacity limit of the filter was reached and the filter saturated with cells as seen when comparing the count rates of the 1st FC (open squares) to the count rates of the 2nd FC (full circles). A constant high collection efficiency (~ 85%) was observed until t ≅ 100 min, but as the filter starts to saturate, the efficiency gradually decreases because the cover of captured cells reduce the capture force on cells. From the measurements, the DEP filter capacity is estimated to be ~ 100000 cells/mm^2, since a total of ~ 40000 cells (the integrated count rate difference) were captured on a fifth of the total area of the filter (0.4 × 5 mm^2), since the sheathing flows occupy the rest of the DEP filter area. It follows that several layers of captured cells must cover the capture electrodes in the saturated filter, since the estimated capacity corresponds to an average occupied filter area of only 10 μm^2 per cell.

4.4.4 Viable and Nonviable Cell Sorting Monitored in Real-Time

The differences in capture efficiency of the DEP filter for viable and non-viable yeast cells as demonstrated in Fig. 4.4D, where the collection efficiency for viable cells was 8-9 fold higher than for nonviable cells at 1-2 MHz, facilitates sorting of these cells on the DEP filter. The integrated flow cytometers allow real-time monitoring of this process. Fig. 4.6 shows the results from an experiment sorting a 1:1 mixture of viable and nonviable yeast cells, with a cell concentration of 10^6 cells/mL at 2 MHz with 20 V peak-to-peak applied voltage, and 1 mL/h total flow rate. The nonviable cells were FITC labelled, by conjugating the cell membrane proteins with FITC followed by a heat treatment of the cell solution to render the cells nonviable. After the heat treatment, the thick cell membranes were still intact, and the cells could be distinguished by FITC fluorescence measurements. The fluorescence signals were measured through a slit aperture (0.2 mm wide) located below the 2nd FC. The signals were collected by the inverted microscope fitted with a band pass filter (589/22 nm), a 40× objective, and a PMT. The count rate from the upstream micro flow cytometer (FC1, symbol □) remained almost constant when the DEP filter was switched on at time t = 8 min, whereas the count rate on the downstream micro flow cytometer (FC2, symbol ●) dropped from essentially the same value as measured on FC1 to approximately half of the initial value when the filter was turned on, indicating that approximately half of the cells were captured on the filter. The fluorescence count rate (FL, symbol ★) was approximately equal to half of the count rate of the upstream flow cytometer, and remained almost unaffected by turning on the DEP filter. Thus, we conclude that most of the captured cells on the DEP filter were viable non-fluorescent cells, and the nonviable FITC labeled cells were almost unaffected by the DEP filter. When the DEP filter was turned off again at time t = 18 min, the count rate on the downstream flow cytometer FC2 increased abruptly since the captured cells were released from the DEP filter. The count rate on FC2 returned to essentially the same value as measured on FC1 after some time. From a comparison of the three measured count rates we conclude that more than 90% of the viable and less than 10% of the nonviable cells were caught on the DEP filter. It follows that the sorting efficiency of the DEP filter described here is comparable to the sorting efficiency of the best of other microchip sorting devices.[48, 69, 72-75]

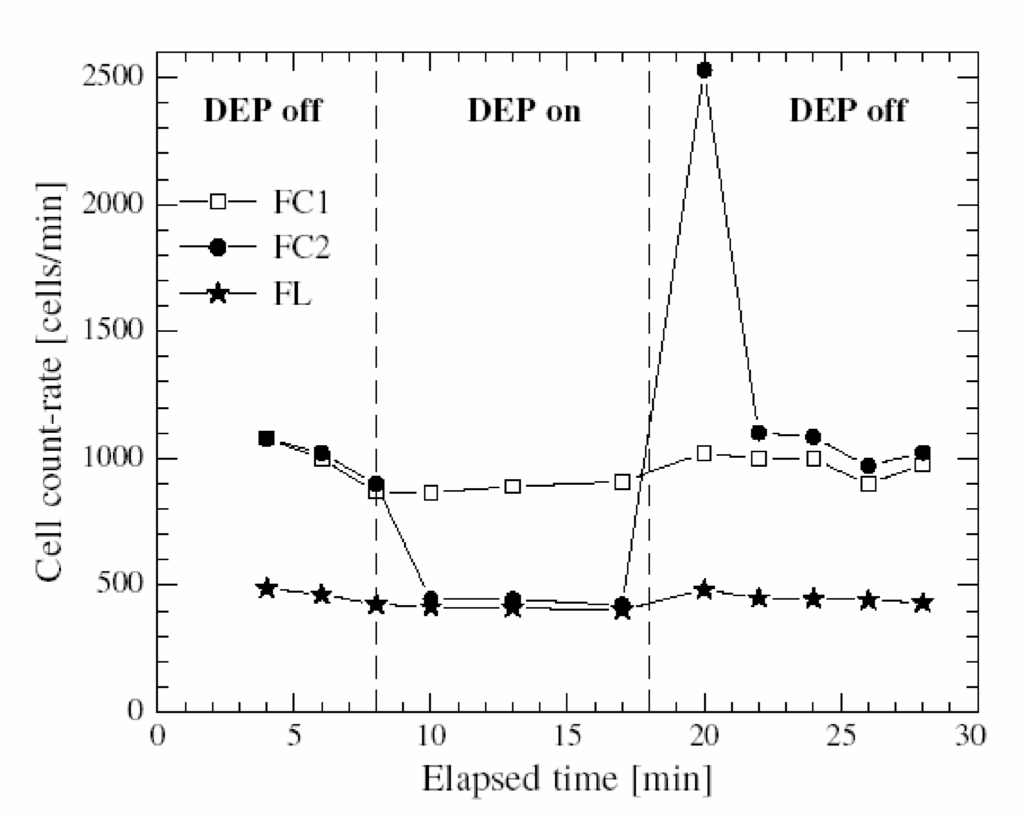

__Figure 4.6__ Sorting of a 1:1 mixture of viable and non-viable (FITC labeled) yeast cells at 2 MHz with 20 V applied peak-to-peak voltage, monitored by micro flow

cytometer cell counting and counting of fluorescent labeled cells. The total flow rate was 1 mL/h and the concentration of the cell solution 10^{6} *cells/mL (flow rate 0.2 mL/h). The upstream micro flow cytometer (FC1 ☐) counts all cells entering whereas the downstream micro flow cytometer (FC2 ●) counts all cells leaving the filter. The fluorescent count rates (FL ★) were obtained through a 0.2 mm slit aperture positioned below the second flow cytometer. The DEP filter was turned on from time t = 8 min to t = 18 min. From the counting rates we conclude that the viable cells were almost completely captured, while most of the non-viable yeast cells passed through the filter. The lines between the experimental data points are for guidance only.*

4.5 Conclusions

We have described the design and fabrication of a novel microdevice with a DEP filter and two optical micro flow cytometers monolithically integrated. Considering the high functionality obtained, the fabrication is surprisingly simple, since only two photolithographic steps are required. With minor modifications, the fabrication platform will allow even more functionality to be integrated, e.g., PCR reactors. [120, 169]

We have demonstrated the use of the integrated flow cytometers for on-line evaluation of the capture efficiency of the DEP filter with respect to applied voltage level, excitation frequency, flow rate, and solution conductivity using yeast cells as a model. We found the measured results in reasonable agreement with our theoretical predictions. Furthermore, we applied the integrated flow cytometers for real-time monitoring of cell sorting on the DEP filter. To our knowledge it was the first time this was done in an integrated system, which integrated two flow cytometers to achieve a functionality that cannot be obtained with conventional instruments. The flow cytometer measurements were supplemented by fluorescence measurements on FITC labelled cells and a good agreement between the two independent measurement methods was observed.

The simple fabrication process, the demonstrated functionality, and the rather straightforward integration of even more functionality hold promise for low cost fabrication of disposable multi functional integrated microsystems that can compete with, or even outperform, conventional instruments both on technical performance and cost.

Acknowledgments

The research was supported by the Danish Technical Research Council (STVF) (Grant no. 26-02-0307).

Supplementary Information

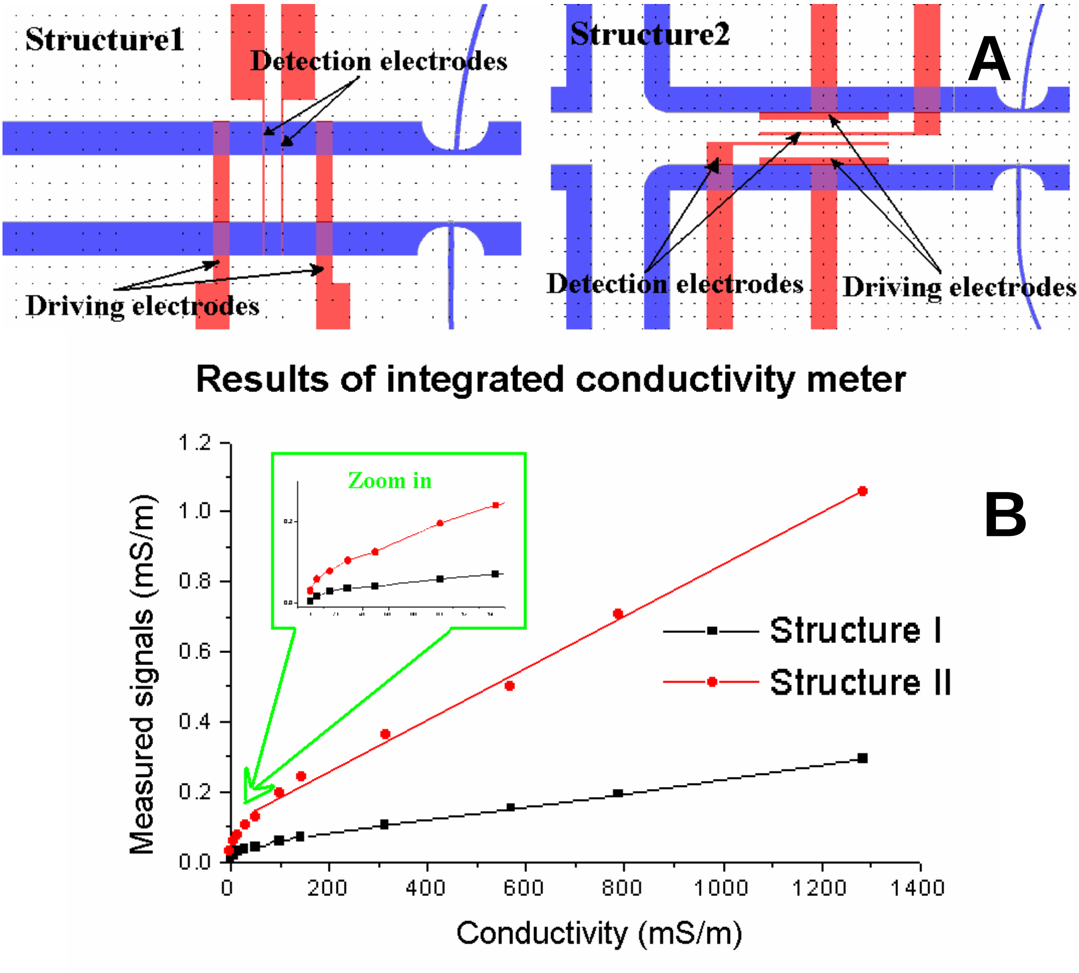

***Supplementary Figure 1. A:** Schematics of two integrated conductivity meter structures. **B:** Results of the conductivities measured by the integrated conductivity meter compared with known conductivities. The zoom-in area shows the nonlinear profiles for the low conductivity measurements.*

Since the DEP operations are very sensitive to the conductivity of the medium, we also integrated two kinds of integrated four-pole conductivity meter inside the channel (Supplementary Fig. 1A) and tested them (Supplementary Fig. 1B). For the four-pole conductivity meter, the two outside electrodes are the driving electrodes, and the two inside electrodes act as the detection electrodes. During the test, the microfluidic channel was filled with different conductivities concentration KCl solutions (0.1 – 1285 mS/m). A 200mV, 94Hz AC voltage was applied for the conductivities' measurements by a CDM230 conductivity meter (Radiometer Analytical SAS, France). Here the cell constant was kept same as the standard cell constant used in the conductivity meter. The structure 2 is designed parallel to the channel, then the length of electrodes can be set longer than the structure 1. Thus the effective area of the structure 2 is larger than the structure 1, and the conductance of the structure 2 is also larger than the structure 1. From the test, under the same cell constant set the structure 2 has higher sensitivity than the structure 1. Both structures show quite good linearity for the measurements above 10mS/m. However in the low conductivity environments, both of them show the nonlinear dumping results. Due to the impendence (~1MΩ) between the double layer capacitances are close to the same order magnitude of the impendence of the Pyrex substrate, part of the currents are leaked through the substrate and can not measured by the integrated conductivity meters.

Chapter 5: Towards a portable microchip system with integrated thermal control and polymer waveguides for real-time PCR Real-time[†]

Z. Wang[1], A. Sekulovic[1,2], J.P. Kutter[1], D.D. Bang[3] and A. Wolff[1,*]

[1]*MIC – Department of Micro and Nanotechnology, Technical University of Denmark E-mail: aw@mic.dtu.dk; Fax: +45 4588 7762; Tel: +45 4525 6305*
[2]*Department of Biotechnology, Technical University of Delft*
[3]*Department of Poultry, Fish and Fur Animals, Danish Institute for Food and Veterinary Research*

A novel real-time PCR microchip platform with integrated thermal system and polymer waveguides has been developed. The integrated polymer optical system for real-time monitoring of PCR was fabricated in the same SU-8 layer as the PCR chamber, without additional masking steps. Two suitable DNA binding dyes, SYTOX Orange and TO-PRO-3, were selected and tested for the real-time PCR processes. As a model, *cad*F gene of *Campylobacter jejuni* has been amplified on the microchip. Using the integrated optical system of the real-time PCR microchip, the measured C_T (cycle threshold) values of the real-time PCR performed with a dilution series of *Campylobacter jejuni* DNA template (2 to 200 pg/µL) could be quantitatively detected and compared with a conventional post - PCR analysis (DNA gel electrophoresis). The presented approach provided reliable real-time quantitative information of the PCR amplification of the targeted gene. With the integrated optical system, the reaction dynamics at any location inside the micro reaction chamber can easily be monitored.

5.1 Introduction

During the last decade, micro Total Analysis System (µTAS) devices have had a remarkable impact on biochemical, chemical, and pharmaceutical research activities, because of their many potential advantages, such as reduced cost, portability, and low reagent consumption. [3] To realize such µTAS devices, the integration of different detectors to monitor various parameters within the system is a crucial step. Recently, we have demonstrated the application of an integrated polymer optical system for cell detection in a micro flow cytometer. [152] The integrated optical system provided more integration feasibility, higher capacity, and more precise alignment for various microsystems in comparison to the bulk

---

[†] Submitted to Electrophoresis in Jun. 2006

optical system. In this paper, we apply integrated optics for real-time monitoring of Polymerase Chain Reaction (PCR).

Polymerase Chain Reaction (PCR) is an enzyme-catalyzed nucleotide amplification technique, routinely used in many different fields for genetic identification. Although PCR is a robust and predictable method, quantification can be difficult because the final amplified product concentration often has large variations caused by minor disturbances, e.g. reaction components, thermal cycling fluctuation, or primer misalignment. [106] A solution to this problem is to use real-time PCR. In real-time PCR, the product formation is measured during the reaction by using different fluorescent DNA binding dyes or different types of fluorescently labeled probes such as Hybridization probes [109], Hydrolysis probes [110, 111], and Hairpin probes [112-116], which bind specifically to DNA targets. The DNA binding dye most often used in real-time PCR is SYBR green I. [107, 108] This dye has very low fluorescence in solution, but its fluorescence increases 1000-fold when it binds to double-stranded DNA (dsDNA) and therefore acts as a non-specific fluorescent reporter of the dsDNA concentrations. A PCR amplification curve can be established by measuring and plotting the fluorescence intensities after each PCR cycle. The cycle threshold value (C_T) is the cycle number at which the fluorescence intensity is higher than the detection baseline level. This parameter provides more accurate and real-time quantitative information on the PCR amplification process. [105]

PCR has also been realized on microchips. To date, three different types of PCR microchips have been developed, featuring either a chamber [83-96, 102], a continuous flow [97-100], or a droplet oscillation design [101]. Until now, only few real-time PCR microsystems have been reported. [117-119] Recently, Gulliksen *et al*. (2004) described a novel real-time PCR microchip. However, this real-time PCR microchip required an external optical system to detect the fluorescent probes. [118, 119]

We have applied PCR microchips for the detection of *Campylobacter*. *Campylobacter jejuni* is the most common food-borne bacterial pathogen that causes gastroenteritis for humans. [170] Several groups have developed different conventional real-time PCR procedures for rapid detection of *Campylobacter*. [171-173] Previously, we reported on a PCR microchip with integrated thermal system for fast thermocycling [120] and this PCR microchip had been applied to detect *Campylobacter jejuni*. In this study, we present a novel real-time PCR microchip with integrated heater, thermometer and polymeric optical elements to detect the *cad*F gene of *Campylobacter jejuni* using DNA binding dyes.

5.2 Experimental section

5.2.1 Modeling of the heater array

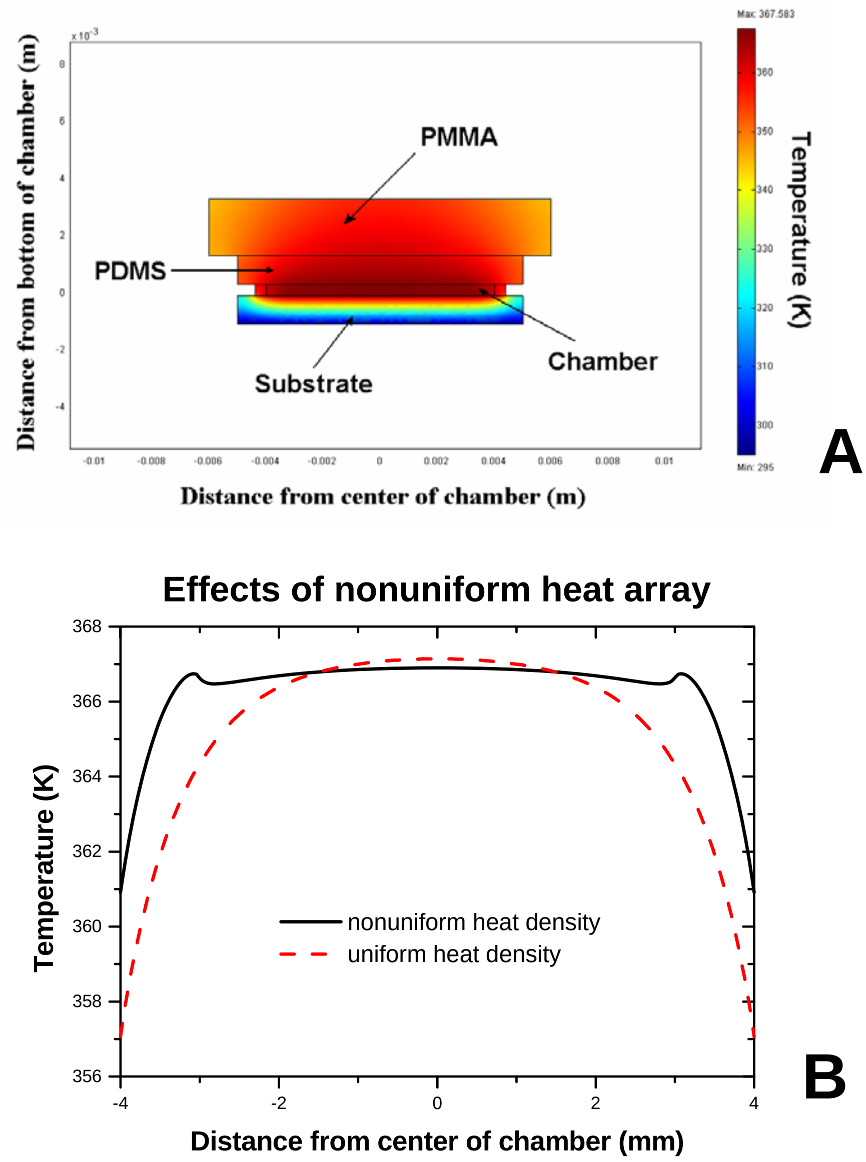

Figure 5.1. A: *The simulated thermal profile using a 2D heat transfer simulation model in FEMLAB3.1.* ***B:*** *Comparison of the temperature profiles inside the reaction chamber for two different heat array designs.*

Based on a previously integrated thermal system design [120], the Pt heater array was remodeled and redesigned. A 2D heat transport model has been established in FEMLAB 3.1 (Fig. 5.1A). The heat is generated by the integrated Pt heater array.

The chip is passively cooled by heat conduction through the substrate to an aluminum heat sink and by natural convection from the lid. Therefore, the boardary condition of the model is set as: The temperature at the substrate bottom is fixed as 25 °C, the rest edges are natural convected with ambient. All the real dimensions of the chip and the packaging are applied in the model. The material properties of the materials in the model are listed in the Table 5.1.

	Borosilicate	water	SU-8	PDMS	PMMA
Thermal conductivity λ ($Wm^{-1}K^{-1}$)	1.1	0.6	0.2	0.15	0.19
Density ρ (Kgm^{-3})	2200	1000	1200	970	1200
Specific heat capacity c ($JKg^{-1}K^{-1}$)	700	4200	1500	1460	1460
Layer thickness (mm)	1.0	0.4	0.4	1.0	2.0

There is extra heat loss at the edges of the chamber. To avoid the detrimental effect of a "cold wall", the integrated Pt heater array was designed to generate a 1.1 times higher heat density at the edges by reducing either the heater width or the distance between the heaters, and by extending the heaters outside of the chamber. The simulation results (Fig. 5.1B) show a much better temperature profile for the non-uniform heat source than for the uniform one. The homogeneous temperature area (within ± 0.5 °C variation at 94 °C) inside the chamber has been expanded three times (from 16 mm^2 to 49 mm^2) in comparison to the previous design. [120]

5.2.2 Chip design, fabrication and packaging

The fabrication of the real-time PCR microchip (18 mm × 18 mm) is a three-mask process as described previously. [120] Firstly, the electrodes (100 Å Ti, 200 nm Pt) for the integrated heater array and thermometer were deposited on a 1000 µm Pyrex substrate (Schott Corporation, Germany) by e-beam evaporation and defined in a standard lift-off process. Secondly, on top of the metal layer, a 5 µm SU-8 (XP2005, MicroChem, USA) protection layer was fabricated to serve as the chamber floor. Finally, the 8 mm × 8 mm reaction chamber (25 µl) and optical systems were defined by a standard photolithography in a 400 µm thick SU-8 (XP2075, MicroChem, USA) layer (refractive index n = 1.59). The chip structure is shown in Fig. 5.2.

The reaction chamber was hermetically sealed by a 1 mm thick PDMS lid with a refractive index n = 1.4, which also provides top cladding for the waveguides. The substrate (n = 1.46) provides the buffer layer of the waveguides, while the PCR mix (n = 1.32) provides the vertical side claddings of the 200 µm wide waveguides. The SU-8 layer thickness was adjusted to readily accommodate 400 μm outer diameter optical fibers (FVP300330370, Polymicro technologies, L.L.C., USA) in the fiber couplers. The chip was finally packaged on a custom-built aluminum heatsink for the passive cooling purpose. A thin layer of thermal conductivity paste (Dow Corning GMBH, USA) was administered to the backside of the chip to enhance thermal conduction.

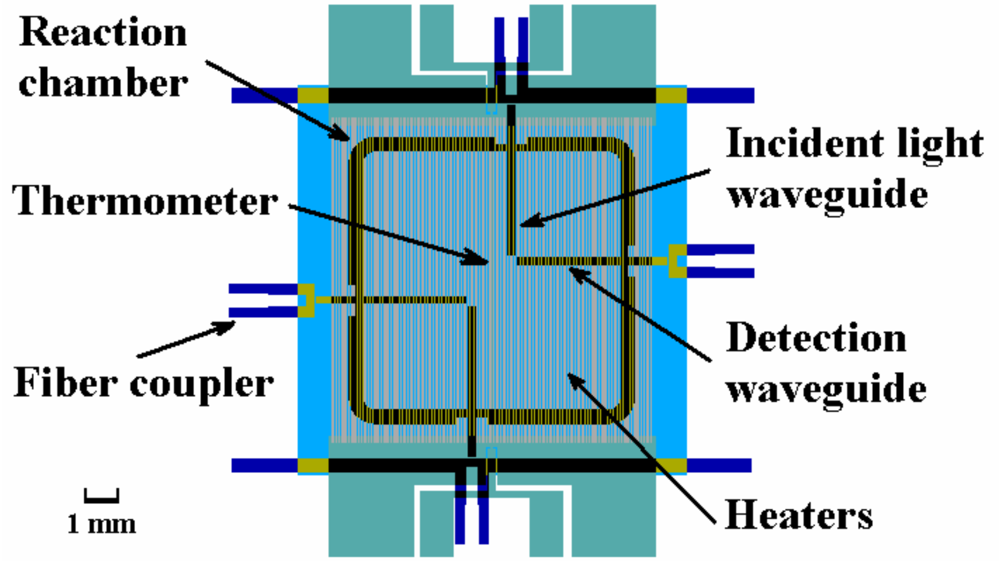

Figure 5.2. *The layout sketch of the chip with integrated waveguides and thermal system. The thermal system consisted of an array of 104 Pt heaters and a thermometer integrated beneath a 5 μm thick SU-8 protection layer. The dimension of the reaction chamber is 8 mm × 8 mm × 0.4 mm, to form a 25 μl PCR reactor. On the microchip, 4 waveguides are placed inside the chamber for fluorescence detection. All the integrated optical elements (waveguides, couplers) are defined in the same SU-8 layer as the reaction chamber in one photolithography step.*

The electrodes on the chip were connected to the analog circuitry by two different types of probe pins. Thin (0.37 mm diameter) probe pins (SS-30-J-1.3-G, Interconnect devices, Inc., USA) were used to connect the four thin pads of the 4-point thermometer sensor. Whereas thick (1.98 mm diameter) probe pins (S-4-C-5-G, Interconnect devices, Inc., USA) were used to connect the four wide pads for the heater array for preventing current overloading at the connecting areas. A Lab-view PID temperature-controlling program was used to control the power of the integrated thermal system using a 15W custom-built power supply.

5.2.3 Primers and real-time PCR conditions

Bacterial chromosomal DNA was isolated from a *Campylobacter* culture on blood agar substrate incubated for 24 hours under micro-aerobic conditions (6% O_2, 6% CO_2, 4% H_2, and 84% N_2) at 42°C as previously described. [120] The DNA was eluted in 100 µl of pre-heated (65°C) sterile water. DNA concentrations were determined by optical density (OD) measurements at 260 nm [174] using a spectrophotometer (Ultrospec 2000, Pharmacia Biotech, Cambridge, UK) and the DNA preparations were stored at – 20 °C until use. For the testing of the real-time PCR on the PCR microchip, a *Campylobacter jejuni* DNA template concentration series (2, 10, 20, 100, and 200 pg/µl) was prepared.

Two primers, namely F2B with sequences 5'-TGG AGG GTA ATT TAG ATA TG-3' and R1B with sequences 5'-CTA ATA CCT AAA GTT GAA AC-3' (synthesized by TAG Copenhagen, Inc., Denmark) were used to amplify a 398 bp amplicon of the *Campylobacter jejuni cad*F gene. PCR mixtures (50 µl) contained 0.1 µM (each) dATP, dCTP, dGTP and dTTP (TAG Copenhagen, Inc., Denmark), 2 µM $MgCl_2$ (Roche Diagnostics Corporation, USA), 12.5 nM of each primer (DNA Technology, Aarhus, Denmark), ×1 PCR buffer (Roche Diagnostics Corporation, USA) and 25 U/ml of *Taq* DNA polymerase (Sigma, USA), 1 µg/µL non-acetylated bovine serum albumin (BSA) (Sigma, USA) and DNA template. Two different DNA binding dyes, SYTOX Orange (ex 547nm/em 570nm) and TO-PRO-3 (ex 642nm/em 661nm) (Molecular probes, Inc., USA), were added into the PCR mix (200 nM each) for the real-time PCR detections.

Of the 50 µl prepared PCR master mix, 25 µl were used for the real-time PCR on the PCR microchip while the rest was used for a conventional real-time PCR using a commercial real-time PCR machine (Chromo4®, MJ Research, Inc., USA) as control. The PCR conditions were: one cycle at 95 °C for 2 minutes, followed by 40 cycles of 94 °C for 15 seconds, 50 °C for 15 seconds and 72 °C for 15 seconds, and ending with a 2 minute elongation stage at 72 °C.

5.2.4 Optical system

For the real-time PCR measurements on chip, a 60 mW diode pumped solid-state green laser (535 nm) (DPSSL-60, Viasho, P.R. China) and a 5 mW He-Ne laser (633 nm) (25-LHR-151-230, Melles Griot, USA) were used to provide two different excitation wavelengths. Two different types of photomultiplier tubes (PMT) from Hamamatsu, Japan, a H5784 (for the 535 nm excitation light) and a H5784-01 (for the 633 nm excitation light), were used to measure the fluorescent signals at the two different wavelengths. A 5 mm × 5 mm × 2 mm FGL550S long pass filter (cut from a 50 mm × 50 mm filter slide obtained from Thorlabs Inc., USA) was placed in front of the aperture of the PMT SMA adapter (E5776-51, Hamamatsu, Japan) for filtering of 535 nm excitation light, while a 5 mm × 5 mm

× 3 mm LP645 long pass filter (cut from a 50 mm × 50 mm filter slide obtained from Melles Griot, USA) was placed in front of the aperture of another PMT SMA adapter for filtering of 633 nm excitation light. To avoid photo bleaching of the fluorescence dyes, a custom-modified chopping blade with a 3% duty cycle was placed in front of the lasers. A SR540 chopper controller (Stanford Research Systems, Inc., USA) was used to manipulate the chopper.

5.3 Results and discussions

In this paper, a real-time PCR microchip with an integrated thermal system and a polymer-based optical detection system is presented. The fluorescence from the real-time PCR is measured using a pair of waveguides. The waveguides, one for introducing excitation light, and the other for receiving the fluorescent signals, are placed perpendicular to each other to avoid collection of too much excitation light. Together they define a detection point (Fig. 5.2). The distance between two waveguide ends is kept short (200 μm), since the measured fluorescent signal intensity is inversely proportional to the detection distance squared. Two such pairs of waveguides were integrated at different positions inside the reaction chamber to locally monitor the fluorescence intensity. The design with two pairs of integrated waveguides provides the ability to monitor two different wavelengths in *multiplex* real-time PCR applications and can easily be modified to detect fluorescent signals at any desired location inside the PCR reaction chamber.

All parts of the integrated optical system in the real time PCR microchip are made from SU-8, and the selection of suitable DNA binding dyes according to the optical properties of SU-8 is therefore a crucial step. SYBR Green I is the most common DNA binding dye used in real-time PCR [107, 108, 175], and it is excited by a blue light source (e.g. an Ar-ion laser with a wavelength of 488nm). However, SYBR Green I is not a suitable dye for the real time PCR microchip described here since SU-8 has very high light absorption and high fluorescence background at low wavelengths (less than 500 nm). [24, 153] To avoid this problem, two other DNA binding dyes, SYTOX Orange (ex 547nm/em 570nm) and TO-PRO-3 (ex 642nm/em 661nm) with longer excitation and emission wavelengths were selected for testing the real-time PCR microchip. Tests in conventional real-time PCR showed that the two dyes were thermally stable and showed very low PCR inhibition (unpublished data).

In initial experiments, the melting curves were determined by mixing the DNA binding dyes with the DNA fragment from a PCR reaction. At the melting point of the DNA fragment, where the double strand DNA melts to single strand DNA, the fluorescent signals decrease significantly, since the DNA binding dyes are only fluorescent when bound to double strand DNA. Using the real-time PCR microchip with a temperature ramp (from 35 °C to 95 °C with 2 °C/min), the melting curve of the DNA fragment could be determined. The result of such an experiment with SYTOX Orange labeled DNA is shown in Fig. 5.3. The melting point was determined by differentiating the registered melting curve, and the melting point (83 °C) measured on the real-time PCR chip is the same as measured on the conventional Chromo4® real-time PCR thermal cycler. The presented approach shows good sensitivity for the fluorescence measurements during the thermal process.

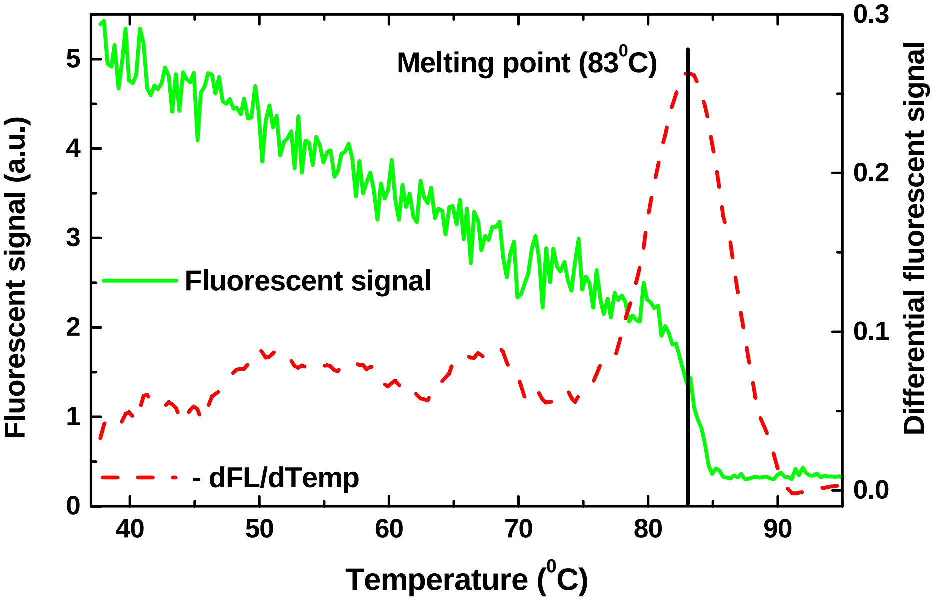

Figure 5.3. *Melting curve measurement of the 398 bp amplicon of Campylobacter jejuni cadF gene using SYTOX Orange. A temperature program from 35 ℃ to 95 ℃ with a ramp of 2 ℃/min was used. The gradual decrease in signal in the range from 35 ℃ to 80 ℃ is due to the temperature-dependence of the fluorescence. The following steep decrease depicts the melting process of the PCR product. The melting point was determined by differentiating the melting curve (dFL/dTemp), and the melting point was found to be 83 ℃.*

DNA binding dye will bind to the dsDNA of any PCR product. Therefore, specific fluorescence probes (labeled ss-DNA oligonucleotides) are normally required to distinguish the different products in a multiplex real-time PCR. However, the costs of the fluorescent DNA binding dyes are much lower than those of the specific fluorescent probes, and in some cases the probes require the use of an expensive specific enzyme. Furthermore, the requirements for optimization of the PCR protocol are less stringent when using the DNA binding dyes. In addition, by measuring the melting curve after the real-time PCR, the PCR product can be examined *in situ* without further post-PCR analysis (e.g. DNA gel electrophoresis), while it is not possible when using fluorescence probes. The DNA binding dyes were therefore selected for preliminary testing of the real-time PCR microchip.

During the real-time PCR experiments, two different colored fluorescent DNA binding dyes (SYTOX Orange and TO-PRO-3) were added into the PCR mixture to monitor the reactions on chip. A typical data profile of the real-time PCR labeled with TO-PRO-3 is shown in Fig. 5.4. The three stages of a PCR cycle (15 seconds denaturation at 94 °C, 15 seconds annealing at 50 °C and 15 seconds elongation at 72 °C) can clearly be distinguished.

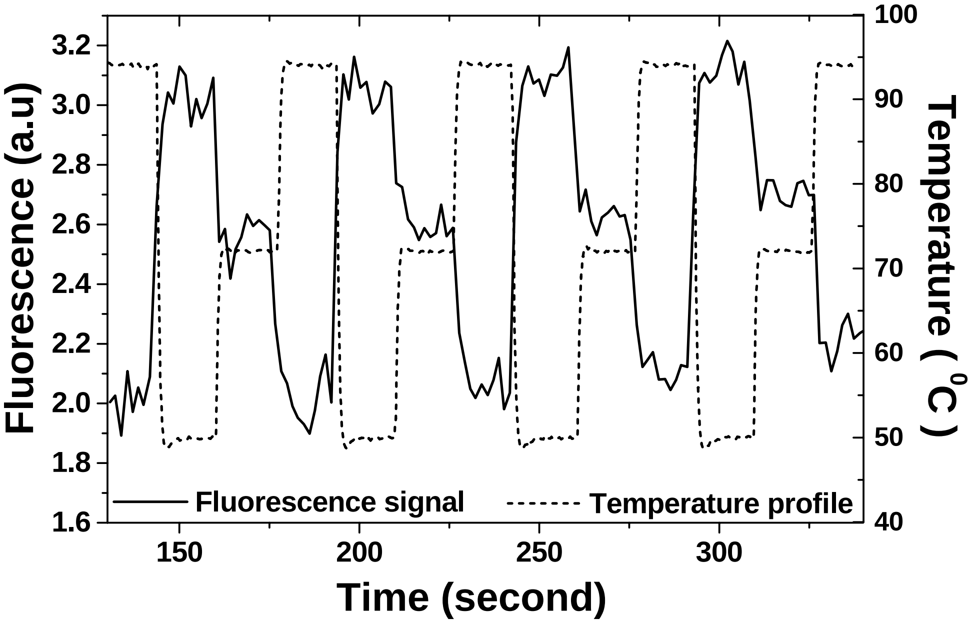

Figure 5.4. *A typical on-chip real-time PCR data profile using TOPRO-3. Due to the thermal dependence of the fluorescent intensity of the dyes, the three stages of the PCR cycle can be clearly distinguished by fluorescence measurements using the integrated waveguides. The fluorescence signal traces correspond perfectly to the measured temperature profile in the chip.*

In this approach, the temperature deviation during the temperature switching is less than 0.5 °C. Such tiny deviations are mainly caused by over compensation through the PID control algorithm. A more accurate feedback control algorithm may eliminate it. The PCR thermocycling has been optimized previously in order to decrease the cycling time. [121] The achievement of fast cooling (20 ± 2 °C/s) and heating (11 ± 1 °C/s) rates reduced the whole PCR process on-chip to only 30 - 40 minutes in comparison to one and a half hours on a conventional PCR thermocycler (Chromo4®, MJ Research, Inc., USA). Therefore, this prototype can be developed towards a portable Lab-on-a-chip system for rapid screening of pathogens in the field.

Possible surface induced inhibition is always a critical issue in microfabricated PCR devices [120, 176-179]. To avoid any inhibition from the SU-8 surface, 1 µg/µL non-acetylated bovine serum albumin (BSA) was added to the PCR mix. The BSA suppresses the interaction of the PCR reagents with the SU-8 surface and thus prevents inhibition. The non-acetylated BSA did not add to the background fluorescent. Furthermore, the applied dye concentrations in the PCR mixture are optimized and limited to 200 nM to avoid any PCR inhibition effects.

By taking the mean fluorescent signal value during the elongation period of each thermal cycle, the relative PCR product concentration for each PCR cycle can be determined quantitatively. The results of real-time PCR on chip using SYTOX Orange to detect the *Campylobacter jejuni cad*F gene [170] for different DNA template concentrations (from 2 to 200 ng/mL corresponding to about 2.8×10^4 – 2.8×10^7 *Campylobacter* genome equivalents per chip) are shown in Fig. 5.5A. Results of gel electrophoresis for the PCR products, both on chip and in tube, are shown in Fig. 5.5B. The PCR cycle threshold values (C_T) for the different DNA template concentrations can be clearly determined from the real-time PCR profile.

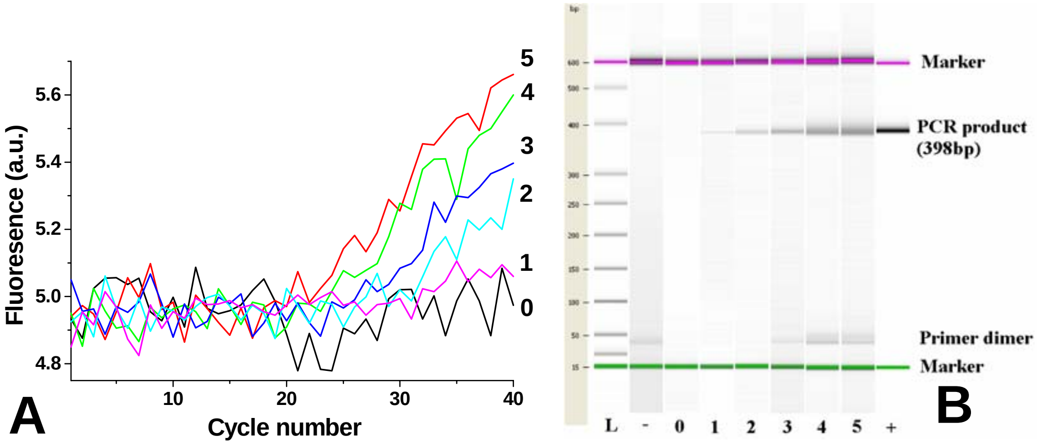

Figure 5.5. A: *Results from real-time PCR on chip to amplify the 398 bp amplicon on the Campylobacter jejuni cadF gene using SYTOX Orange. 0.: negative control on chip; 1-5.:real-time PCR on chip for detection of the*

Campylobacter jejuni DNA template series (2, 10, 20, 100, and 200 ng/mL); ***B:*** *Results for gel electrophoresis on an Agilent Bioanalyzer DNA500 chip. L: DNA marker ladder (15-600bp); -.: negative control in tube; +.: positive control in tube; numbers correspond to the samples mentioned above.*

The C_T value represents the cycle number at which the PCR product concentration is above the threshold level, as shown in equation (5.1).

$$Conc_T = Conc_0 \times (1+\varepsilon)^{C_T} \qquad (5.1)$$

Where $Conc_T$ and $Conc_0$ are the concentrations of PCR product at the threshold level and the initial template concentration, respectively, and ε is the PCR reaction efficiency. If the efficiency is 100% the concentration will double for each thermocycle, but in practice the efficiency will often be somewhat lower. Since the threshold level is constant, the C_T value should be proportional to the logarithm of the PCR template concentration.

$$C_T = mLog(Conc_0) + b \qquad (5.2)$$

Where $m = -(\log(1+\varepsilon))^{-1}$ and $b = (\log(2\varepsilon))^{-1}\log(Conc_T)$. The efficiency of the PCR reaction can be determined from the parameter m using equation (5.3):

$$\varepsilon = 10^{-1/m} - 1 \qquad (5.3)$$

Ideally, the final PCR product concentration as measured by gel electrophoresis should be proportional to the PCR template concentration, as shown in equation (5.4).

$$Conc_{product} = Conc_0 \times (1+\varepsilon)^{C_{End}} = Conc_0 \times k \qquad (5.4)$$

where $Conc_{product}$ is the concentration of the PCR product after C_{End} thermo cycles and $k = (1+\varepsilon)^{Cend}$.

The results obtained from the real-time PCR microchips showed the expected logarithmic correlation between C_T and the DNA template concentration (Fig. 5.6A), and the expected linear correlation between the PCR product concentration and the DNA template concentration (Fig. 5.6B) for both dyes. Linear regression of the C_T vs. Log($Conc_0$) plot according to equation (5.2) yields $m = -3.95$ and $b = 30.7$ for SYTOX Orange, and $m = -4.41$ and $b = 34.7$ for TO-PRO-3. By using equation (5.3) the reaction efficiency can be calculated to be 79% and 69% for SYTOX Orange and TO-PRO-3, respectively. The lower efficiency measured for TO-PRO-3 may indicate that this dye inhibits the reaction more than SYTOX Orange under the same conditions. Control PCR reactions in tubes on a conventional PCR thermocycler were performed in parallel. The results of these controls were: $m = -3.56$ and $b = 28.1$ for SYTOX Orange, and $m = -3.59$ and $b = 32.4$ for TO-PRO-3, corresponding to a reaction efficiency of 90% and 89% for SYTOX Orange and TO-PRO-3, respectively. The parameter b represents the expected C_T value of a sample with 1 pg/µL DNA template.

The C_T value measurements (Fig. 5.6A) provide more accurate information about the initial DNA template concentrations than the measurements of the final PCR product concentration (Fig. 5.6B). These results are in agreement with the literature. [105, 106] Furthermore, the dynamic range of the C_T value measurements can be extremely high: more than six orders of magnitude. [105, 106]

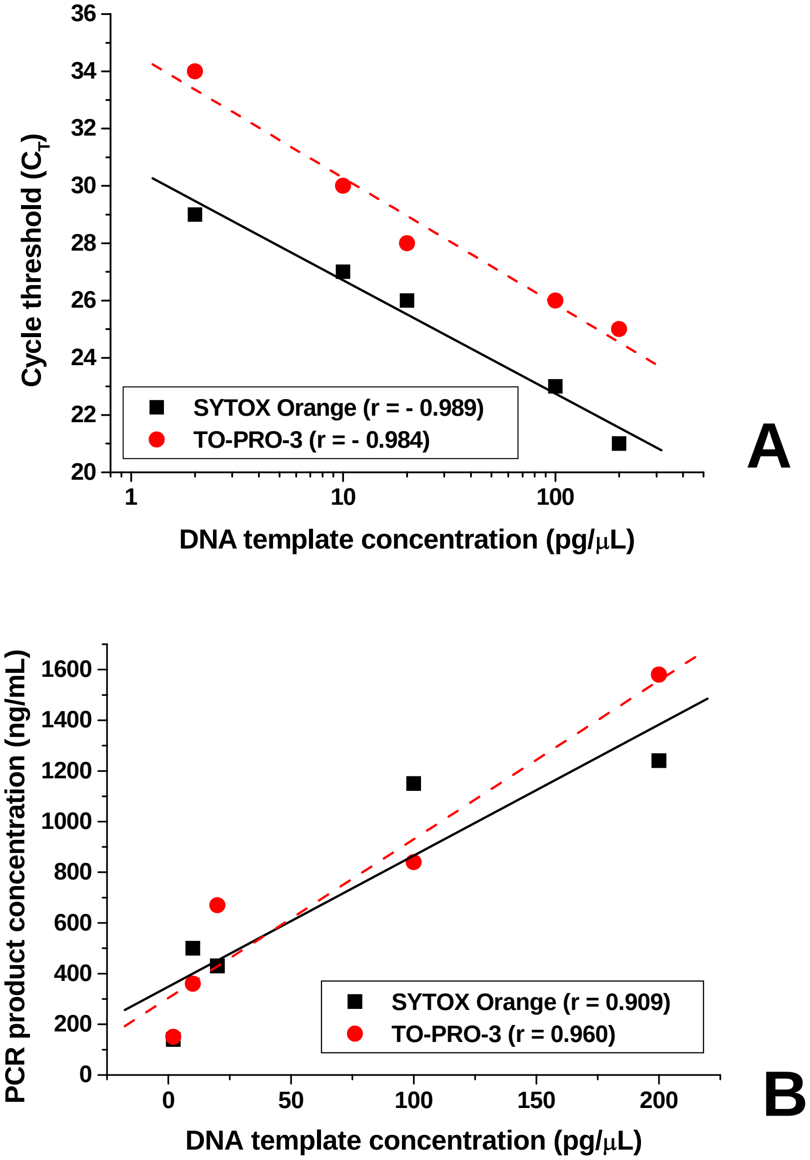

Figure 5.6. *Two DNA binding dyes (SYTOX Orange and TO-PRO-3) with different excitation wavelengths were used for detection of the Campylobacter*

jejuni cadF gene on the real-time PCR chip. **A:** *The internal assay (C_T) for both dyes shows good linear relationships with the logarithm of the DNA template concentration series;* **B:** *The external end-point assay results (obtained via DNA gel electrophoresis) can only indicate the trend of the DNA template concentrations.*

The PCR efficiency on microchip is about 10% lower than the conventional PCR in tube. This is probably manly due to the high surface to volume ratio problem and surface inhibition [121] However, the detection limit of the PCR microchip is sufficient for the *Campylobacter jejuni* detection. A better surface to volume ratio consideration design and good surface coating that may provide an even higher PCR efficiency of this microchip are focus points for further development of the PCR microchip.

5.4 Conclusions

To our knowledge, this is the first time monitoring of real-time PCR using integrated optical elements in a lab-on-a-chip system has been demonstrated. All the integrated polymer optical systems were defined in the same SU-8 layer as the PCR reaction chamber, without any extra mask step. By using two fluorescent DNA binding dyes with suitable excitation and emission spectra (SYTOX Orange and TO-PRO-3), the progression of the PCR amplification could be followed efficiently. The measured C_T value on the chip provided more accurate quantitative information about the initial DNA template concentrations in comparison to the conventional post PCR analysis by capillary gel electrophoresis. The integrated optical system described in this study allows real-time monitoring of the reaction dynamics at any location inside the micro reaction system and can be integrated into various types of microchips to facilitate real-time monitoring for a number of different purposes. Integration of thermal control and polymer waveguides for real-time PCR is thus an important step toward a portable microchip system for pathogen detection.

Acknowledgments

We would like to thank Dr. Klaus B. Morgensen for his useful suggestions for the integrated optical system design. The research was supported by the Danish Technical Research Council (STVF) (Grant no. 26-02-0307) and EU STREP project OptoLabCard.

Chapter 6: Whole genome expression profiling using DNA microarray for determining biocompatibility of polymeric surfaces [†]

M. Stangegaard[1], Z. Wang [1], J.P. Kutter, M. Dufva[*], A. Wolff

[1] Both authors contributed equally to the work.
Department of Micro and Nanotechnology, Technical University of Denmark,
Ørsteds Plads 345 east, DK-2800 Kgs. Lyngby, Denmark. Tel: +45 4525 6324;
Fax: +45 4588 7762; E-mail: mdu@mic.dtu.dk

Abstract

There is an even increasing need to find surfaces that are biocompatible for application like medical implants and the microfluidics based cell culture systems. The biocompatibility of totally five different surfaces was determined using gene expression profiling as well as more conventional methods to determine biocompatibility like, cellular growth rate, morphology and the hydrophobicity of the surfaces. HeLa cells grown on polymethylmethacrylate (PMMA) or a SU-8 surface treated with HNO_3-CAN and ethanolamine showed no differences in growth rate, morphology or gene expression profiles as compared to HeLa cells grown in cell culture flasks. Cells grown on SU-8 treated with only HNO_3-CAN showed almost the same growth rate (36±1 h) and similar morphology as cells grown in cell culture flask (32±1 h), indicating good biocompatibility. However, more than 200 genes showed different expression levels in cells grown on SU-8 treated with HNO_3-CAN compared to cell grown on cell culture flask. This shows that gene expression profiling is a simple and precise method to determine differences that is otherwise difficult to find using conventional methods in cells grown on different surfaces. It is particularly noteworthy that no correlation was found between surface hydrophobicity and biocompatibility.

Keywords: SU-8, Surface modification, Contact angle, Cell culture, Cell patterning, Gene expression, Microarray

6.1 Introduction

Polymeric materials (*e.g.*, polymethylmethacrylate (PMMA)) have been used since the 1960s in orthopedic surgery. [180] More recently, polymer materials have been used in micro total analysis systems (µTAS) for cell biology research. [127, 181, 182] Culturing cells *in vitro* requires biocompatible surfaces. [183] A

[†] Submitted to Molecular Biosystems in Jun. 2006, accept in Jul. 2006

biocompatible surface is a surface without of both negative (cytotoxic) and positive effects with regard to biofunctionality, *i.e.,* the promotion or obstruction of biological processes compared to a reference surface. [128, 129, 184] Surfaces can be rendered biocompatible for tissue and cell culturing studies by coating them with fibronectin [130-132] or hydrophilic polymer materials [133], or treating them with O_2 plasma [134]. However, those coating processes may be laborious and expensive, and the coating may prove unstable over time.

Cytotoxicity determination is an important aspect in biomaterial testing standards such as those proposed by the International Organization for Standardization (ISO) and the American Society for Testing and Materials (ASTM). However, the absence of cytotoxicity as, *e.g.*, measured by the 3-(4,5-dimethylthiazol-2-yl)-2,5-diphenyl-tetrazolium bromide (MTT) test [185] or the fluorescent membrane integrity test (FMIT) [136], does not necessarily imply that a biomaterial is biocompatible. For each application, tests have to be conducted in settings reflecting the natural environment and the demands posed on the application to elucidate the biocompatibility of the biomaterial. The biocompatibility of a material has been related to cellular functions like adhesion [136-138] and spreading [139] on the surface, proliferation rate [138], metabolic activity [138], surface inhomogeneity and moderate wettability [135]. However, as evident in some reports, increasing the surface wettability does not necessarily correspond to an increased biocompatibility. [140, 141]

As an epoxy-based negative constructional photoresist, SU-8 is widely used for fabricating microstructures in various µTAS devices because of its excellent chemical stability, optical properties and fast fabrication process. [24, 28, 29, 152, 186, 187] However, the SU-8 epoxy surface is not biocompatible. [188] Coating of the SU-8 surface with polymers [120, 166] have been reported to result in temporary biocompatibility. Chemical treatments have the potential to modify the SU-8 surface properties for extended periods of time, and can easily be combined with other micro fabrication processes. The epoxy moieties on the SU-8 surface are generally not reactive with standard corrodents (e.g., THF, HCl or HNO_3) [26, 27], reflecting the pronounced chemical stability of SU-8. However, with the catalyst ceric ammonium nitrate (CAN, $(NH_4)_2Ce(NO_3)_6$), the epoxy rings was reported to open under the reaction with HNO_3 [189] or acetic acid [190]. Recently such reaction mechanism was applied to render SU-8 hydrophilic for using in micro channel fabrication. [190]

Gene expression profiling using DNA microarrays has been widely used in the past 10 years to unravel molecular events within cell cycle regulation [191, 192], response to growth factors [193] and cellular responses to irradiation [194]. DNA microarrays are used as cancer classifiers [195-198] because there is strong evidence that the gene expression profile differs in cancer cells compared to their "normal" counterparts. The DNA microarrays normally used consist of DNA probes that is complementary to about 40,000 genes or possible genes. In one batch process, the expression level of these 40,000 genes in a particular cell can be monitored and compared to a reference cell. Culturing cells on a surface that are not biocompatible will most likely induce changes in the mRNA expression profile of a cell. [199] This became apparent when studying changes in gene-expression in MG63 osteoblast-like cells grown on zirconium oxide [200] where genes involved in immunity, cell cycle, and vesicular transport showed significant changes compared to the reference system.

In this report, we compare different methods to determine biocompatibility such as contact angle measurements and aspects of mammalian cell culturing (including morphology and growth kinetics) and whole genome expression profiling. The biocompatibility methods were tested using cells grown on modified and unmodified SU-8 as well as on unmodified PMMA.

6.2 Results and discussions

6.2.1 Surface modifications

Because SU-8 and PMMA are popular materials for building microfluidics structure [29], these materials were evaluated in biocompatibility tests and compared to polystyrene (PS) cell culture flasks. SU-8 as well as PMMA is highly hydrophobic, suggesting that they may be less suitable for cell growth. [129] Therefore, a method was developed to modulate the hydrophobicity of SU-8. A simple two-step chemical surface treatment resulted in a hydrophilic SU-8 surface. The assumed chemical reaction mechanism of the protocol is shown in Fig. 6.1: The HNO_3-CAN treatment opens the SU-8 epoxy groups and converts them into nitro groups. [189] This surface can subsequently be modified with ethanolamine (Fig. 6.1). [190]

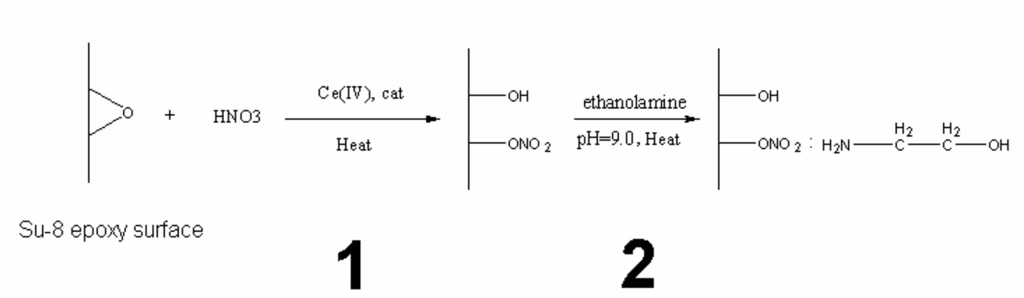

Figure 6.1. *Proposed reaction scheme of the two-step SU-8 surface modification:* ***1:*** *The epoxy ring on the SU-8 surface is believed to be opened by treatment with HNO_3-CAN;* ***2:*** *The nitrato radical on the modified SU-8 surface reacts with the amino group of ethanolamine.*

The water contact angle was measured on the differently modified SU-8 surfaces, on PMMA and on PS cell culturing flasks. Treatment of SU-8 with HNO_3-CAN decreased the contact angle from 95 ° to 45 ° (Fig. 6.2).

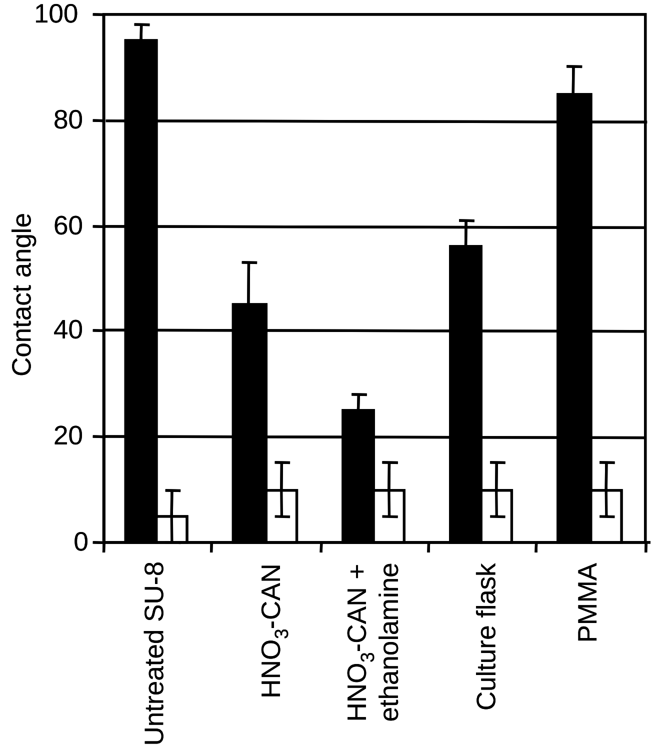

***Figure 6.2.** Water contact angles of different surfaces. The hydrophobicity of differently surfaces was determined by measuring the contact angle of water. Solid columns represent measurements performed on surfaces prior to incubation with cell culture media. Hollow columns represent water contact angles on surfaces after incubation with cell culture media under culturing conditions (37 ℃, 5 % CO_2) in the incubator for 24 hours. Prior to measuring the contact angles, surfaces were dried under a gentle stream of N_2.*

The contact angle of SU-8 could be further decreased to 25 ° by treating SU-8 first with HNO_3-CAN and then with ethanolamine. Ethanolamine had no effect on the contact angle without the initial HNO_3-CAN treatment. The contact angle of SU-8 treated with HNO_3-CAN and ethanolamine changed back to about 50° after storage at room temperature for two months. In contrast, the surface of SU-8 treated with HNO_3-CAN was chemically stable over time as determined by contact angle measurements. Furthermore, it also tolerated the ultrasonic agitation lift-off process of photoresist in acetone. The contact angle of a PMMA sheet was measured to be 85° and the PS cell culturing flask was determined to be 56 ° (Fig. 6.2). These two surfaces were served as control surfaces for the study of the differently treated SU-8 surfaces. As contact angles measured on a dry surface hardly reflect the environment encountered by the cells during culturing, the different surfaces were exposed to cell culture media and incubated for 24 hours under cell culturing conditions. After drying under a gentle stream of N_2, all surfaces had a contact angle with water that was less than 15° (Fig. 6.2). The reduction of the contact angle to approximately 15° is most likely caused by adsorption of proteins to the respective surfaces. Protein binding has indirectly been observed on untreated PMMA and SU-8 because PCR microchips made in SU-8 and PMMA require at least two fold more enzyme to sustain PCR reactions [120, 121]. Furthermore, both SU-8 and PMMA can directly form covalent bonds with single stranded amino modified DNA [153, 201], indicating that these surfaces are reactive to amine containing biomolecules such as DNA and proteins.

6.2.2 Morphology and growth kinetics

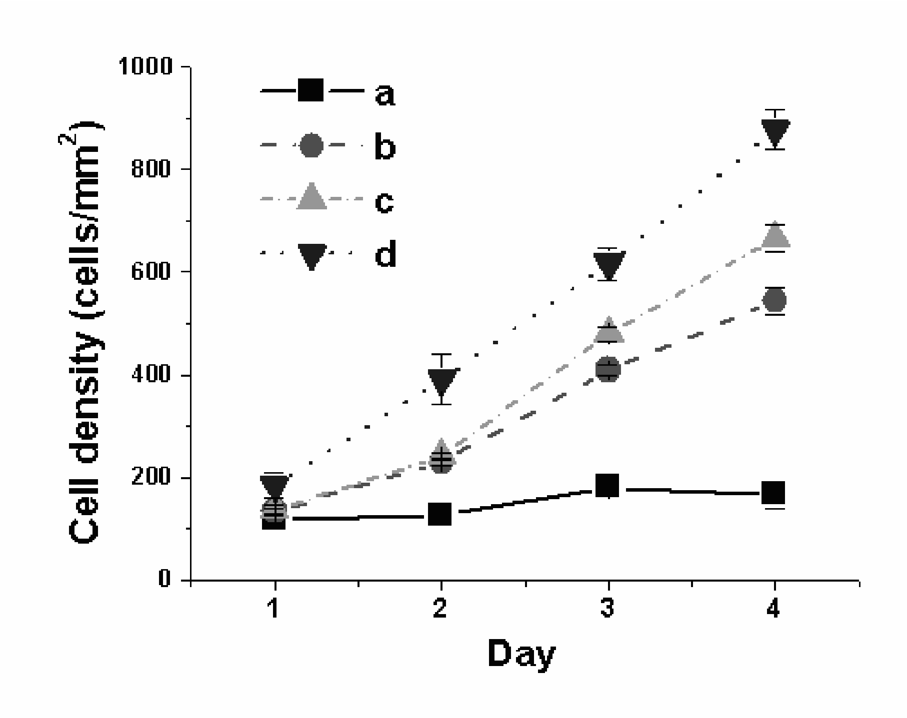

Figure 6.3. Growth kinetics of HeLa cells on the differently modified SU-8 surfaces. Samples of the differently modified SU-8 surfaces were immersed in standard cell culture media in separate cell culture flasks and seeded with equal amounts of HeLa cells. The samples were incubated for 4 days in the incubator. The cells were inspected every 24 hours and three to four representative pictures were taken on each surface on each occasion for cell counting. The entire culturing experiment was repeated twice and the cell counts were averaged. The error bars represent the standard deviation. The number of attached cells was

manually counted for calculation of the cell densities. The label letters refer to the following different surfaces: ***(a)****. Untreated SU-8;* ***(b)****. SU-8 treated with* HNO_3*-CAN;* ***(c)****. SU-8 treated with* HNO_3*-CAN and ethanolamine;* ***(d)****. Control culture flask surface.*

Five different surfaces (Fig. 6.2) were tested for biocompatibility by comparing cell morphology and growth characteristics. HeLa cells were seeded on the different surfaces and the cell density was determined throughout a four day period. Untreated SU-8 had a very high generation time of 147 ± 56 hours, indicating an unusual slow growth compared to the reference cell culture flask, which had a generation time of 32 ± 1 hours (Fig. 6.3). The images show that the few cells attached to untreated SU-8 were elongated compared to cells grown in the culture flask. Very few dividing cells were observed on untreated SU-8. Treatment of SU-8 with HNO_3-CAN resulted in a surface that supported HeLa cell growth with a generation time of 36 ± 1 hours (Fig. 6.3). By contrast, SU-8 surfaces treated with HNO_3-CAN and ethanolamine sustained cell growth rates, indistinguishable from cell growth rates in a cell culturing flask. Both surfaces resulted in a cell generation time of approximately 32 hours. The morphologies of cells cultured on the SU-8 surface treated with HNO_3-CAN closely resembled the morphology of cells cultured on SU-8 surface treated with HNO_3-CAN and ethanolamine and the culture flask surface (supplement Figure 1-2). Similar to cells grown on SU-8 treated with HNO_3-CAN and ethanolamine, cells grown on PMMA showed no differences in morphology or growth rate compared to cells grown in cell culture flasks. These results show that the growth rate does not correlate with the hydrophobicity of the investigated surfaces. PMMA had, for instance, a higher initial hydrophobicity than SU-8 treated with HNO_3-CAN and ethanolamine (Fig. 6.2). Incubating the surfaces with cell culturing medium resulted in a similar hydrophobicity (15 °C) for all the surfaces, suggesting that all surfaces should sustain growth with similar efficiency. However, this was not observed.

SU-8 might be releasing chemical factors such as residual solvents or monomers from the polymerization and lithographical processes. Such factors might be responsible for the different growth kinetics as well as the differences in morphology observed on the different SU-8 surfaces tested. The existence of such factors was tested by growing cells on SU-8 samples that were patterned chemically so that the samples contained small checkerboard or circular areas that were biocompatible. Such patterns were created on the SU-8 surface by masking the SU-8 surface prior to treatment with HNO_3-CAN and ethanolamine. The cells avoided areas that had not been exposed to HNO_3-CAN and ethanolamine. Two or three cells were observed in 50 µm × 50 µm patterned squares, while no or few cells were observed on adjacent untreated surfaces (Fig. 6.4A). After cell division, cells on the patterned areas decreased in either size or attachment area, rather than colonizing on untreated SU-8. On the 5 µm wide concentric circles, the cells appeared elongated and convex rather than round, indicating that the cells actively avoided the untreated SU-8 surface (Fig. 6.4B). Taken together these results demonstrate that SU-8 can be patterned with defined areas that sustain cell growth using the suggested novel method and that chemicals diffusing out of the bulk material are not causing the lack of growth on untreated SU-8 since cells separated by only one or two µm displayed different morphologies and growth rates.

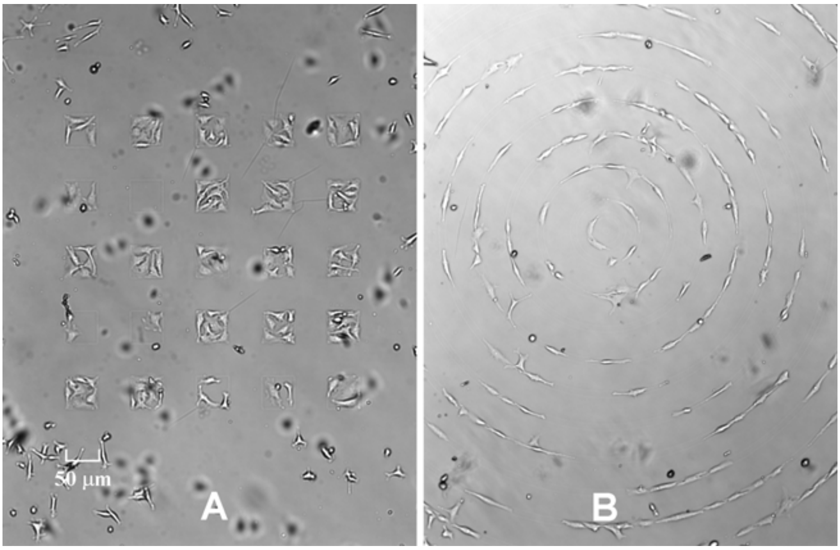

Figure 6.4. *HeLa cells cultured over night on SU-8 surfaces patterned with the HNO_3-CAN ethanolamine treatment.* ***A:*** *HeLa cells grown on an array of 50 µm × 50 µm squares. The dark areas observed to be out of focus are cells adhering to the bottom of the culture flask below the pattern* ***B:*** *HeLa cells grown on the 5 µm wide concentric circles. The cells appeared to change their morphologies to fit on to the HNO_3-CAN and ethanolamine treated patterns, avoiding contact to the untreated SU-8.*

6.2.3 Whole genome expression profile comparison of cells grown on different surfaces

DNA microarray analysis was used to determine the differences in gene expression profile on cells cultured on various surfaces. Therefore, the gene expression profiles of cells cultured on PMMA, SU-8, SU-8 treated with HNO_3-CAN, and SU-8 treated with HNO_3-CAN and ethanolamine were determined and compared with the gene expression profiles of cells cultured on PS cell culturing flasks. Whole genome expression profiles were generated using DNA microarrays carrying 60 bases long oligo probes directed against the entire human transcriptome (44290 probes in total). To estimate the amount of noise, two self-

self hybridizations were performed using cDNA generated only from cells cultured in culture flasks. The results showed that 40 genes had more than a two-fold difference in expression level. However, no genes showed more than three fold difference in expression level (Fig. 6.5 A-B), and a cut-off of three fold was therefore used for detection of significant up- or down regulation. Scatter plots of the resulting hybridization intensities indicated that cells grown on untreated SU-8 and HNO_3-CAN treated SU-8 (Fig. 6.5 C-D) had significantly different gene expression profiles (i.e., genes with more than three-fold higher or lower expression levels) compared to cells grown in cell culture flasks (Fig. 6.5 A-B). Thirty-one genes were up-regulated in cells cultured on untreated SU-8 (Fig. 6.5 H), while 13 were down-regulated (Fig. 6.5 I). Of the 31 up-regulated genes, 25 were also up-regulated in cells cultured on HNO_3-CAN treated SU-8, while 12 of the 13 down-regulated genes were also down-regulated in cells grown on SU-8 treated with HNO_3-CAN. In addition, 42 genes were up-regulated and 149 genes were down-regulated in cells cultured on SU-8 treated with HNO_3-CAN compared to cells grown on the culture flask surface. In contrast, none of the genes in cells cultured on SU-8 treated with HNO_3-CAN and ethanolamine were significantly up- or down-regulated (Fig. 6.5 E). Similar to cells grown on SU-8 treated with HNO_3-CAN and ethanolamine, cells grown on PMMA showed no change in gene expression compared to cells grown in cell culture flasks (Fig. 6.5 F-G). This observation is consistent with previous finding where a cell culture chip fabricated in PMMA [181] was found to result in culture conditions indistinguishable from the culture flasks [182]. All the regulated genes are summarized in Supplementary Table 1.

Although both the cell morphology and growth kinetics of HeLa cells cultured on HNO_3-CAN treated SU-8 surface were similar to the reference culture flask surface the whole genome expression profile indicates significant differences. The differences may arise from the different chemical functional groups on the surfaces (i.e. nitrato radicals) or differences in surface charge densities. [129] Cell grown of SU-8 treated with HNO_3-CAN showed up-regulation of Rho guanine nucleotide exchange factor 15 (ARHGEF15), which encodes a specific guanine nucleotide exchange factor for RhoA. Because RhoA is inhibiting cellular spreading [202], this up-regulation indicates that cell spreading and migration might be down-regulated on HNO_3-CAN treated SU-8 relative to the culture flask. Furthermore, histone deacetylase 4 (HDAC4) was found up-regulated indicating changes in transcriptional regulation or cell cycle progression, as histone deacetylation is a mechanim for epigenetic repression. Various DNA binding proteins was found up-regulated as well as the anti-apoptotic junD proto-oncogene (JUND) indicating an increased stress stimuli. [203] Among the down regulated genes in cells cultured on HNO_3-CAN treated SU-8 were the transcription factor BTF3 required for initiation of transcription [204], beta actin, tubulin alpha chain and a dynamin like protein involved in the microtubule formation. This is consistent with the observed reduced growth kinetics. Interestingly, both tubulin and alpha actin was also found to be down-regulated in HeLa cells cultured on co-polymer films with contact angle between 53 and 57 ° compared to the cell culture flask. [199] We measured the contact angle of cell culture flasks to 57 ° indicating that *chemistry* more than *hydrophobicity* determines gene expression in cells.

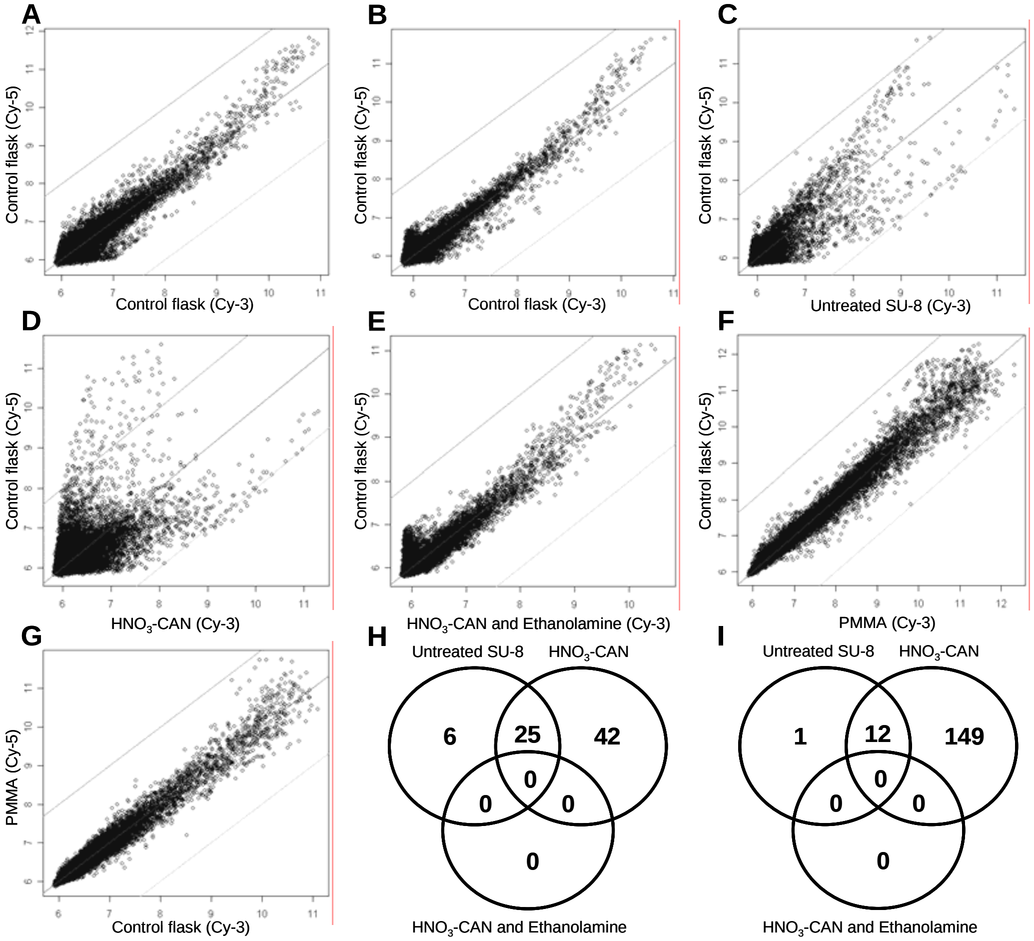

Figure 6.5. *Scatter plots of whole human genome expression profiles following four days culture on different surfaces. In all scatter plots the central line is the median and the upper and lower lines represent a fold change of 3 up and down, respectively. Data originating from the Cy-5 channel were plotted on the y-axis while the corresponding Cy-3 data were plotted on the x-axis.* ***A and B:*** *Self-self hybridization control experiments.* ***C:*** *Untreated SU-8.* ***D:*** *HNO$_3$-CAN treated SU-8.* ***E:*** *HNO$_3$-CAN and ethanolamine treated SU-8.* ***F and G:*** *PMMA.* ***H:*** *The figure displays the number of more than three fold up-regulated genes on the differently treated SU-8 surfaces relative to the reference cell culture flask. The*

numbers in the overlapping region of the circles indicates the number of genes that were up-regulated on both corresponding surfaces, while the number in the overlapping region of all three circles reflects the number of genes that were up-regulated on all three surfaces. All fold changes were measured relative to the reference cell culture flask. ***I:*** *Same as* ***H*** *but for down regulated genes. The entire list of regulated gene names and description is available in the Supplementary Table 1.*

Ideally, the effect of foreign surfaces on the cells cultured on them should be minimal or preferably none. In the case of medical implants, changes in cellular gene expression can result in cells responding differently to stimuli than normal cells, which can lead to cancer or other undesired side effects. In *in vitro* systems, it is advantageous to find environments that closely reflect the *in vivo* situation. The *in vitro* cultured cells should be functionally comparable to the corresponding cells grown *in vivo*. [184] Our results show that gene expression profiling is better than conventional functional studies like cell growth and morphology to determine biocompatibility. This is illustrated by the fact that cells grown on a test surface can show similar cell attachment, morphology and cell growth rate as cells grown on a reference surface, but still show significant differences in terms of gene expression. Without doubt, the cells grown on SU-8 surfaces treated only with HNO_3-CAN had a similar morphology and almost equal growth rate to cells grown on PMMA, cell culture flask material, and SU-8 treated with HNO_3-CAN and ethanolamine. Based on growth rate and morphology it is therefore difficult to rule out SU-8 treated with only HNO_3-CAN as a surface suitable for cell studies. Gene expression profiling, however, strongly showed that SU-8 treated with only HNO_3-CAN results in surfaces that affect cells so much as to render them significantly different in terms of gene expression from cells grown on either PMMA, cell culture flask material or SU-8 treated with HNO_3-CAN and ethanolamine. In contrast, cells grown on the three latter surfaces are very similar in terms of growth rate and morphology and also in terms of gene expression profiles. These three surfaces apparently provide comparable culturing conditions for the cells. It is however, still possible that differences on the *protein level or function* exist in cells grown on PMMA, cell culture flask material and SU-8 treated with HNO_3-CAN and ethanolamine. This cannot directly be determined using DNA microarrays, indicating that protein microarrays may be a better choice for analyzing biocompatibility in the future. Such protein microarrays may also detect secondary modifications on proteins induced by surfaces. Protein arrays are, however, less comprehensive than DNA microarrays [205], making DNA microarrays the best analysis tool currently.

6.3 Experimental section

6.3.1 Preparation of modified SU-8 surface

A 5 µm thin layer of SU-8 XP2005 negative photoresist (Microchem, Switzerland) was spin-coated on a 4” 500 µm thick Pyrex wafer (Schott Corporation, Germany). The SU-8 layer was fully cross-linked by 10 seconds UV flood exposure (9 mW/cm^2 at 365nm) and a post-bake process (on 95 ºC hotplate for 10 minutes with a 10 minutes ramp). The SU-8 surface was modified by incubation with 1 M nitric acid (Fluka, Germany), catalyzed by 0.1 M ceric ammonium nitrate (CAN, $(NH_4)_2Ce(NO_3)_6$) (Sigma, U.S.A.) at 50 °C for one hour and subsequently washed with MilliQ water. The material samples were dried and, optionally, treated with 0.1 M ethanolamine (Fluka, Germany) in 0.1 M sodium phosphate (Sigma, U.S.A.) buffer (pH 9.0) for 20 minutes at 50 °C. Finally, the material samples were washed with MilliQ water and dried.

6.3.2 Water contact angle measurements

Contact angles between the different surfaces and MilliQ water were measured by a commercial contact angle measurement instrument DSA 10 MK2 (Krüss GMBH, Germany).

6.3.3 Patterning on SU-8 surface

A two-step photolithography process was established to create the hydrophilic patterns on an otherwise hydrophobic SU-8 surface for the cell patterning experiments. A 1.5 µm layer of AZ5214e photoresist (Honeywell, U.S.A.) film was deposited on a fully developed 5 µm SU-8 layer by spin coating. The patterns on the AZ5214e photoresist were defined by standard UV lithography, and developed. Then, the whole wafer was dipped into the HNO_3-CAN solution for the first step of the surface treatment. After the HNO_3-CAN treatment, the AZ5214e photoresist layer was lifted off in acetone (Fluka, Germany), with 4 minutes of ultrasonic agitation. Finally, the whole wafer was dipped into the ethanolamine solution to finish the second step of the surface treatment. Incubation of untreated SU-8 with ethanolamine did not change the contact angle. The contact angle was only observed to decrease upon prior reaction with HNO_3-CAN. Thus, on the SU-8 surface, patterned areas were rendered hydrophilic for cell attachment while the remaining areas kept their original hydrophobic character.

6.3.4 Cell culture

Human carcinoma cells (HeLa) were cultured in 75 cm^2 culture flasks (Easyflask, Nalge Nunc International Rochester, U.S.A.) in 25 mL media (RPMI 1640 media (Sigma, U.S.A.) supplemented with 10 % Fetal Bovine Serum (FBS) (Sigma, U.S.A.), penicillin (100 U/mL) and streptomycin (100 µg/mL) (Sigma, U.S.A.)). Cells were cultured at 37 °C in an atmosphere containing 5 % CO_2 in a CO_2

incubator. Seeding of the cells was performed with a density of 6700 cells per cm^2 and the cells were passaged every three to four days when around 90 % confluence was reached, by trypsinization.

6.3.5 Target cDNA preparation

Total RNA was isolated with the RNeasy total RNA isolation kit (Qiagen, U.S.A.). Quantification of total RNA was performed using an Ultraspec 3000 spectrophotometer (Pharmacia Biotech, U.K.) and validation of RNA quality was performed using an Agilent 2100 Bioanalyzer (Agilent Technologies, U.S.A.). Amplification was performed with the Riboamp T7-based RNA amplification kit (Arcturus Engineering, U.S.A.) according to the manufacturer’s instructions using 2 μg total RNA as starting material yielding 35-40 μg amplified RNA (aRNA) after one round of amplification. Synthesis of cDNA was performed as described elsewhere [206], using random nonamers as primers.

6.3.6 Microarray hybridization

Slides containing 44,290 60 bp long oligos directed against the human genome were obtained (Agilent Technologies, USA.). Hybridization was performed according to the supplier’s instructions using 200 pmol of each of the differently Cy-labeled cDNA in a hybridization chamber (Agilent) containing a total of 490 μL hybridization solution (Agilent). The hybridization chamber was mounted on a rotation device and placed in a Hybaid Shake 'n' Stack hybridization oven (Thermo Electron Corporation, U.S.A.) for 17 hours at 60 °C with rotation (~ 4 rpm).

Following hybridization the slides were washed in washing solution 1 (6 x SSC (AppliChem, Germany), 0.005 % Triton-X-102 (Agilent)) for 10 minutes at room temperature followed by 5 minutes wash in wash solution 2 (0.1 x SSC (AppliChem, Germany), 0.005 % Triton-X-102 (Agilent)) at 4 °C. All the washing steps were performed in an in-house fabricated microarray washing station. The slides were dried by centrifugation followed by scanning and quantification performed in an ArrayWoRx microarray scanner (Applied Precision, USA).

6.3.7 Data analysis

The data was normalized using the non-linear method Qspline [207] included in the affy software package (version 1.6.7) [208] in Bioconductor software extension package version 1.6 [209] run under the freeware statistical program R (version 2.1.1) [210]. Scatter plots of the co-hybridizations were constructed with the $\log_2$ values of the Cy-3 labeled cDNA hybridization intensities on the x-axis and the $\log_2$ values of the Cy-5 labeled cDNA on the y-axis.

6.4 Conclusion

Examination of biocompatibility of the different SU-8 surfaces and PMMA showed that that contact angle measurements, morphological studies and growth kinetics might not be sufficient parameters for assessing the effect of the surfaces on cell functions. A surface, such as SU-8 treated with HNO_3-CAN, can be biocompatible with respect to cell growth, morphology, and cell adhesion, while still inducing differences in gene expression in cells grown on this substrate compared to a reference substrate. Thus, comparing the whole genome expression profiles of cells cultured for several generations on a novel surface with identical cells cultured on a reference surface gives a better indication whether the cells can be regarded as biologically comparable to the reference cells. Furthermore, gene expression profiling can be used to determine if microfluidic systems intended to simulate a particular environment *in vivo* (e.g. a blood vessel) indeed provides conditions for the cells that result in gene expression profiles that are identical to the gene expression profiles in cells in their natural environment.

Acknowledgment

We thank Jin Ulrik Louw Andersen for his testing and optimizing the treatment protocol and Maria Nordström at MIC, DTU for her kind information regarding the SU-8 treatment protocol. The research was supported by the Danish Research Council (Grant no.2014-00-0003, DABIC) and the Danish Technical Research Council (Grant no. 26-02-0307, STVF).

Supplementary Information

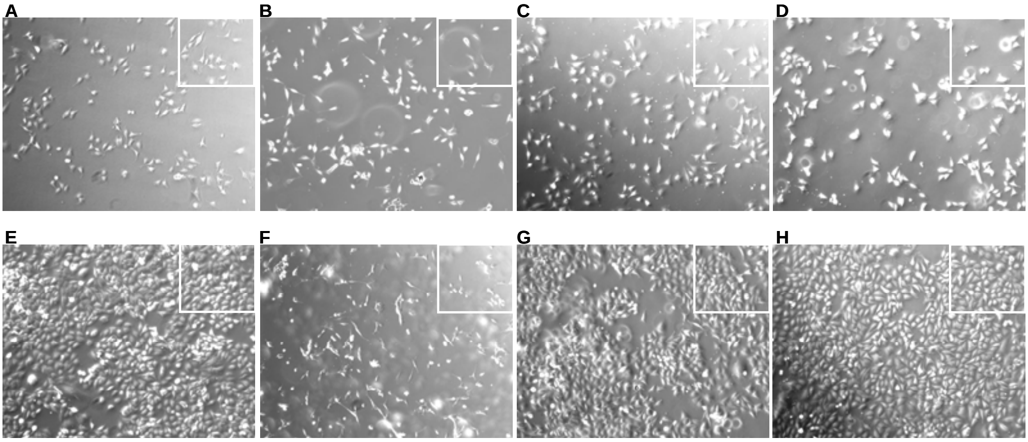

Supplementary Figure 1. *HeLa Cells cultured on differently treated SU-8 surfaces. In **A-D** the cells were cultured for 24 hours while in **E-H** the cells were cultured for four days. **A** and **E** is the reference culture flask. **B** and **F** is untreated SU-8. **C** and **G** represents SU-8 treated with HNO_3-CAN, while **D** and **E** represents SU-8 treated with HNO_3-CAN and ethanolamine. All cells originated from the same culture and were cultured under identical conditions using the same media formulation. The white rectangle indicates the area magnified in Supplementary Figure 2.*

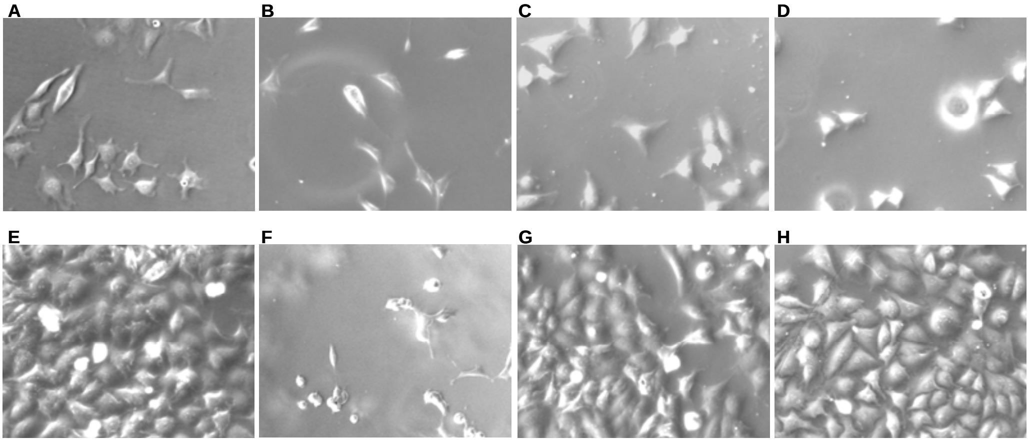

Supplementary Figure 2. *Magnification of the region indicated with a white rectangle in Supplementary Figure 1.*

Supplementary Table 1:

List of significantly regulated genes on cells cultured on SU-8 HNO_3-CAN (SU-8 CAN) and SU-8 surfaces relative to cell cultured in the culture flask. The number signifies the fold change of the gene in cells cultured on the indicated surface relative to the cell culture flask.

Name	class	Desription	SU8CAN	SU8
AF144054	Apoptosis	Homo sapiens apoptosis related protein APR-4 mRNA, partial cds. [AF144054]	3,300	
BM023129	Cell cycle	BM023129 ie79h07.x1 Melton Normalized Human Islet 4 N4-HIS 1 Homo sapiens cDNA clone IMAGE:5673444 3' similar to SW:BUB3_MOUSE Q9WVA3 MITOTIC CHECKPOINT PROTEIN BUB3 ;, mRNA sequence [BM023129]	0.332	
TAGLN2	Differentiation	Homo sapiens transgelin 2 (TAGLN2), mRNA [NM_003564]	3.349	
HSPC065	Heat shock	Homo sapiens HSPC065 protein (HSPC065), mRNA [NM_014157]	3.102	
CCL19	Ligand	Homo sapiens chemokine (C-C motif) ligand 19 (CCL19), mRNA [NM_006274]	3.800	
THC2045396	Membrane	O00429 (O00429) Dynamin-like protein, partial (16%) [THC2045396]	0.131	
AW075437	Metabolism	AW075437 xb23c01.x1 NCI_CGAP_Kid13 Homo sapiens cDNA clone IMAGE:2577120 3' similar to WP:C17G10.8 CE16861 FAT-3: ALCOHOL DEHYDROGENASE ;, mRNA sequence [AW075437]	0.314	
HAAO	Metabolism	Homo sapiens 3-hydroxyanthranilate 3,4-dioxygenase (HAAO), mRNA [NM_012205]	4.733	3.885
ABHD9	Metabolism	Homo sapiens abhydrolase domain containing 9 (ABHD9), mRNA [NM_024794]	3.689	
NPEPL1	Metabolism	Homo sapiens aminopeptidase-like 1 (NPEPL1), mRNA [NM_024663]	3.837	4.054
PNPO	Metabolism	Homo sapiens pyridoxine 5'-phosphate oxidase (PNPO), mRNA [NM_018129]	3.978	
SLC27A1	Metabolism	Homo sapiens solute carrier family 27 (fatty acid transporter), member 1 (SLC27A1), mRNA [NM_198580]	3.066	
THC2159243	Metabolism	RIB2_HUMAN (P04844) Dolichyl-diphosphooligosaccharide--protein glycosyltransferase 63 kDa subunit precursor (Ribophorin II) (RPN-II) (RIBIIR) , partial (25%) [THC2159243]	0.311	
THC2200192	Metabolism	THU1_HUMAN (Q9NXG2) THUMP domain containing protein 1, partial (69%) [THC2200192]	0.155	
AI918632	Metabolism	ts32h01.x1 NCI_CGAP_Ut4 Homo sapiens cDNA clone IMAGE:2230321 3' similar to gb:X60221 ATP SYNTHASE B CHAIN, MITOCHONDRIAL PRECURSOR (HUMAN);, mRNA sequence [AI918632]	0.118	
AI267511	Mitochondria	AI267511 aq65g08.x1 Stanley Frontal SN pool 2 Homo sapiens cDNA clone IMAGE:2035838 similar to gb:X16560 CYTOCHROME C OXIDASE POLYPEPTIDE VIIC PRECURSOR (HUMAN);, mRNA sequence [AI267511]	0.294	

AI961400	Mitochondria	AI961400 wt22a12.x1 NCI_CGAP_Ut1 Homo sapiens cDNA clone IMAGE:2508190 3' similar to gb:X60036 MITOCHONDRIAL PHOSPHATE CARRIER PROTEIN PRECURSOR (HUMAN);, mRNA sequence [AI961400]	0.070	
THC2200745	Mitochondria	DAAMTTGRG Damaliscus dorcas mitochondrial 12S and 16S ribosomal RNA genes, and Phe-, Val-, and Leu-tRNA genes, partial (5%) [THC2200745]	0.074	
AI278811	Oncogene	AI278811 qo50a11.x1 NCI_CGAP_Co8 Homo sapiens cDNA clone IMAGE:1911932 3' similar to gb:K02276 MYC PROTO-ONCOGENE PROTEIN (HUMAN);, mRNA sequence [AI278811]	0.164	
THC2134410	Oncogene	AI732190 ae38f11.x5 Gessler Wilms tumor Homo sapiens cDNA clone IMAGE:898125 3', mRNA sequence [AI732190]	4.095	
AY117690	Oncogene	Homo sapiens lung cancer oncogene 5 (HLC5) mRNA, complete cds. [AY117690]	0.312	
TMEFF2	Oncogene	Homo sapiens mRNA for tomoregulin, complete cds. [AB004064]	0.305	0.104
AY170823	Oncogene	Homo sapiens transformation-related protein 2 mRNA, complete cds. [AY170823]	0.303	
AI457687	Other	AI457687 tj48g10.x1 Soares_NSF_F8_9W_OT_PA_P_S1 Homo sapiens cDNA clone IMAGE:2144802 3' similar to TR:O22899 O22899 RNA HELICASE ISOLOG. ;, mRNA sequence [AI457687]	0.276	
AI937689	Other	AI937689 wp82d09.x1 NCI_CGAP_Brn25 Homo sapiens cDNA clone IMAGE:2468273 3' similar to gb:M32886 SORCIN (HUMAN);, mRNA sequence [AI937689]	0.275	
ADM	Other	Homo sapiens adrenomedullin (ADM), mRNA [NM_001124]	3.745	
AF271776	Other	Homo sapiens DC48 mRNA, complete cds. [AF271776]	0.227	
DPYSL3	Other	Homo sapiens dihydropyrimidinase-like 3 (DPYSL3), mRNA [NM_001387]	3.949	
FTH1	Other	Homo sapiens ferritin, heavy polypeptide 1, mRNA (cDNA clone IMAGE:3874046). [BC032091]	0.084	
FTHL7	Other	Homo sapiens ferritin, heavy polypeptide-like 7 (FTHL7) on chromosome 13 [NR_002202]	0.075	
XTP7	Other	Homo sapiens protein 7 transactivated by hepatitis B virus X antigen (HBxAg) (XTP7), mRNA [NM_138568]	3.777	4.126
SDK2	Other	Homo sapiens sidekick homolog 2 (chicken) (SDK2), mRNA [NM_019064]	4.410	3.912
AF187554	Other	Homo sapiens sperm antigen-36 mRNA, complete cds. [AF187554]	0.182	
THC2182978	Other	TTR320199 immunoglobulin mu heavy chain {Tursiops truncatus;} , partial (10%) [THC2182978]	4.322	
AD7C-NTP	Other	Homo sapiens neuronal thread protein AD7c-NTP (AD7C-NTP), mRNA [NM_014486]	3.823	3.404
DUB3	Protease	Homo sapiens deubiquitinating enzyme 3 (DUB3), mRNA [NM_201402]	3.069	
THC2202467	Protease	PSA7_HUMAN (O14818) Proteasome subunit alpha type 7 (Proteasome subunit RC6-1) (Proteasome subunit XAPC7) , partial (22%) [THC2202467]	0.235	

AI567808	Receptor	AI567808 tr62h05.x1 NCI_CGAP_Pan1 Homo sapiens cDNA clone IMAGE:2222937 3' similar to gb:M14043 ANNEXIN II (HUMAN);, mRNA sequence [AI567808]	0.314	0.081
THC2174183	Receptor	BC012448 thyroid hormone receptor interactor 4 {Homo sapiens;} , partial (75%) [THC2174183]	0.261	
DKFZp564K142	Receptor	Homo sapiens implantation-associated protein (DKFZp564K142), mRNA [NM_032121]	3.093	
LENG8	Receptor	Homo sapiens leukocyte receptor cluster (LRC) member 8 (LENG8), mRNA [NM_052925]	3.086	
KCNK7	Receptor	Homo sapiens potassium channel, subfamily K, member 7 (KCNK7), transcript variant C, mRNA [NM_005714]	3.679	3.157
AA780485	Ribosome	ac65f02.s1 Stratagene fetal retina 937202 Homo sapiens cDNA clone IMAGE:867483 3' similar to gb:X69392 60S RIBOSOMAL PROTEIN L26 (HUMAN);, mRNA sequence [AA780485]	0.296	0.114
AI613259	Ribosome	AI613259 ty35c04.x1 NCI_CGAP_Ut2 Homo sapiens cDNA clone IMAGE:2281062 3' similar to gb:X69391 60S RIBOSOMAL PROTEIN L6 (HUMAN);, mRNA sequence [AI613259]	0.265	0.071
BQ614035	Ribosome	BQ614035 il02g06.x1 Human insulinoma Homo sapiens cDNA clone IMAGE:6028979 3' similar to SW:RS11_HUMAN P04643 40S RIBOSOMAL PROTEIN S11. [1] ;, mRNA sequence [BQ614035]	0.219	
RPS15A	Ribosome	H.sapiens mRNA for ribosomal protein (homologuous to yeast S24). [X62691]	0.113	
RPS15A	Ribosome	H.sapiens mRNA for ribosomal protein (homologuous to yeast S24). [X62691]	0.137	
THC2194550	Ribosome	HUMCH13C3A ribosmal protein small subunit {Homo sapiens;} , partial (27%) [THC2194550]	0.067	
N75321	Ribosome	N75321 za79f05.s1 Soares_fetal_lung_NbHL19W Homo sapiens cDNA clone IMAGE:298785 3' similar to SW:RL24_HUMAN P38663 60S RIBOSOMAL PROTEIN L24. [2] PIR:JN0549 ;, mRNA sequence [N75321]	0.192	
THC2166330	Ribosome	RL35_HUMAN (P42766) 60S ribosomal protein L35, partial (67%) [THC2166330]	0.299	
THC2044542	Ribosome	RS10_HUMAN (P46783) 40S ribosomal protein S10, partial (93%) [THC2044542]	0.193	
THC2162618	Ribosome	RS3A_HUMAN (P61247) 40S ribosomal protein S3a, partial (81%) [THC2162618]	0.208	0.085
AA300289	Ribosome	AA300289 EST13009 Uterus tumor I Homo sapiens cDNA 3' end similar to similar to ribosomal protein YL10, mRNA sequence [AA300289]	0.121	
HNRPH1	RNA metabolism	Homo sapiens heterogeneous nuclear ribonucleoprotein H1 (H) (HNRPH1), mRNA [NM_005520]	0.299	
THC2084699	RNA metabolism	HSEXPORTI Exportin(tRNA) {Homo sapiens;} , partial (13%) [THC2084699]	0.204	
THC2083654	RNA metabolism	PR18_HUMAN (Q99633) Pre-mRNA splicing factor 18 (PRP18 homolog) (hPRP18), partial (31%) [THC2083654]	0.286	
AI608782	Sceleton	AI608782 tw94g05.x1 NCI_CGAP_HN6 Homo sapiens cDNA clone IMAGE:2267384 3' similar to gb:K00558 TUBULIN ALPHA-1 CHAIN (HUMAN);, mRNA sequence [AI608782]	0.244	
ACTB	Sceleton	Homo sapiens actin, beta (ACTB), mRNA [NM_001101]	0.160	

RASD1	Sceleton	Homo sapiens RAS, dexamethasone-induced 1 (RASD1), mRNA [NM_016084]	4.053	
TNNI1	Sceleton	Homo sapiens troponin I, skeletal, slow (TNNI1), mRNA [NM_003281]	3.623	3.911
THC2087016	Sceleton	HUMMYLCC smooth muscle mysoin light chain {Homo sapiens;} , partial (22%) [THC2087016]	0.295	0.129
THC2045155	Sceleton	MLRM_HUMAN (P19105) Myosin regulatory light chain 2, nonsarcomeric (Myosin RLC), complete [THC2045155]	0.269	
THC2200669	Signal	HNT1_HUMAN (P49773) Histidine triad nucleotide-binding protein 1 (Adenosine 5'-monophosphoramidase) (Protein kinase C inhibitor 1) (Protein kinase C-interacting protein 1) (PKCI-1), partial (51%) [THC2200669]	0.136	
ASB16	Signal	Homo sapiens ankyrin repeat and SOCS box-containing 16 (ASB16), mRNA [NM_080863]	4.027	
CDKAL1	Signal	Homo sapiens CDK5 regulatory subunit associated protein 1-like 1 (CDKAL1), mRNA [NM_017774]	3.116	
FAM19A4	Signal	Homo sapiens family with sequence similarity 19 (chemokine (C-C motif)-like), member A4 (FAM19A4), transcript variant 1, mRNA [NM_182522]	3.351	
FLJ90024	Signal	Homo sapiens fasting-inducible integral membrane protein TM6P1 (FLJ90024), mRNA [NM_153342]	4.265	
ARHGEF15	Signal	Homo sapiens Rho guanine nucleotide exchange factor (GEF) 15 (ARHGEF15), mRNA [NM_173728]	3.727	
SLA	Signal	Homo sapiens Src-like-adaptor (SLA), mRNA [NM_006748]	3.607	4.085
TRH	Signal	Homo sapiens thyrotropin-releasing hormone (TRH), mRNA [NM_007117]	3.015	
TRAF4	Signal	Homo sapiens TNF receptor-associated factor 4 (TRAF4), transcript variant 1, mRNA [NM_004295]	0.323	
THC2128887	Signal	WSB1_HUMAN (Q9Y6I7) WD repeat and SOCS box containing protein 1 (WSB-1) (SOCS box-containing WD protein SWiP-1), partial (55%) [THC2128887]	0.268	0.142
THC2162031	Structure	TCPH_HUMAN (Q99832) T-complex protein 1, eta subunit (TCP-1-eta) (CCT-eta) (HIV-1 Nef interacting protein), partial (80%) [THC2162031]	0.261	
HDAC4	Transciption	Homo sapiens histone deacetylase 4 (HDAC4), mRNA [NM_006037]	3.066	
JUND	Transciption	Homo sapiens jun D proto-oncogene (JUND), mRNA [NM_005354]	3.342	
TIP120A	Transciption	Homo sapiens TBP-interacting protein (TIP120A), mRNA [NM_018448]	3.298	
TCF15	Transciption	Homo sapiens transcription factor 15 (basic helix-loop-helix) (TCF15), mRNA [NM_004609]	4.081	
ZNF403	Transciption	Homo sapiens zinc finger protein 403 (ZNF403), mRNA [NM_024835]	3.413	
MKRN4	Transciption	Makorin 4 (Zinc finger protein 127-Xp) (ZNF127-Xp). [Source:Uniprot/SWISSPROT;Acc:Q13434] [ENST00000355859]	3.056	
THC2203017	Transciption	Q08243 (Q08243) CCAAT-binding protein (Fragment), partial (32%) [THC2203017]	0.295	
W45382	Transciption	W45382 zc80e10.s1 Pancreatic Islet Homo sapiens cDNA clone IMAGE:328650 3' similar to gb:D13748 EUKARYOTIC INITIATION FACTOR 4A-I (HUMAN);, mRNA sequence [W45382]	0.218	

THC2022176	Transciption	AA601920 np02d02.s1 NCI_CGAP_Pr2 Homo sapiens cDNA clone IMAGE:1115139 similar to gb:M90356_cds1 TRANSCRIPTION FACTOR BTF3 (HUMAN);, mRNA sequence [AA601920]	0.185	0.142
GLTSCR1	Tumor sup	Homo sapiens glioma tumor suppressor candidate region gene 1 (GLTSCR1), mRNA [NM_015711]	3.986	

Chapter7: Semi-standardization packaging mode for bio MEMS devices

Currently, most bio MEMS (Micro Electro Mechanical Systems) devices are produced as prototype for research purposes. The fabrication of these bio MEMS devices is at the laboratorial level. Therefore, the fabrication facilities of these bio MEMS devices are not reach a high standard in comparison to industrial traditional MEMS devices, such as RF MEMS and transducers. Furthermore, most of the bio MEMS devices are commonly fabricated from polymer materials and used external analogy circuits on print circuit board (PCB) for the disposable purpose. Therefore, many mature integrated circuit (IC) packaging technologies, for instance, wafer level bonding [211, 212], are not suitable for the plastic domination disposable bio MEMS devices comparison with those industrial traditional MEMS devices. Currently, the packaging modes for various bio MEMS devices are more like chaotic handicrafts. Non-standard packaging mode is one of the bottlenecks for a larger scale of the bio MEMS devices production. In this chapter, we presented a semi-standardization packaging mode for the bio MEMS devices that is used for embedding the packaged device as a standard IC element on PCB. A novel spring electrodes connection clamp is designed to mount the bio MEMS devices on the standardized Dual in line / Dual in parallel (DIL/DIP) socket as the devices packaging.

7.1 Structure of the spring clamp

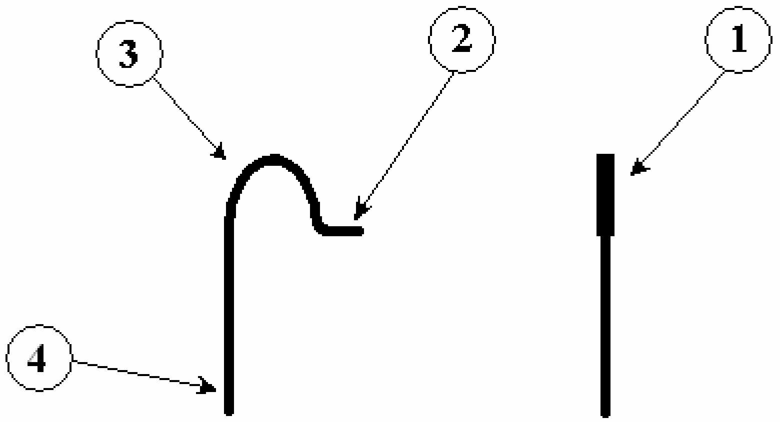

Figure 7.1. *The schematic of the spring electrode connection clamp(1). The whole spring clamp (1) is built in copper. It constitutes three parts: Electrode connection pad (2), Arch spring (3), and the socket plug-in pole (4). The out diameter of the socket plug-in pole (4) fits to the socket hole of the standardized DIL/DIP socket (9).*

The essential element in this invention is the copper spring clamp. A 0.7 mm diameter copper wire was used to make the copper spring clamp polar for match the pinhole size on the standard DIL/DIP socket. The head of the polar is forged into a flat shape, and then wrenched into an arch shape to server as a spring clamp (Fig. 7.1).

7.2 The application of the spring clamp

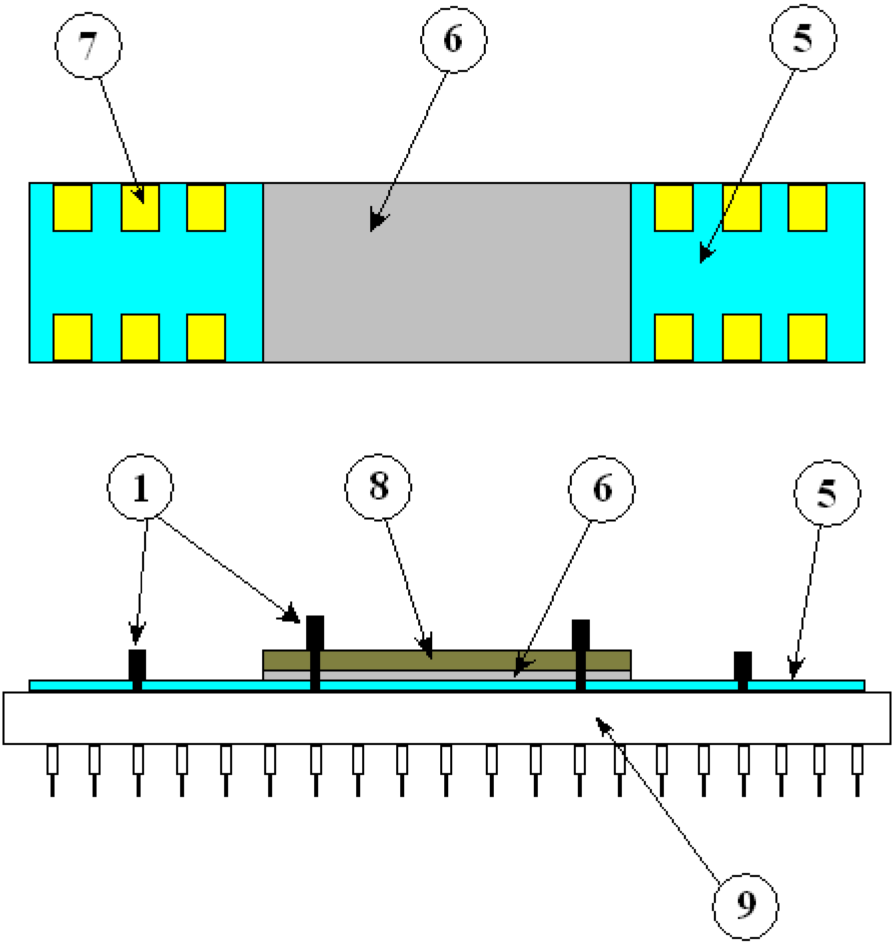

Figure 7.2. *The schematic of the standardized DIL/DIP socket MEMS device (5) and the packaging. The MEMS device (5) has the DIE of the MEMS device (6) in the middle and the chip electrodes connection pads (7) on both sides. The DIE of the MEMS device (6) is sealed by the sealing cover (8) using the spring clamps (1). The chip electrodes pads (7) are also connected onto the DIL/DIP socket by the spring clamps (1), and then connected to the PCB. Therefore the whole MEMS Device (5) is mounted on the standardized DIL/DIP socket (9) by the spring clamps (1) after the packaging.*

The spring clamp not only can connect the electrodes pads on the MEMS chips, but also can clamp the sealing layer for the MEMS devices packaging. The schematic of the spring clamp application is shown in Fig. 7.2. Using the spring clamps, the MEMS devices can easily be mounted on the standardized DIL/DIP IC socket, and can be directly plugged onto the PCB with analogy circuit design, as a standardized IC element.

An application of the semi-standardization packaging mode is shown in Fig. 7.3. A micro flow cytometer with integrated polymer waveguides is sealed with a PDMS and PMMA lid and the whole device is mounted on a 28 way standard DIL socket using the spring clamps. For easily replacement, this 28 way standard DIL socket is plugged on a 28 way standard zipper DIL socket. The zipper DIL socket can be easily soldered on the PCB for connecting with analogy circuit on the PCB. The standard DIL/DIP socket has various specifications therefore the bio MEMS device can be designed (e.g. the size of the chip, the electrode pad distance on the chip) to match one of the closed specifications.

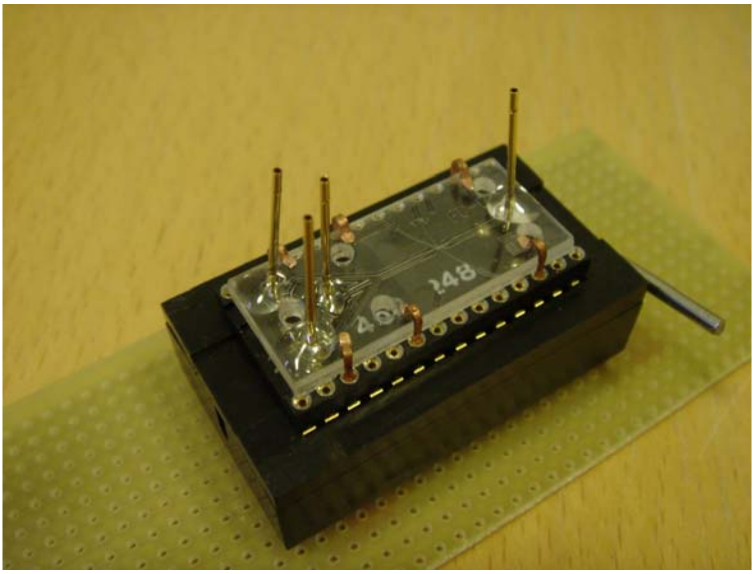

Figure 7.3. *The image shows a micro flow cytometer device is packaged on the standard DIL socket by the spring clamp. Whole device can be easily soldered on the PCB as a standard IC element.*

7.3 Retail price estimation of the μFC system

By utilization this packaging mode, the replaceable μFC device packaging, LED and photodiodes can be totally welded on a PCB as a portable μFC system prototype. The whole system can be packaged into a 20 cm × 10 cm × 5 cm large box, and driven by the 5V USB port from a laptop computer. In the table 7.1, the procurement costs are listed for the main elements of a single wavelength two detection windows μFC system.

Item	Pieces	Cost (euro)	Comments
NI USB DAQ system	1	170	
4" Pyrex wafer	0.125	27	Replaceable
40 way ZIP DIL socket	1	28	
40 way low profile DIL socket	1	1.34	Replaceable
SMA bulkhead for TO-18	3	25.2	
SMA connector	3	9	
Red LED	1	5.3	
Photodiode	2	4.7	
Sum		320	The replaceable chip packaging costs 5 euro.

Table 7.1. *The procurement costs list of the main parts for a one wavelength two detection windows μFC system. The listed prices were obtained from the retailers before Aug. 2005.*

Considering the costs of fabrication, service, and transportation etc., the final retail price for each μFC system (excluding the syringe pumps and the computer) can be estimated less than 1,000 euro. Each replaceable μFC device packaging costs less than 10 euro. For the practical reasons, each replaceable μFC device packaging can be applied for 10 times cell analysis. Therefore, the final cost for each time cell analysis can be less than 1 euro.

7.4 Conclusions

In this chapter, a novel copper spring clamp invention is presented. By applying the spring clamp for mounting the bio MEMS devices on the standard DIL/DIP socket, the packaged device can be simply plugged on the PCB as a standard IC element. Therefore, the sealing and the electrode connection problems can be solved in one packaging step. Finally, the cost of a practical μFC device (using this packaging mode) is estimated.

Chapter 8: Conclusions

The main theme of this Ph.D. project is to integrate planar polymer optical systems in the different μTAS devices to realize different optical measurement applications. During this Ph.D. project, three different type microdevice prototypes with integrated optical measurement have been developed and tested. These micro-devices have been successfully used for detection cells, investigation cell sorting, and monitoring real-time PCR, respectively.

Firstly, examination of flowing through cells/particles in a microfluidic channel was realized in an innovative microchip flow cytometer with integrated polymer optical systems. The microfluidic system and all the optical elements (waveguides, taper, lenses and fiber-to-waveguide couplers) were defined in a 90 μm thick SU-8 layer on a 500 μm borosilicate glass substrate by standard photolithography in a single mask procedure. This approach allows the fabrication and packaging of an entire device to be completed in a single day. Using the microchip flow cytometer, the scattering signals and extinction light of polystyrene beads with different sizes (3, 4.5, 6, and 9 μm) could be measured without any bulk optical system. Data of the three different signals (forward scattering, large angle scattering and extinction) for each bead showed good linear relationship ($r = 0.994$, $r = 0.979$, $r = 0.991$, respectively) with its size. By placing a band pass filter set (525 nm/22 nm) in front of the detection PMTs, the microchip flow cytometer was also successfully distinguished the propidium iodide labeled chicken red blood cells from labeled rainbow trout red blood cells. Although the scattering signals of the two cells cannot be distinguished because of their similar cell size, but the fluorescent signals of the nucleolus stained cells showed big different due to their different DNA contents.

Secondly, positive DEP cell sorting processes were real-time monitored in a novel microfluidic system with two microchip flow cytometers integrated upstream and downstream of a DEP filter. This novel microdevice is constructed by laying the 80 μm thick SU-8 microfluidic and optics components on top of a thin metal layer on the borosilicate glass substrate. By this way, only two simple photolithography steps (metal deposition, and polymer layer definition) are needed for the fabrication. The DEP filter was constructed of 62.5 pairs electrodes, each with 10 μm distance. The DEP-FC microdevice was used to study the capture efficiency of the positive DEP filter under different conditions using yeast cells as a model. The effects of the applied voltage level (1 - 20 V_{pp}), flow rate (1 - 5 mL/h), solution conductivity (0.5 – 25 mS/m), and excitation frequency (0.1 – 10 MHz) were invested. The responses on the capture efficiency were in reasonable agreement with the FEM simulation equations presented in Chapter 4. Furthermore, the DEP-FC device was also applied for real-time monitoring of viable/non-viable yeast cell sorting on the DEP filter. Under 2 MHz and 20 Vpp, more than 90% viable yeast cells were sorted from non-viable ones.

Thirdly, the PCR formation was real-time measured in a novel real-time PCR microchip with integrated polymer waveguides in the reaction chamber. Based on an existed PCR microchip, the integrated thermal system of the chip was remodeled and redesigned to expand the homogeneous heating area, from 16 mm^2 to 49 mm^2. The integrated polymer optical systems were created in the same 400 μm SU-8 layer of the reaction chamber. To avoid the high propagation loss at the low wavelength (less than 500 nm) of SU8, two suitable DNA binding dyes (SYTOX Orange (547 nm/570 nm) and TO-PRO-3 (642 nm/661 nm)) were tested and used in the real-time PCR experiments. The approach provided quantitative information of the amplified PCR progression in real-time PCR amplification of *cad*F gene of *Campylobacter juni*. The PCR reaction efficiencies of the two different dyes on the chip were 79% and 69% respectively. The measured C_T value on the chip showed more accurately quantitative information about the initial concentrations of the DNA template than the conventional gel electrophoresis. The integrated optical system allows real-time monitoring of the reaction dynamics at any location inside the micro reaction system.

Furthermore, a simple, moderate and robust SU-8 surface chemical modification protocol was studied and developed, rendering the biocompatibility of SU-8 surface for the mammalian cell culture. Several different methods, that included surface contact angle determination, morphology of the attached cells, cell growth kinetics, as well as whole genome expression profile microarray analysis, were investigated to evaluate the biocompatibility of the modified SU-8 surface. As a conclusion, the whole genome expression profile microarray analysis provided more complete information and details of the cell adhesion and growth dynamic on the surface than other methods. From the data, there might be no strong relationship between surface hydrophobicity and biocompatibility.

Through this Ph.D. study, the integrated polymer waveguides in different μTAS devices have been successfully achieved for various applications. For realizing a practical real μTAS, the integrated polymer optics technology provides a simple way for real-time monitoring in different μTAS devices. It is therefore believed that the technology of the integrated polymer optics will not only be a milestone, but also be a new research direction for the real μTAS research area.

Since the late 80's, many efforts have been carried out toward real μTAS devices. However, most of them were still at the stage of prototype. The main bottleneck is how to integrate various microstructures together and work properly. Furthermore, currently many new nanofabrication technologies have been developed, such as E-beam lithography and nano-imprint. More narrow and tiny nanostructures can now be invented using those technologies. As a courageous prospect, once the bottleneck of integration is broken through, a μTAS (even nanoTAS) market can be eventually boosted.

Bibliography

[1] A. Manz, N. Graber, H.M. Widmer, "Miniaturized Total Chemical-Analysis Systems - a Novel Concept for Chemical Sensing", *Sens. Actuator B-Chem.*, vol. 1, pp. 244-248, 1990.

[2] A. van den Berg, T.S.J. Lammerink, "Micro total analysis systems: Microfluidic aspects, integration concept and applications", *Topics in Current Chemistry*, vol. 194, pp. 21-49, 1998.

[3] D. Figeys, D. Pinto, "Lab-on-a-chip: A revolution in biological and medical sciences", *Anal. Chem.*, vol. 72, pp. 330A-335A, 2000.

[4] D.R. Reyes, D. Iossifidis, P.A. Auroux, A. Manz, "Micro total analysis systems. 1. Introduction, theory, and technology", *Anal. Chem.*, vol. 74, pp. 2623-2636, 2002.

[5] E. Verpoorte, "Chip vision - optics for microchips", *Lab on a Chip*, vol. 3, pp. 42N-52N, 2003.

[6] Z.H. Liang, N. Chiem, G. Ocvirk, T. Tang, K. Fluri, D.J. Harrison, "Microfabrication of a planar absorbance and fluorescence cell for integrated capillary electrophoresis devices", *Anal. Chem.*, vol. 68, pp. 1040-1046, 1996.

[7] L. Cui, T. Zhang, H. Morgan, "Optical particle detection integrated in a dielectrophoretic lab-on-a-chip", *J. Micromech. Microeng.*, vol. 12, pp. 7-12, 2002.

[8] M.L. Chabinyc, D.T. Chiu, J.C. McDonald, A.D. Stroock, J.F. Christian, A.M. Karger, G.M. Whitesides, "An integrated fluorescence detection system in poly(dimethylsiloxane) for microfluidic applications", *Anal. Chem.*, vol. 73, pp. 4491-4498, 2001.

[9] J.C. Roulet, R. Volkel, H.P. Herzig, E. Verpoorte, N.F. de Rooij, R. Dandliker, "Performance of an integrated microoptical system for fluorescence detection in microfluidic systems", *Anal. Chem.*, vol. 74, pp. 3400-3407, 2002.

[10] S. Camou, H. Fujita, T. Fujii, "PDMS 2D optical lens integrated with microfluidic channels: principle and characterization", *Lab on a Chip*, vol. 3, pp. 40-45, 2003.

[11] J. Seo, L.P. Lee. " Integrated microfluidic optical system (iMOS) with LED". in *microTAS2002*. Dordrecht: Kluwer Academic Publishers. 2002.

[12] B. Yao, G. Luo, L.D. Wang, Y.D. Gao, G.T. Lei, K.N. Ren, L.X. Chen, Y.M. Wang, Y. Hu, Y. Qiu, "A microfluidic device using a green organic light emitting diode as an integrated excitation source", *Lab on a Chip*, vol. 5, pp. 1041-1047, 2005.

[13] K.B. Mogensen, Y.C. Kwok, J.C.T. Eijkel, N.J. Petersen, A. Manz, J.P. Kutter, "A microfluldic device with an integrated waveguide beam splitter

for velocity measurements of flowing particles by Fourier transformation", *Anal. Chem.*, vol. 75, pp. 4931-4936, 2003.

[14] O. Leistiko, P.F. Jensen, "Integrated bio/chemical microsystems employing optical detection: the clip-on", *J. Micromech. Microeng.*, vol. 8, pp. 148-150, 1998.

[15] J.M. Ruano, V. Benoit, J.S. Aitchison, J.M. Cooper, "Flame hydrolysis deposition of glass on silicon for the integration of optical and microfluidic devices", *Anal. Chem.*, vol. 72, pp. 1093-1097, 2000.

[16] P. Friis, K. Hoppe, O. Leistiko, K.B. Mogensen, J. Hubner, J.P. Kutter, "Monolithic integration of microfluidic channels and optical waveguides in silica on silicon", *Appl. Optics*, vol. 40, pp. 6246-6251, 2001.

[17] K.B. Mogensen, P. Friis, J. Hubner, N. Petersen, A.M. Jorgensen, P. Telleman, J.P. Kutter, "Ultraviolet transparent silicon oxynitride waveguides for biochemical microsystems", *Opt. Lett.*, vol. 26, pp. 716-718, 2001.

[18] K.B. Mogensen, N.J. Petersen, J. Hubner, J.P. Kutter, "Monolithic integration of optical waveguides for absorbance detection in microfabricated electrophoresis devices", *Electrophoresis*, vol. 22, pp. 3930-3938, 2001.

[19] J.P. Valentino, S.M. Troian, S. Wagner, "Microfluidic detection and analysis by integration of thermocapillary actuation with a thin-film optical waveguide", *Applied Physics Letters*, vol. 86, pp. 1-3, 2005.

[20] R.G. Hunsperger, "Integrated optics: Theory and Technology", Second ed. 1984, Berlin: Springer-Verlag.

[21] K.B. Mogensen, F. Eriksson, O. Gustafsson, R.P. Nikolajsen, J.P. Kutter, "Pure-silica optical waveguides, fiber couplers, and high-aspect ratio submicrometer channels for electrokinetic separation devices", *Electrophoresis*, vol. 25, pp. 3788-3795, 2004.

[22] L. Robitaille, C.L. Callender, J.P. Noad, "Design and fabrication of low-loss polymer waveguide components for on-chip optical interconnection", *IEEE Photonics Technology Letters*, vol. 8, pp. 1647-1649, 1996.

[23] L. Eldada, L.W. Shacklette, "Advances in polymer integrated optics", *Selected Topics in Quantum Electronics, IEEE Journal on*, vol. 6, pp. 54-68, 2000.

[24] K.B. Mogensen, J. El-Ali, A. Wolff, J.P. Kutter, "Integration of polymer waveguides for optical detection in microfabricated chemical analysis systems", *Appl. Optics*, vol. 42, pp. 4072-4079, 2003.

[25] D. Snakenborg, K.B. Mogensen, J.P. Kutter. "Optimization of signal-to-noise ratio in absorbance detection by integration of microoptical components". in *microTAS2003*. Squaw Valley. 2003.

[26] N. Zhang, J. Xie, M. Guers, V.K. Varadan, "Chemical bonding of multiwalled carbon nanotubes to SU-8 via ultrasonic irradiation", *Smart Mater. Struct.*, vol. 12, pp. 260–263, 2003.

[27] Y. Song, C.S.S.R. Kumar, J. Hormes, "Fabrication of an SU-8 based microfluidic reactor on a PEEK substrate sealed by a ‘flexible semi-solid transfer’(FST) process", *J. Micromech. Microeng.*, vol. 14, pp. 932–940, 2004.

[28] J. Hsieh, C.J. Weng, H.L. Yin, H.H. Lin, H.Y. Chou, "Realization and characterization of SU-8 micro cylindrical lenses for in-plane micro optical systems", *Microsystem Technologies*, vol. 11, pp. 429–437, 2005.

[29] H. Lorenz, M. Despont, N. Fahrni, N. LaBianca, P. Renaud, P. Vettiger, "SU-8: a low-cost negative resist for MEMS", *J. Micromech. Microeng.*, vol. 7, pp. 121–124, 1997.

[30] H.M. Shapiro, "Practical flow cytometry", 3rd ed ed. 1995, New York: Wiley,.

[31] E. Altendorf, D. Zebert, M. Holl, P. Yager. "Differential blood cell counts obtained using a microchannel based flow cytometer". in *Tranducers 97. 1997 International Conference on Solid-State Sensors and Actuators.*: Digest of Technical Papers (Cat. No.97TH8267). 1997.

[32] D. Sobek, A.M. Young, M.L. Gray, S.D. Senturia, "A microfabricated flow chamber for optical measurments in fluids", *IEEE*, pp. 219-224, 1993.

[33] L.L. Sohn, O.A. Saleh, G.R. Facer, A.J. Beavis, R.S. Allan, D.A. Notterman, "Capacitance cytometry: Measuring biological cells one by one", *Proc. Natl. Acad. Sci. U. S. A.*, vol. 97, pp. 10687-10690, 2000.

[34] M.A. McClain, C.T. Culbertson, S.C. Jacobson, J.M. Ramsey, "Flow cytometry of Escherichia coli on microfluidic devices", *Anal. Chem.*, vol. 73, pp. 5334-5338, 2001.

[35] T. Buranda, J.M. Huang, V.H. Perez-Luna, B. Schreyer, L.A. Sklar, G.P. Lopez, "Biomolecular recognition on well-characterized beads packed in microfluidic channels", *Anal. Chem.*, vol. 74, pp. 1149-1156, 2002.

[36] J. Voldman, M.L. Gray, M. Toner, M.A. Schmidt, "A Microfabrication-Based Dynamic Array Cytometer", *Anal. Chem.*, vol. 74, pp. 3984-3990, 2002.

[37] N. Pamme, R. Koyama, A. Manz, "Counting and sizing of particles and particle agglomerates in a microfluidic device using laser light scattering: application to a particle-enhanced immunoassay", *Lab on a Chip*, vol. 3, pp. 187-192, 2003.

[38] S. Gawad, L. Schild, P. Renaud, "Micromachined impedance spectroscopy flow cytometer for cell analysis and particle sizing", *Lab on a Chip*, vol. 1, pp. 76-82, 2001.

[39] H. Bang, H. Yun, K.-C. Cho, C. Chung, D.-C. Han, J.K. Chang. "Expansion channel for microchip flowcytometer". in *microTAS2005*. Boston, MA, USA. 2005.

[40] D.P. Schrum, C.T. Culbertson, S.C. Jacobson, J.M. Ramsey, "Microchip flow cytometry using electrokinetic focusing", *Anal. Chem.*, vol. 71, pp. 4173-4177, 1999.

[41] S. Gawad, K. Cheung, U. Seger, A. Bertsch, P. Renaud, "Dielectric spectroscopy in a micromachined flow cytometer: theoretical and practical considerations", *Lab on a Chip*, vol. 4, pp. 241-251, 2004.

[42] L.S. Cram, J.C. Martin, J.A. Steinkamp, J.H. Jett, G. Saizman, L. Sklar, "New flow cytometric capability at the national flow cytometry resource", *Proc. IEEE*, vol. 80, pp. 912-917, 1992.

[43] A. Orfao, A. RuizArguelles, "General concepts about cell sorting techniques", *Clinical Biochemistry*, vol. 29, pp. 5-9, 1996.

[44] G. Blankenstein, U.D. Larsen, "Modular concept of a laboratory on a chip for chemical and biochemical analysis", *Biosens. Bioelectron.*, vol. 13, pp. 427-438, 1998.

[45] A.Y. Fu, C. Spence, A. Scherer, F.H. Arnold, S.R. Quake, "A microfabricated fluorescence-activated cell sorter", *Nat. Biotechnol.*, vol. 17, pp. 1109-1111, 1999.

[46] J. Krüger, K. Singh, A. O'Neill, C. Jackson, A. Morrison, P. O'Brien, "Development of a microfluidic device for fluorescence activated cell sorting", *J. Micromech. Microeng.*, vol. 12, pp. 486-494, 2002.

[47] A.Y. Fu, H.P. Chou, C. Spence, F.H. Arnold, S.R. Quake, "An integrated microfabricated cell sorter", *Anal. Chem.*, vol. 74, pp. 2451-2457, 2002.

[48] A. Wolff, I.R. Perch-Nielsen, U.D. Larsen, P. Friis, G. Goranovic, C.R. Poulsen, J.P. Kutter, P. Telleman, "Integrating advanced functionality in a microfabricated high-throughput fluorescent-activated cell sorter", *Lab on a Chip*, vol. 3, pp. 22-27, 2003.

[49] P.S. Dittrich, P. Schwille, "An integrated microfluidic system for reaction, high-sensitivity detection, and sorting of fluorescent cells and particles", *Anal. Chem.*, vol. 75, pp. 5767-5774, 2003.

[50] B. Yao, G.A. Luo, X. Feng, W. Wang, L.X. Chen, Y.M. Wang, "A microfluidic device based on gravity and electric force driving for flow cytometry and fluorescence activated cell sorting", *Lab on a Chip*, vol. 4, pp. 603-607, 2004.

[51] B.H. Kunst, A. Schots, A. Visser, "Design of a confocal microfluidic particle sorter using fluorescent photon burst detection", *Rev. Sci. Instrum.*, vol. 75, pp. 2892-2898, 2004.

[52] V. Studer, R. Jameson, E. Pellereau, A. Pepin, Y. Chen, "A microfluidic mammalian cell sorter based on fluorescence detection", *Microelectron. Eng.*, vol. 73-74, pp. 852-857, 2004.

[53] G.B. Lee, C.H. Lin, S.C. Chang, "Micromachine-based multi-channel flow cytometers for cell/particle counting and sorting", *J. Micromech. Microeng.*, vol. 15, pp. 447-454, 2005.

[54] M. Yamada, M. Nakashima, M. Seki, "Pinched flow fractionation: continuous size separation of particles utilizing a laminar flow profile in a pinched microchannel", *Anal Chem*, vol. 76, pp. 5465-5471, 2004.

[55] L.R. Huang, E.C. Cox, R.H. Austin, J.C. Sturm, "Continuous particle separation through deterministic lateral displacement", *Science*, vol. 304, pp. 987-990, 2004.

[56] M. Safarikova, I. Safarik, "Magnetic Separations in Biosciences and Biotechnologies", *Chem. Listy*, vol. 89, pp. 280-287, 1995.

[57] M. Zborowski, L.R. Moore, S. Reddy, G.H. Chen, L.P. Sun, J.J. Chalmers, "Magnetic flow sorting using a model system of human lymphocytes and a colloidal magnetic label", *Asaio Journal*, vol. 42, pp. M666-M671, 1996.

[58] M.A.M. Gijs, "Magnetic bead handling on-chip: new opportunities for analytical applications", *Microfluid Nanofluid*, vol. 1, pp. 22-40, 2004.

[59] K. Smistrup, O. Hansen, H. Bruus, M.F. Hansen, "Magnetic separation in microfluidic systems using microfabricated electromagnets-experiments and simulations", *J. Magn. Magn. Mater.*, vol. 293, pp. 597-604, 2005.

[60] H. Lu, S. Gaudet, M.A. Schmidt, K.F. Jensen, "A microfabricated device for subcellular organelle sorting", *Anal. Chem.*, vol. 76, pp. 5705-5712, 2004.

[61] R. Pethig, G.H. Markx, "Applications of dielectrophoresis in biotechnology", *Trends Biotechnol.*, vol. 15, pp. 426-432, 1997.

[62] P.R.C. Gascoyne, J.V. Vykoukal, "Dielectrophoresis-based sample handling in general-purpose programmable diagnostic instruments", *Proc. IEEE*, vol. 92, pp. 22-42, 2004.

[63] P.K. Wong, T.H. Wang, J.H. Deval, C.M. Ho, "Electrokinetics in micro devices for biotechnology applications", *IEEE-ASME Trans. Mechatron.*, vol. 9, pp. 366-376, 2004.

[64] T.B. Jones, "Elestromechanics of Particles". 1995: Cambridge University Press.

[65] F.F. Becker, X.B. Wang, Y. Huang, R. Pethig, J. Vykoukal, P.R.C. Gascoyne, "The Removal of Human Leukemia-Cells From Blood Using Interdigitated Microelectrodes", *J. Phys. D-Appl. Phys.*, vol. 27, pp. 2659-2662, 1994.

[66] N.G. Green, H. Morgan, J.J. Milner, "Manipulation and trapping of sub-micron bioparticles using dielectrophoresis", *Journal of Biochemical and Biophysical Methods*, vol. 35, pp. 89-102, 1997.

[67] D. Holmes, N.G. Green, H. Morgan, "Microdevices for dielectrophoretic flow-through cell separation", *IEEE Eng. Med. Biol. Mag.*, vol. 22, pp. 85-90, 2003.

[68] S. Choi, J.K. Park, "Microfluidic system for dielectrophoretic separation based on a trapezoidal electrode array", *Lab on a Chip*, vol. 5, pp. 1161-1167, 2005.

[69] I. Doh, Y.H. Cho, "A continuous cell separation chip using hydrodynamic dielectrophoresis (DEP) process", *Sens. Actuator A-Phys.*, vol. 121, pp. 59-65, 2005.

[70] G.H. Markx, J. Rousselet, R. Pethig, "DEP-FFF: Field-flow fractionation using non-uniform electric fields", *Journal of Liquid Chromatography & Related Technologies*, vol. 20, pp. 2857-2872, 1997.

[71] M.P. Hughes, R. Pethig, X.B. Wang, "Dielectrophoretic forces on particles in travelling electric fields", *J. Phys. D-Appl. Phys.*, vol. 29, pp. 474-482, 1996.

[72] P. Gascoyne, C. Mahidol, M. Ruchirawat, J. Satayavivad, P. Watcharasit, F.F. Becker, "Microsample preparation by dielectrophoresis: isolation of malaria", *Lab on a Chip*, vol. 2, pp. 70-75, 2002.

[73] G. de Gasperis, J. Yang, F.F. Becker, P.R.C. Gascoyne, X.-B. Wang, "Microfluidic cell separation by 2-dimensional dielectrophoresis", *Biomedical Microdevices*, vol. 2, pp. 41-49, 1999.

[74] P.R.C. Gascoyne, X.B. Wang, Y. Huang, F.F. Becker, "Dielectrophoretic separation of cancer cells from blood", *IEEE Trans. Ind. Appl.*, vol. 33, pp. 670-678, 1997.

[75] J. Yang, Y. Huang, X.B. Wang, F.F. Becker, P.R.C. Gascoyne, "Cell separation on microfabricated electrodes using dielectrophoretic/gravitational field flow fractionation", *Anal. Chem.*, vol. 71, pp. 911-918, 1999.

[76] I.R. Perch-Nielsen, D.D. Bang, C.R. Poulsen, J. El-Ali, A. Wolff, "Removal of PCR inhibitors using dielectrophoresis as a selective filter in a microsystem", *Lab on a Chip*, vol. 3, pp. 212–216, 2003.

[77] Y. Huang, R. Holzel, R. Pethig, X.B. Wang, "Differences in the AC electrodynamics of viable and nonviable yeast-cells determined through combined dielectrophoresis and electrorotation studies", *Phys. Med. Biol.*, vol. 37, pp. 1499-1517, 1992.

[78] M.S. Talary, R. Pethig, "Optical technique for measuring the positive and negative dielectrophoretic behavior of cells and colloidal suspensions", *Iee Proceedings-Science Measurement and Technology*, vol. 141, pp. 395-399, 1994.

[79] X.F. Zhou, G.H. Markx, R. Pethig, I.M. Eastwood, "Differentiation of viable and nonviable bacterial biofilms using electrorotation", *Biochim. Biophys. Acta-Gen. Subj.*, vol. 1245, pp. 85-93, 1995.

[80] X.F. Zhou, G.H. Markx, R. Pethig, "Effect of biocide concentration on electrorotation spectra of yeast cells", *Biochim. Biophys. Acta-Biomembr.*, vol. 1281, pp. 60-64, 1996.

[81] A.D. Goater, J.P.H. Burt, R. Pethig, "A combined travelling wave dielectrophoresis and electrorotation device: applied to the concentration and viability determination of Cryptosporidium", *J. Phys. D-Appl. Phys.*, vol. 30, pp. L65-L69, 1997.

[82] K.L. Chan, H. Morgan, E. Morgan, I.T. Cameron, M.R. Thomas, "Measurements of the dielectric properties of peripheral blood mononuclear cells and trophoblast cells using AC electrokinetic techniques", *Biochim. Biophys. Acta-Mol. Basis Dis.*, vol. 1500, pp. 313-322, 2000.

[83] S. Poser, T. Schulz, U. Dillner, V. Baier, J.M. Kohler, D. Schimkat, G. Mayer, A. Siebert, "Chip elements for fast thermocycling", *Sens. Actuator A-Phys.*, vol. 62, pp. 672-675, 1997.

[84] J.H. Daniel, S. Iqbal, R.B. Millington, D.F. Moore, C.R. Lowe, D.L. Leslie, M.A. Lee, M.J. Pearce, "Silicon microchambers for DNA amplification", *Sens. Actuator A-Phys.*, vol. 71, pp. 81-88, 1998.

[85] T.M.H. Lee, I.M. Hsing, A.I.K. Lao, M.C. Carles, "A miniaturized DNA amplifier: Its application in traditional Chinese medicine", *Anal. Chem.*, vol. 72, pp. 4242-4247, 2000.

[86] Y.C. Lin, C.C. Yang, M.Y. Huang, "Simulation and experimental validation of micro polymerase chain reaction chips", *Sens. Actuator B-Chem.*, vol. 71, pp. 127-133, 2000.

[87] B.C. Giordano, J. Ferrance, S. Swedberg, A.F.R. Huhmer, J.P. Landers, "Polymerase chain reaction in polymeric microchips: DNA amplification in less than 240 seconds", *Anal. Biochem.*, vol. 291, pp. 124-132, 2001.

[88] H. Nagai, Y. Murakami, K. Yokoyama, E. Tamiya, "High-throughput PCR in silicon based microchamber array", *Biosens. Bioelectron.*, vol. 16, pp. 1015-1019, 2001.

[89] J.N. Yang, Y.J. Liu, C.B. Rauch, R.L. Stevens, R.H. Liu, R. Lenigk, P. Grodzinski, "High sensitivity PCR assay in plastic micro reactors", *Lab on a Chip*, vol. 2, pp. 179-187, 2002.

[90] D.S. Yoon, Y.S. Lee, Y. Lee, H.J. Cho, S.W. Sung, K.W. Oh, J. Cha, G. Lim, "Precise temperature control and rapid thermal cycling in a micromachined DNA polymerase chain reaction chip", *J. Micromech. Microeng.*, vol. 12, pp. 813-823, 2002.

[91] T.M.-H. Lee, M.C. Carles, I.-M. Hsing, "Microfabricated PCR-electrochemical device for simultaneous DNA amplification and detection", *Lab on a Chip*, vol. 3, pp. 100-105, 2003.

[92] I. Erill, S. Campoy, J. Rus, L. Fonseca, A. Ivorra, Z. Navarro, J.A. Plaza, J. Aguilo, J. Barbe, "Development of a CMOS-compatible PCR chip: comparison of design and system strategies", *J. Micromech. Microeng.*, vol. 14, pp. 1558–1568, 2004.

[93] D.S. Lee, S.H. Park, H. Yang, K.H. Chung, T.H. Yoon, S.J. Kim, K. Kim, Y.T. Kim, "Bulk-micromachined submicroliter-volume PCR chip with very rapid thermal response and low power consumption", *Lab Chip*, vol. 4, pp. 401-407, 2004.

[94] C. Ke, H. Berney, A. Mathewson, M.M. Sheehan, "Rapid amplification for the detection of Mycobacterium tuberculosis using a non-contact heating

method in a silicon microreactor based thermal cycler", *Sens. Actuator B-Chem.*, vol. 102, pp. 308–314, 2004.

[95] W. Yan, L. Du, J. Wang, L. Ma, J. Zhu, "Simulation and experimental study of PCR chip based on silicon", *Sens. Actuator B-Chem.*, vol. 108, pp. 695–699, 2005.

[96] C.S. Liao, G.B. Lee, J.J. Wu, C.C. Chang, T.M. Hsieh, F.C. Huang, C.H. Luo, "Micromachined polymerase chain reaction system for multiple DNA amplification of upper respiratory tract infectious diseases", *Biosens Bioelectron*, vol. 20, pp. 1341-1348, 2005.

[97] M.U. Kopp, A.J. de Mello, A. Manz, "Chemical amplification: Continuous-flow PCR on a chip", *Science*, vol. 280, pp. 1046-1048, 1998.

[98] I. Schneegaß, R. Bräutigam, J.M. Köhler, "Miniaturized flow-through PCR with different template types in a silicon chip thermocycler", *Lab on a Chip*, vol. 1, pp. 42-49, 2001.

[99] Q.T. Zhang, W.H. Wang, H.S. Zhang, Y.L. Wang, "Temperature analysis of continuous-flow micro-PCR based on FEA", *Sens. Actuator B-Chem.*, vol. 82, pp. 75-81, 2002.

[100] K. Sun, A. Yamaguchi, Y. Ishida, S. Matsuo, H. Misawa, "A heater-integrated transparent microchannel chip for continuous-flow PCR", *Sens. Actuator B-Chem.*, vol. 84, pp. 283-289, 2002.

[101] W. Wang, Z.-X. Li, R. Luo, S.-H. Lu, A.-D. Xu, Y.-J. Yang, "Droplet-based micro oscillating-flow PCR chip", *J. Micromech. Microeng.*, vol. 15, pp. 1369–1377, 2005.

[102] E.T. Lagally, I. Medintz, R.A. Mathies, "Single-molecule DNA amplification and analysis in an integrated microfluidic device", *Anal. Chem.*, vol. 73, pp. 565-570, 2001.

[103] E.T. Lagally, C.A. Emrich, R.A. Mathies, "Fully integrated PCR-capillary electrophoresis microsystem for DNA analysis", *Lab on a Chip*, vol. 1, pp. 102-107, 2001.

[104] H. Kim, S. Suk, N. Park, J.H. Hahn. "Microchip for continuous on-line PCR product analysis". in *microTAS 2004*. Malmö. 2004.

[105] M.L. Wong, J.F. Medrano, "Real-time PCR for mRNA quantitation", *Biotechniques*, vol. 39, pp. 75-85, 2005.

[106] J. Wilhelm, A. Pingoud, "Real-time polymerase chain reaction", *Chembiochem*, vol. 4, pp. 1120-1128, 2003.

[107] D.A. Simpson, S. Feeney, C. Boyle, A.W. Stitt, "Retinal VEGF mRNA measured by SYBR green I fluorescence: A versatile approach to quantitative PCR", *Mol. Vis.*, vol. 6, pp. 178-183, 2000.

[108] R.H. Lekanne Deprez, A.C. Fijnvandraat, J.M. Ruijter, A.F. Moorman, "Sensitivity and accuracy of quantitative real-time polymerase chain reaction using SYBR green I depends on cDNA synthesis conditions", *Anal. Biochem.*, vol. 307, pp. 63-69, 2002.

[109] P.S. Bernard, C.T. Wittwer, "Homogeneous amplification and variant detection by fluorescent hybridization probes", *Clin. Chem.*, vol. 46, pp. 147-148, 2000.

[110] U.E. Gibson, C.A. Heid, P.M. Williams, "A novel method for real time quantitative RT-PCR", *Genome Res.*, vol. 6, pp. 995-1001, 1996.

[111] I.V. Kutyavin, I.A. Afonina, A. Mills, V.V. Gorn, E.A. Lukhtanov, E.S. Belousov, M.J. Singer, D.K. Walburger, S.G. Lokhov, A.A. Gall, R. Dempcy, M.W. Reed, R.B. Meyer, J. Hedgpeth, "3'-minor groove binder-DNA probes increase sequence specificity at PCR extension temperatures", *Nucleic Acids Res*, vol. 28, pp. 655-661, 2000.

[112] S. Tyagi, F.R. Kramer, "Molecular beacons: probes that fluoresce upon hybridization", *Nat. Biotechnol.*, vol. 14, pp. 303-308, 1996.

[113] S. Tyagi, S.A. Marras, F.R. Kramer, "Wavelength-shifting molecular beacons", *Nat. Biotechnol.*, vol. 18, pp. 1191-1196, 2000.

[114] D. Whitcombe, J. Theaker, S.P. Guy, T. Brown, S. Little, "Detection of PCR products using self-probing amplicons and fluorescence", *Nat. Biotechnol.*, vol. 17, pp. 804-807, 1999.

[115] I.A. Nazarenko, S.K. Bhatnagar, R.J. Hohman, "A closed tube format for amplification and detection of DNA based on energy transfer", *Nucleic Acids Res*, vol. 25, pp. 2516-2521, 1997.

[116] I. Nazarenko, B. Lowe, M. Darfler, P. Ikonomi, D. Schuster, A. Rashtchian, "Multiplex quantitative PCR using self-quenched primers labeled with a single fluorophore", *Nucleic Acids Res*, vol. 30, pp. e37, 2002.

[117] J. Liu, M. Enzelberger, S. Quake, "A nanoliter rotary device for polymerase chain reaction", *Electrophoresis*, vol. 23, pp. 1531-1536, 2002.

[118] A. Gulliksen, L. Solli, F. Karlsen, H. Rogne, E. Hovig, T. Nordstrom, R. Sirevag, "Real-time nucleic acid sequence-based amplification in nanoliter volumes", *Anal. Chem.*, vol. 76, pp. 9-14, 2004.

[119] A. Gulliksen, L.A. Solli, K.S. Drese, O. Sorensen, F. Karlsen, H. Rogne, E. Hovig, R. Sirevag, "Parallel nanoliter detection of cancer markers using polymer microchips", *Lab Chip*, vol. 5, pp. 416-420, 2005.

[120] J. El-Ali, I.R. Perch-Nielsen, C.R. Poulsen, D.D. Bang, P. Telleman, A. Wolff, "Simulation and experimental validation of a SU-8 based PCR thermocycler chip with integrated heaters and temperature sensor", *Sens. Actuator A-Phys.*, vol. 110, pp. 3–10, 2004.

[121] C.R. Poulsen, J. El-Ali, I.R. Perch-Nielsen, D.D. Bang, A. Wolff, "Detection of a putative virulence cadF gene of Campylobacter jejuni isolates from different sources using a microfabricated PCR chip", *J. Rapid Methods Autom. Microbiol.*, vol. 13, pp. 111-126, 2005.

[122] W.-J. Chang, D. Akin, M. Sedlak, M.R. Ladisch, R. Bashir, "Poly (dimethylsiloxane) (PDMS) and silicon hydrid biochip for bacterial culture", *Biomedical Microdevices*, vol. 5, pp. 281-290, 2003.

[123] R. Davidsson, B. Johansson, V. Passoth, M. Bengtsson, T. Laurell, J. Emneus, "Microfluidic biosensing systems. Part II. Monitoring the dynamic production of glucose and ethanol from microchip-immobilised yeast cells using enzymatic chemiluminescent micro-biosensors", *Lab Chip*, vol. 4, pp. 488-494, 2004.

[124] D.M. Spence, N.J. Torrence, M.L. Kovarik, R.S. Martin, "Amperometric determination of nitric oxide derived from pulmonary artery endothelial cells immobilized in a microchip channel", *Analyst*, vol. 129, pp. 995-1000, 2004.

[125] M.G. Alonso-Amigo, "Polymer Microfabrication for Microarrays, Microreactors and Microfluidics", *Journal of the Association for Laboratory Automation*, vol. 5, pp. 96-101, 2000.

[126] H. Becker, C. Gartner, "Polymer microfabrication methods for microfluidic analytical applications", *Electrophoresis*, vol. 21, pp. 12-26, 2000.

[127] G.S. Fiorini, D.T. Chiu, "Disposable microfluidic devices: fabrication, function, and application", *Biotechniques*, vol. 38, pp. 429-446, 2005.

[128] C.J. Kirkpatrick, F. Bittinger, M. Wagner, H. Kohler, T.G. van Kooten, C.L. Klein, M. Otto, "Current trends in biocompatibility testing", *Proc Inst Mech Eng [H]*, vol. 212, pp. 75-84, 1998.

[129] Y.X. Wang, J.L. Robertson, W.B. Spillman, Jr., R.O. Claus, "Effects of the chemical structure and the surface properties of polymeric biomaterials on their biocompatibility", *Pharm Res*, vol. 21, pp. 1362-1373, 2004.

[130] N.D. Gallant, J.R. Capadona, A.B. Frazier, D.M. Collard, A.J. Garcia, "Micropatterned surfaces to engineer focal adhesions for analysis of cell adhesion strengthening", *Langmuir*, vol. 18, pp. 5579-5584, 2002.

[131] A. Sin, K.C. Chin, M.F. Jamil, Y. Kostov, G. Rao, M.L. Shuler, "The design and fabrication of three-chamber microscale cell culture analog devices with integrated dissolved oxygen sensors", *Biotechnol Prog*, vol. 20, pp. 338-345, 2004.

[132] J.L. Charest, L.E. Bryant, A.J. Garcia, W.P. King, "Hot embossing for micropatterned cell substrates", *Biomaterials*, vol. 25, pp. 4767-4775, 2004.

[133] S. Bouaidat, B. Winther-Jensen, S.F. Christensen, J. Jonsmann, "Plasma-polymerized coatings for bio-MEMS applications", *Sens. Actuator A-Phys.*, vol. 110, pp. 390-394, 2004.

[134] E.W.H. Jager, C. Immerstrand, K.H. Petersen, K.-E. Magnusson, I. Lundstorm, O. Inganas, "The cell clinic: closable microvials for single cell studies", *Biomedical Microdevices*, vol. 4, pp. 177-187, 2002.

[135] K.E. Geckeler, R. Wacker, W.K. Aicher, "Biocompatibility correlation of polymeric materials using human osteosarcoma cells", *Naturwissenschaften*, vol. 87, pp. 351-354, 2000.

[136] C.J. Kirkpatrick, A. Dekker, "Quantitative evaluation of cell interaction with biomaterials *in vitro*", *Adv. Biomater.*, pp. 31, 1992.

[137] T.G. van Kooten, C.L. Klein, H. Kohler, C.J. Kirkpatrick, D.F. Williams, R. Eloy, "From cytotoxicity to biocompatibility testing in vitro: cell adhesion molecule expression defines a new set of parameters", *J Mater Sci Mater Med*, vol. 8, pp. 835-841, 1997.

[138] M.J. Dalby, L. Di Silvio, E.J. Harper, W. Bonfield, "In vitro adhesion and biocompatability of osteoblast-like cells to poly(methylmethacrylate) and poly(ethylmethacrylate) bone cements", *J Mater Sci Mater Med*, vol. 13, pp. 311-314, 2002.

[139] C.J. Kirkpatrick, T. Otterbach, D. Anderheiden, J. Schiefer, H. Richter, H. Höcker, C.H. Mittermayer, A. Dekker, "Quantitative scanning electron microscopy (SEM) to study the adhesion and spreading of humen endothelial cells to surface-modified poly(carbonate urethane)s", *Cells and Mater.*, pp. 166-177, 1992.

[140] D.V. Nicolau, T. Taguchi, H. Tanigawa, S. Yoshikawa, "Control of neuronal cell attachment by functionality manipulation of diazo-naphthoquinone/novolak photoresist surface", *Biosens Bioelectron*, vol. 11, pp. 1237-1252, 1996.

[141] D. Irimia, J.O.M. Karlsson, "Development of a cell patterning technique using poly (ethylene glycol) disilane", *Biomedical Microdevices*, vol. 5, pp. 185-194, 2003.

[142] H.M. Shapiro, M. Hercher, "Flov cytometers using optical waveguides in place of lenses for specimen illumination and light collection", *Cytometry*, vol. 7, pp. 221-223, 1986.

[143] D. Qin, Y.N. Xia, J.A. Rogers, R.J. Jackman, X.M. Zhao, G.M. Whitesides, "Microfabrication, microstructures and microsystems", *Topics in Current Chemistry*, vol. 194, pp. 1-20, 1998.

[144] S.C. Jakeway, A.J. de Mello, E.L. Russell, "Review: Miniaturized total analysis systems for biological analysis", *Fresenius J. Anal. Chem.*, vol. 366, pp. 525-539, 2000.

[145] X.-F. Zhou, J.P.H. Burt, M.S. Talary, A.D. Goater, R. Pethig, "Development of biofactory-on-a-chip technology", *Proceedings of the SPIE - Micromachining & Microfabrication*, vol. 4177, pp. 241-250, 2000.

[146] D.J. Beebe, G.A. Mensing, G.M. Walker, "Physics and application of microfluidics in biology", *Annu. Rev. Biomed. Eng.*, vol. 4, pp. 261-286, 2002.

[147] P.A. Auroux, D. Iossifidis, D.R. Reyes, A. Manz, "Micro total analysis systems. 2. Analytical standard operations and applications", *Anal. Chem.*, vol. 74, pp. 2637-2652, 2002.

[148] J. Khandurina, A. Guttman, "Bioanalysis in microfluidic devices", *J. Chromatogr. A*, vol. 943, pp. 159-183, 2002.

[149] E. Verpoorte, "Microfluidic chips for clinical and forensic analysis", *Electrophoresis*, vol. 23, pp. 677-712, 2002.

[150] A. Wolff, U.D. Larsen, P. Friis, P. Telleman. "Chip-Integrated Microfluidic System for Cell Sorting and Cell Culturing". in *Eurosensors XIV (2000)*. Copenhagen, Denmark: MIC - Mikroelektronik Centret. 2000.

[151] U.D. Larsen, A. Wolff, P. Telleman, Method of establishing at least one enveloped flow in a channel, Patent No. WO0169203, Denmark, 2001.

[152] Z. Wang, J. El-Ali, M. Engelund, T. Gotsaed, I.R. Perch-Nielsen, K.B. Mogensen, D. Snakenborg, J.P. Kutter, A. Wolff, "Measurements of scattered light on a microchip flow cytometer with integrated polymer based optical elements", *Lab on a Chip*, vol. 4, pp. 372-377, 2004.

[153] R. Marie, S. Schmid, A. Johansson, L. Ejsing, M. Nordström, D. Häfliger, C. Christensen, A. Boisen, M. Dufva, "Immobilisation of DNA to polymerised SU-8 photoresist", *Biosensors and Bioelectronics*, vol. 21, pp. 1327-1332, 2006.

[154] J.K. Larsen, I.J. Christensen, J. Christiansen, B.T. Mortensen, "Washless double staining of unfixed nuclei for flow cytometric analysis of DNA and a nuclear antigen (Ki-67 or bromodeoxyuridine)", *Cytometry*, vol. 12, pp. 429-437, 1991.

[155] L.L. Vindelov, I.J. Christensen, N.I. Nissen, "A detergent-trypsin method for the preparation of nuclei for flow cytometric DNA analysis", *Cytometry*, vol. 3, pp. 323-327, 1983.

[156] D. Snakenborg, G. Perozziello, H. Klank, O. Geschke, J.P. Kutter, "Direct milling and casting of polymer-based optical waveguides for improved transparancy in the visible range", *J. Micromech. Microeng.*, vol. 16, pp. 375-381, 2006.

[157] Y. Huang, X.B. Wang, J.A. Tame, R. Pethig, "Electrokinetic behavior of colloidal particles in traveling-electric-fields studies using yeast-cells", *J. Phys. D-Appl. Phys.*, vol. 26, pp. 1528-1535, 1993.

[158] M.S. Talary, J.P.H. Burt, J.A. Tame, R. Pethig, "Electromanipulation and separation of cells using travelling electric fields", *J. Phys. D-Appl. Phys.*, vol. 29, pp. 2198-2203, 1996.

[159] R. Holzel, "Electrorotation of single yeast cells at frequencies between 100 Hz and 1.6 GHz", *Biophys. J.*, vol. 73, pp. 1103-1109, 1997.

[160] J. Cheng, E.L. Sheldon, L. Wu, M.J. Heller, J.P. O'Connell, "Isolation of cultured cervical carcinoma cells mixed with peripheral blood cells on a bioelectronic chip", *Anal. Chem.*, vol. 70, pp. 2321-2326, 1998.

[161] Y. Huang, K.L. Ewalt, M. Tirado, T.R. Haigis, A. Forster, D. Ackley, M.J. Heller, J.P. O'Connell, M. Krihak, "Electric manipulation of bioparticles and macromolecules on microfabricated electrodes", *Anal. Chem.*, vol. 73, pp. 1549-1559, 2001.

[162] N.J. Abernethy, W. Chin, H. Lyons, J.B. Hay, "A dual laser analysis of the migration of xritc-labeled, fitc- labeled, and double-labeled lymphocytes in sheep", *Cytometry*, vol. 6, pp. 407-413, 1985.

[163] F.M. White, "Viscous fluid flow", 2nd ed. ed. 1991, New York: McGraw-Hill.

[164] H. Morgan, A.G. Izquierdo, D. Bakewell, N.G. Green, A. Ramos, "The dielectrophoretic and travelling wave forces generated by interdigitated electrode arrays: analytical solution using Fourier series", *J. Phys. D-Appl. Phys.*, vol. 34, pp. 1553-1561, 2001.

[165] M.A. Hubbe, "Theroy of detechment of colloidal particles from flat surfaces exposed to flow", *Colloids and Surfaces*, vol. 12, pp. 151-178, 1984.

[166] S. Bouaidat, C. Berendsen, P. Thomsen, S.G. Petersen, A. Wolff, J. Jonsmann, "Micro patterning of cell and protein non-adhesive plasma polymerized coatings for biochip applications", *Lab on a Chip*, vol. 4, pp. 632-637, 2004.

[167] S.W. Lee, Y.C. Tai, "A micro cell lysis device", *Sens. Actuator A-Phys.*, vol. 73, pp. 74-79, 1999.

[168] G. Fuhr, S.G. Shirley, "Cell handling and characterization using micron and submicron electrode arrays - state-of-the-art and perspectives of semiconductor microtools", *J. Micromech. Microeng.*, vol. 5, pp. 77-85, 1995.

[169] J. El-Ali, *Ph.D. Thesis: Design and fabrication of PCR chip with integrated Dielectrophoretic based sample pretreatment system*, in *MIC - Dept. of Micro- and Nanotechnology*. 2003, Technical University of Denmark: Kgs. Lyngby, Denmark.

[170] D.D. Bang, E.M. Nielsen, F. Scheutz, K. Pedersen, K. Handberg, M. Madsen, "PCR detection of seven virulence and toxin genes of Campylobacter jejuni and Campylobacter coli isolates from Danish pigs and cattle and cytolethal distending toxin production of the isolates", *J. Appl. Microbiol.*, vol. 94, pp. 1003-1014, 2003.

[171] E.L. Best, E.J. Powell, C. Swift, K.A. Grant, J.A. Frost, "Applicability of a rapid duplex real-time PCR assay for speciation of *Campylobacter jejuni* and *Campylobacter coli* directly from culture plates", *FEMS Microbiol. Lett.*, vol. 229, pp. 237-241, 2003.

[172] C. Yang, Y. Jiang, K. Huang, C. Zhu, Y. Yin, "Application of real-time PCR for quantitative detection of *Campylobacter jejuni* in poultry, milk and environmental water", *FEMS Immunol. Med. Microbiol.*, vol. 38, pp. 265-271, 2003.

[173] M. Abu-Halaweh, J. Bates, B.K. Patel, "Rapid detection and differentiation of pathogenic *Campylobacter jejuni* and *Campylobacter coli* by real-time PCR", *Res. Microbiol.*, vol. 156, pp. 107-114, 2005.

[174] M.T. Madigan, J.M. Martinku, J. Parker, "Brock biology of microorganisms", Eighth ed. 1997, New Jersey: Prentice-Hall, Inc.

[175] P.T. Monis, S. Giglio, C.P. Saint, "Comparison of SYTO9 and SYBR green I for Real-time polymerase chain reaction and investigation of the effect of dye concentration on amplification and DNA melting curve analysis", *Anal. Biochem.*, vol. 340, pp. 24-34, 2005.

[176] M.A. Shoffner, J. Cheng, G.E. Hvichia, L.J. Kricka, P. Wilding, "Chip PCR .1. Surface passivation of microfabricated silicon- glass chips for PCR", *Nucleic Acids Res.*, vol. 24, pp. 375-379, 1996.

[177] Y.S. Shin, K. Cho, S.H. Lim, S. Chung, S.-J. Park, C. Chung, D.-C. Han, J.K. Chang, "PDMS-based micro PCR chip with parylene coating", *J. Micromech. Microeng.*, vol. 13, pp. 768–774, 2003.

[178] J. Felbel, I. Bieber, J. Pipper, J.M. Kohler, "Investigations on the compatibility of chemically oxidized silicon (SiOx)-surfaces for applications towards chip-based polymerase chain reaction", *Chem. Eng. J.*, vol. 101, pp. 333–338, 2004.

[179] B.C. Giordano, E.R. Copeland, J.P. Landers, "Towards dynamic coating of glass microchip chambers for amplifying DNA via the polymerase chain reaction", *Electrophoresis*, vol. 22, pp. 334-340, 2001.

[180] J. Charnley, "Anchorage of the femoral head prosthesis to the shaft of the femur", *J Bone Joint Surg Br*, vol. 42-B, pp. 28-30, 1960.

[181] S. Petronis, M. Stangegaard, C.B. Christensen, M. Dufva, "Transparent polymeric cell culture chip with integrated temperature control and uniform media perfusion", *Biotechniques*, vol. 40, pp. 368-376, 2006.

[182] M. Stangegaard, S. Petronis, A.M. Jorgensen, C. Christensen, M. Dufva, "A biocompatible micro cell culture chamber (µCCC) for the culturing and on-line monitoring of eukaryote cells", *Lab Chip*, 2006.

[183] C.S. Chen, X. Jiang, G.M. Whitesides, "Microengineering the environment of mammalian cells in culture", *MRS Bulletin*, pp. 194-201, 2005.

[184] D. Williams, "Revisiting the definition of biocompatibility", *Med Device Technol*, vol. 14, pp. 10-13, 2003.

[185] A. Dekker, C. Panfil, M. Valdor, G. Pennartz, H. Richter, C.H. Mittermayer, C.J. Kirkpatrick, "Quantitative methods for in vitro cytotoxicity testing of biomaterials", *Cells Mater.*, pp. 101-112, 1994.

[186] T. Mappes, S. Achenbach, A. Last, J. Mohr, T. R., "Evaluation of optical qualities of a LIGA-spectrometer in SU-8", *Microsystem Technologies*, vol. 10, pp. 560–563, 2004.

[187] J. Zhang, K.L. Tan, H.Q. Gong, "Characterization of the polymerization of SU-8 photoresist and its applications in micro-electro-mechanical systems (MEMS)", *Polymer Testing*, vol. 20, pp. 693-701, 2001.

[188] G. Kotzar, M. Freas, P. Abel, A. Fleischman, S. Roy, C. Zorman, J.M. Moran, J. Melzak, "Evaluation of MEMS materials of construction for implantable medical devices", *Biomaterials*, vol. 23, pp. 2737-2750, 2002.

[189] N. Iranpoor, P. Salehi, "Ceric ammonium nitrate: a mild and efficient reagent for conversion of epoxides to beta-nitrato alcohols", *Tetrahedron*, vol. 51, pp. 909-912, 1995.

[190] M. Nordstrom, R. Marie, M. Calleja, A. Boisen, "Rendering SU-8 hydrophilic to facilitate use in micro channel fabrication", *J. Micromech. Microeng.*, vol. 14, pp. 1614–1617, 2004.

[191] R.J. Cho, M.J. Campbell, E.A. Winzeler, L. Steinmetz, A. Conway, L. Wodicka, T.G. Wolfsberg, A.E. Gabrielian, D. Landsman, D.J. Lockhart, R.W. Davis, "A genome-wide transcriptional analysis of the mitotic cell cycle", *Mol Cell*, vol. 2, pp. 65-73, 1998.

[192] P.T. Spellman, G. Sherlock, M.Q. Zhang, V.R. Iyer, K. Anders, M.B. Eisen, P.O. Brown, D. Botstein, B. Futcher, "Comprehensive identification of cell cycle-regulated genes of the yeast Saccharomyces cerevisiae by microarray hybridization", *Mol Biol Cell*, vol. 9, pp. 3273-3297, 1998.

[193] V.R. Iyer, M.B. Eisen, D.T. Ross, G. Schuler, T. Moore, J.C. Lee, J.M. Trent, L.M. Staudt, J. Hudson, Jr., M.S. Boguski, D. Lashkari, D. Shalon, D. Botstein, P.O. Brown, "The transcriptional program in the response of human fibroblasts to serum", *Science*, vol. 283, pp. 83-87, 1999.

[194] V.G. Tusher, R. Tibshirani, G. Chu, "Significance analysis of microarrays applied to the ionizing radiation response", *Proc Natl Acad Sci U S A*, vol. 98, pp. 5116-5121, 2001.

[195] S.A. Ahrendt, S. Halachmi, J.T. Chow, L. Wu, N. Halachmi, S.C. Yang, S. Wehage, J. Jen, D. Sidransky, "Rapid p53 sequence analysis in primary lung cancer using an oligonucleotide probe array", *Proc Natl Acad Sci U S A*, vol. 96, pp. 7382-7387, 1999.

[196] T.R. Golub, D.K. Slonim, P. Tamayo, C. Huard, M. Gaasenbeek, J.P. Mesirov, H. Coller, M.L. Loh, J.R. Downing, M.A. Caligiuri, C.D. Bloomfield, E.S. Lander, "Molecular classification of cancer: class discovery and class prediction by gene expression monitoring", *Science*, vol. 286, pp. 531-537, 1999.

[197] A.A. Alizadeh, M.B. Eisen, R.E. Davis, C. Ma, I.S. Lossos, A. Rosenwald, J.C. Boldrick, H. Sabet, T. Tran, X. Yu, J.I. Powell, L. Yang, G.E. Marti, T. Moore, J. Hudson, Jr., L. Lu, D.B. Lewis, R. Tibshirani, G. Sherlock, W.C. Chan, T.C. Greiner, D.D. Weisenburger, J.O. Armitage, R. Warnke, R. Levy, W. Wilson, M.R. Grever, J.C. Byrd, D. Botstein, P.O. Brown, L.M. Staudt, "Distinct types of diffuse large B-cell lymphoma identified by gene expression profiling", *Nature*, vol. 403, pp. 503-511, 2000.

[198] S.M. Dhanasekaran, T.R. Barrette, D. Ghosh, R. Shah, S. Varambally, K. Kurachi, K.J. Pienta, M.A. Rubin, A.M. Chinnaiyan, "Delineation of

prognostic biomarkers in prostate cancer", *Nature*, vol. 412, pp. 822-826, 2001.

[199] L.T. Allen, E.J. Fox, I. Blute, Z.D. Kelly, Y. Rochev, A.K. Keenan, K.A. Dawson, W.M. Gallagher, "Interaction of soft condensed materials with living cells: phenotype/transcriptome correlations for the hydrophobic effect", *Proc Natl Acad Sci U S A*, vol. 100, pp. 6331-6336, 2003.

[200] F. Carinci, F. Pezzetti, S. Volinia, F. Francioso, D. Arcelli, E. Farina, A. Piattelli, "Zirconium oxide: analysis of MG63 osteoblast-like cell response by means of a microarray technology", *Biomaterials*, vol. 25, pp. 215-228, 2004.

[201] F. Fixe, M. Dufva, P. Telleman, C.B. Christensen, "One-step immobilization of aminated and thiolated DNA onto poly(methylmethacrylate) (PMMA) substrates", *Lab on a Chip*, vol. 4, pp. 191-195, 2004.

[202] L.A. Roberts, H. Glenn, C.S. Hahn, B.S. Jacobson, "Cdc42 and RhoA are differentially regulated during arachidonate-mediated HeLa cell adhesion", *J Cell Physiol*, vol. 196, pp. 196-205, 2003.

[203] J.B. Weitzman, L. Fiette, K. Matsuo, M. Yaniv, "JunD protects cells from p53-dependent senescence and apoptosis", *Mol Cell*, vol. 6, pp. 1109-1119, 2000.

[204] X.M. Zheng, D. Black, P. Chambon, J.M. Egly, "Sequencing and expression of complementary DNA for the general transcription factor BTF3", *Nature*, vol. 344, pp. 556-9, 1990.

[205] M. Dufva, C.B. Christensen, "Diagnostic and analytical applications of protein microarrays", *Expert Rev Proteomics*, vol. 2, pp. 41-48, 2005.

[206] I.V. Yang, E. Chen, J.P. Hasseman, W. Liang, B.C. Frank, S. Wang, V. Sharov, A.I. Saeed, J. White, J. Li, N.H. Lee, T.J. Yeatman, J. Quackenbush, "Within the fold: assessing differential expression measures and reproducibility in microarray assays", *Genome Biol.*, pp. R62, 2002.

[207] C. Workman, L.J. Jensen, H. Jarmer, R. Berka, L. Gautier, H.B. Nielser, H.H. Saxild, C. Nielsen, S. Brunak, S. Knudsen, "A new non-linear normalization method for reducing variability in DNA microarray experiments", *Genome Biol.*, pp. R48, 2002.

[208] R.A. Irizarry, L. Gautier, B.M. Bolstad, C. Miller, M. Astrand, L.M. Cope, R. Gentleman, J. Gentry, C. Halling, W. Huber, J. MacDonald, B.I.P. Rubinstein, C. Workman, J. Zhang, *affy: Methods for Affymetrix Oligonucleotide Arrays. R package*. 2005.

[209] R.C. Gentleman, V.J. Carey, D.M. Bates, B. Bolstad, M. Dettling, S. Dudoit, B. Ellis, L. Gautier, Y. Ge, J. Gentry, K. Hornik, T. Hothorn, W. Huber, S. Iacus, R. Irizarry, F. Leisch, C. Li, M. Maechler, A.J. Rossini, G. Sawitzki, C. Smith, G. Smyth, L. Tierney, J.Y. Yang, J. Zhang, "Bioconductor: open software development for computational biology and bioinformatics", *Genome Biol.*, pp. R80, 2004.

[210] R_Development_Core_Team, *R: A language and environment for statistical computing*. 2005, R Foundation for Statistical Computing: Vienna, Austria.

[211] C.-J. Lin, M.-T. Lin, S.-P. Wu, F.-G. Tseng, "High density and through wafer copper interconnections and solder bumps for MEMS wafer-level packaging", *Microsystem Technologies*, vol. 10, pp. 517-521, 2004.

[212] H.-A. Yang, M. Wu, W. Fang, "Localized induction heating solder bonding for wafer level MEMS packaging", *J. Micromech. Microeng.*, vol. 15, pp. 394-399, 2005.

Appendix A

Process sequence for Polymer waveguides on glass wafer

Wafers: 4" 500µm thick Borofloat glass wafers from Schott.

1. **Cleaning of wafers:** Clean on turning table using Triton X100 soap. Rinse 10 minutes in piranha (4:1 H_2SO_4: H_2O_2).
2. **Spinning of SU-8 waveguide core and fluidic system layer:** Dehydrate wafers in 250 ºC oven for at least 3 Hours. Spin on 90µm SU-8 (XP2075, Microchem). KS-spinner: 1800 rpm, 30 seconds.
3. **Soft baking of SU-8 layer:** Softbake the SU-8 on 65 ºC hotplate for 5 minutes with a 5 minutes ramp, 95 ºC hotplate for 20 minutes with a 5 minutes ramp, 65 ºC hotplate for 1 minute with a 5 minutes ramp. Let wafers cool down on hotplate.
4. **Photolithography:** UV exposure through waveguide mask. KS aligner settings: Multiple exposure, 10 cycles of 10 seconds exposure 10 seconds wait, constant power of 275 W, soft contact mode.
5. **Post exposure baking:** Bake wafers on 65 ºC hotplate for 1 minute with a 5 minutes ramp, 95 ºC hotplate for 10 minutes with a 5 minutes ramp, 65 ºC hotplate for 1 minute with a 10 minutes ramp. Let wafers cool down on hotplate.
6. **Development of SU-8:** Develop wafers in PGMEA: 8 minutes in developer labeled SU-8 first, 2 minutes in developer labeled SU-8 final. Rinse in isopropanol solution.

Appendix B

Process sequence for DEP - FC chip fabrication

Wafers: 4" 500μm thick Pyrex glass wafers from Schott.

1. **Cleaning of wafers:** Clean on turning table using triton X-100 soap, rinse 10 minutes in piranha (4:1 H2SO4: H2O2).
2. **Dehydration of wafers:** dehydrate wafers in 120 °C oven for approx one hour.
3. **HDMS:** HDMS treatment for 1 hour.
4. **Spincoating with photoresist for lift-off:** Tack 1, 1.5 μm AZ5314 resist, soft bake (recipe: pr1_5 or _2min. on 90°C hotplate).
5. **Photolithography:** UV exposure through “electrode” mask, 5 seconds exposure time, 275 W const. Power, hard contact mode.
6. **Image reversal:** reverse bake on 120 °C hotplate for 2 minutes, UV flood exposure wafers for 50 seconds.
7. **Development of resist:** develop wafers in a 1 AZ351B: 5 DI water solution for about 1 minutes.
8. **Plasma asher:** 100 W, 20 seconds, recipe 11.
9. **Metal deposition:** deposition of 10 nm Ti followed by 200 nm Au.
10. **Lift-off:** Lift-off bath (acetone) with ultrasonic agitation 10-15 min.
11. **Plasma asher:** 100 W, 1 min, recipe 11.
12. **Dehydrate bake:** leave in 250 °C oven overnight, and prepare SU-8 XP2075 syringe.
13. **Spin-coating 90μm SU-8 XP2075 Microchem:** take wafer directly from oven, for 90 μm thick, the recipe is 1800 rpm, 30 seconds.
14. **Soft baking SU-8:** ramping: 2 minutes, 65 °C in 1 minutes; ramping 5 minutes, 95 °C in 25 minutes. cool down on hotplate.
15. **Photolithography:** UV exposure through “SU-8” mask. KS aligner settings: multiple exposure, 10 cycles of 10 seconds, exposure followed by 10 seconds waiting, 275 W const power, soft contact mode.
16. **Post exposure baking:** ramping 10 minutes, 90 °C for 25 minutes. Cool down on hotplate approx 45 minutes.
17. **Development of SU-8:** develop wafers in PGMEA, 8 minutes in developer labeled SU-8 first, 2 minutes in developer labeled Su-8 final. Rinse in isopropanol.

Appendix C

Process sequence for real - time PCR chip

Wafers: 4" 500µm thick Borofloat glass wafers from Schott.

1. **Cleaning of wafers:** Clean on turning table using Triton X100 soap. Rinse 10 minutes in piranha (4:1 H_2SO_4: H_2O_2).
2. **Spinning of resist for metal mask:** Dehydrate wafers in 120 °C oven for ~1 Hour. HDMS treatment for 45 minutes. Spin on 1.5 µm AZ5214 photoresist, soft-bake for 2 minutes on 90 °C hotplate, recipe pr1_5.
3. **Photolithography:** UV exposure through metallization mask (mask: metal). KS aligner settings: 5 seconds exposure time, constant power of 275 W, soft contact mode.
4. **Image reversal:** Bake resist on 120 °C hotplate for 2 minutes. UV flood exposure wafers for ~30 seconds.
5. **Development of resist:** Develop wafers in a 1 AZ 351B: 5 DI water solution for ~60 seconds at 22 °C.
6. **Plasma asher:** 100 W, 20 seconds, recipe 11.
7. **Deposition of platinum:** Deposit 200 nm platinum using e-beam evaporation with a 100 Å titanium adhesion layer. (Alcatel).
8. **Lift-off:** The platinum is lifted in an ultrasonic acetone bath for 5 minutes.
9. **Plasma asher:** 100 W, 20 seconds, recipe 11. (Prepare SU-8 XP2075 syringe).
10. **Spinning of SU-8 electrode protection layer:** Dehydrate wafers in 250 °C oven for at least 3 Hours. Spin on 5 µm SU-8 (XP2005, Microchem). KS-spinner: 3000 rpm, 30 seconds.
11. **Soft baking of SU-8 protection layer**: Soft-bake the SU-8 on the hotplate at 65 °C for 1 minute with a 3 minute ramp, then 90 °C for 3 minutes with a 1 minute ramp. Let wafers cool down on hotplate.
12. **Photolithography:** UV exposure through protection mask (mask: protection). KS aligner settings: 50 seconds exposure time, constant power of 275 W, proximity mode 25 µm.
13. **Post exposure baking:** Bake wafers on 95 °C hotplate for 8 minutes with a 5 minutes ramp. Ramp temperature to 105 °C using a 2 minutes ramp. Bake at 105 °C for 10 minutes. Let wafers cool down on hotplate.
14. **Spinning of SU-8 layer 1 for PCR chamber and waveguide:** Spin on 200 µm SU-8 (XP2075, Microchem). KS-spinner: 1000 rpm, 30 seconds.
15. **Soft baking of SU-8 layer 1 for PCR chamber and waveguide:** Soft-bake the SU-8 on 95 °C hotplate for 45 minutes with a 10 minutes ramp. Let wafers cool down on hotplate.
16. **Spinning of SU-8 layer 2 for PCR chamber and waveguide:** Spin on 200 µm SU-8 (XP2075, Microchem). KS-spinner: 1000 rpm, 30 seconds.

17. **Soft baking of SU-8 layer 2 for PCR chamber and waveguide:** Soft-bake the SU-8 on 95 °C hotplate for 2 hours with a 10 minutes ramp. Let wafers cool down on hotplate.
18. **Photolithography:** UV exposure through PCR chamber mask (mask: chamber). KS aligner settings: Multiple exposure, 10 cycles of 15 seconds exposure 10 seconds wait, constant power of 275 W, soft contact mode.
19. **Post exposure baking:** Bake wafers on 100 °C hotplate for 45 minutes with a 10 minutes ramp. Let wafers cool down on hotplate.
20. **Development of SU-8:** Develop wafers in PGMEA: 25 minutes in developer labeled SU-8 first, 5 minutes in developer labeled SU-8 final. Rinse in isopropanol solution.

Appendix D

Process sequence for hydrophilic cell patterning on SU-8

Wafers: 4" 500µm thick Borofloat glass wafers from Schott.

1. **Cleaning of wafers:** Clean on turning table using Triton X100 soap. Rinse 10 minutes in piranha (4:1 H2SO4: H2O2).
2. **Spinning of 5 µm thin SU-8 layer:** Dehydrate wafers in 250 °C oven for at least 3 Hours. Spin on 5 µm SU-8 (XP2005, Microchem). KS-spinner: 3000 rpm, 30 seconds.
3. **Soft baking of thin SU-8 layer**: Soft-bake the SU-8 on the hotplate at 65 °C for 1 minute with a 3 minute ramp, then 90 °C for 3 minutes with a 1 minute ramp. Let wafers cool down on hotplate.
4. **Photolithography:** UV flood exposure. KS aligner settings: 50 seconds exposure time, constant power of 275 W.
5. **Post exposure baking:** Bake wafers on 95 °C hotplate for 8 minutes with a 5 minutes ramp. Ramp temperature to 105 °C using a 2 minutes ramp. Bake at 105 °C for 10 minutes. Let wafers cool down on hotplate.
6. **Spinning of resist for shadow mask:** Spin on 1.5µm AZ5214 photoresist, soft-bake for 2 minutes on 90 °C hotplate, recipe pr1_5.
7. **Photolithography:** UV exposure through patterning mask (mask: patterning). KS aligner settings: 5 seconds exposure time, constant power of 275 W, soft contact mode.
8. **Image reversal:** Bake resist on 120 °C hotplate for 2 minutes. UV flood exposure wafers for ~30 seconds.
9. **Development of resist:** Develop wafers in a 1 AZ 351B: 5 DI water solution for ~60 seconds at 22 °C.
10. **Plasma asher:** 100 W, 20 seconds, recipe 11.
11. **First step SU-8 surface treatment:** Immerge the whole wafer in the HNO_3-CAN (1 M HNO_3 with 0.1 M $(NH_4)_2Ce(NO_3)_6$) solution, then heated on the 50 °C hotplate for 1 hour. Rinse with MilliQ water, dried with nitrogen stream.
12. **Shadow mask Lift-off:** The shadow mask is lifted in an ultrasonic acetone bath for 5 minutes.
13. **Second step SU-8 surface treatment:** Immerge the wafer in the ethanolamine solution (0.1 M ethanolamine in 0.1 M, pH 9.0 sodium phosphate buffer), then heated on the 50 °C hotplate for 20 minutes. Rinse with MilliQ water, dried with nitrogen stream.

Appendix E

Protocol for FITC labeling of yeast cells

FITC solution:	1 mg/mL fluorescein 5-isothiocyanate (FITC) carbonate buffer (0.05 M, pH 9.6) is prepared and stocked in 4 °C dark place.
Growth of Yeast Cell:	The yeast cells were growth overnight in the Yeast extract Peptone Dextro (YPD) medium (yeast extract 10 g, bacto peptone 20 g, glucose 20 g, and water 1000 mL) at room temperature.
Labeling dosage:	The yeast cells are suspended in MilliQ water at concentration of 10^8 cells/ml. 0.9 mL FITC solution was mixed with 0.1 ml the cell suspension.
Labeling process:	The labeled yeast cells were incubated for 30 - 60 minutes at room temperature or 37 °C. After the labeling, the FITC molecules will conjugate with the cell membrane proteins.
Killing yeast cell:	For killing the yeast cells, 30 mL yeast cells suspension is heated by a 1500 W microwave oven for 30 seconds.

Appendix F

Protocol of Propidium Iodide (PI) labeling Red Blood Cells (RBC)

PI stock solution: 1 mg/mL PI in water (stocked at 4 °C in a dark place).

Staining solution: 0.2 mL PI stock solution and 0.05 mL Triton X-100 (0.5 % v/v) are added into a 10 mL PBS (EDTA 0.5 mM) buffer.

Stock RBC: Rainbow Trout Red Blood Cells (RTRBC) and Chicken Red Blood Cells (CRBC) are suspended in citrate buffer (10^7 cells/mL), and stocked at – 80 °C.

Labeling process: RBCs are quickly thawed in an ice bath. 50 μL stock RBC suspension, 200 μL PI staining solution, and 750 μL PBS are mixed together. Then the whole mixture is put in the ice bath, genteelly shaking on a shaker table for half hour. After labeling PI will be stained the nuclei of the RBCs.

Appendix G

List of publications

Conference abstracts:

1. **Zhenyu Wang**, Jamil El-Ali, Ivan R. Perch-Nielsen, Klaus B. Mogensen, Detlef Snakenborg, Jörg P. Kutter and Anders Wolff. Microchip flow cytometer with integrated polymer optical elements for measurement of scattered light. MEMS2004, Maastricht, Netherlands.
2. **Zhenyu Wang**, Jörg P. Kutter, Anders Wolff. Microchip flow cytometer with integrated polymer optics for fluorescence analysis of cells. μTAS2004, Malmö, Sweden.
3. **Zhenyu Wang**, Peter K. Petersen, Anders Rogeberg, Jörg P. Kutter, Dang D. Bang, Anders Wolff. Real-time monitoring of a dielectrophoresis based selective filter using microchip flow cytometry with integrated polymer waveguides. MEMS2005, Miami, USA.
4. **Zhenyu Wang**, Michael Stangegaard, Martin Dufva, Jörg P. Kutter, and Anders Wolff. A simple hydrophilic treatment of SU-8 surfaces for cell culture and cell patterning. μTAS2005, Boston, USA.
5. **Zhenyu Wang,** Andrea Sekulovic, Jörg P. Kutter, Dang D. Bang, Anders Wolff. Real-time PCR using a PCR microchip with integrated thermal system and polymer waveguides for the detection of *Campylobacter jejuni.* MEMS2006, Istanbul, Turkey.

Journal papers:

1. **Zhenyu Wang**, Jamil El-Ali, Ivan R. Perch-Nielsen, Klaus B. Mogensen, Detlef Snakenborg, Jörg P Kutter and Anders Wolff. Measurements of scattered light on a microchip flow cytometer with integrated polymer based optical elements. Lab on a Chip, 2004, 4, 372-377.
2. Michael Stangegaard, **Zhenyu Wang**[*], Jörg P. Kutter, Martin Dufva and Anders Wolff. Whole genome expression profiling using DNA microarray for determining biocompatibility of polymeric surfaces. Accept by Molecular Biosystems.
3. **Zhenyu Wang**, Ole Hansen, Peter K. Petersen, Anders Rogeberg, Jörg P. Kutter, Dang D. Bang and Anders Wolf. Real-time monitoring of cell sorting using a dielectrophoresis - flowcytometry microchip with integrated polymer waveguides. Submitted to Electrophoresis.
4. **Zhenyu Wang**, Andrea Sekulovic, Jörg P. Kutter, Dang. D. Bang and Anders Wolff. Real-time PCR detection *Campylobacter jejuni* on a microchip with integrated thermal system and polymer waveguides. Submitted to Electrophoresis.

---

[*] Co-first author